Establishment of quality assurance and quality control measures for Boron Neutron Capture Therapy using microdosimetry

Naonori Ko

Kyoto University

Faculty of Engineering

School of Nuclear Engineering

Establishment of quality assurance and quality control measures for Boron Neutron Capture Therapy using microdosimetry

By

Naonori KO

Doctor of Philosophy

A thesis submitted to the School of Nuclear Engineering, Kyoto University, in partial fulfilment of the requirements for the degree of Doctor of Philosophy.

Thesis outline

This thesis presents the research on the application of microdosimetry for radiation protection and quality assurance in Boron Neutron Capture Therapy (BNCT). In a typical BNCT field, there exists a mixture of low and high Linear Energy Transfer (LET) radiation components. Since different LET components have a different biological end-point, it is important to determine the beam quality of the BNCT field to accurately understand the biological effect, which will ultimately benefit patient's receiving BNCT. The thesis outline is as follows:

Chapter 1 – Presents an introduction to BNCT, microdosimetry concepts and current challenges in BNCT Quality Assurance/Quality Control (QA/QC) program.

Chapter 2 – Presents a literature review of experimental microdosimetry and the two detectors used in this thesis; tissue equivalent proportional counter and silicon semiconductor detectors.

Chapter 3 – Presents the investigation on the use of tissue equivalent proportional counters for measurement of beam quality and microdosimetric quantities of a BNCT field.

Chapter 4 – Describes the development of a 3D "bridge" silicon-on-insulator microdosimeter and its application for BNCT dosimetry. The detector characteristic under a neutron field was investigated, along with the effect of a removable thin boron converter.

Chapter 5 – Introduces a new design microdosimeter, called mushroom microdosimeter. The detector characterisation results and its application in BNCT dosimetry was investigated.

Chapter 6– Presents the summary, conclusion and future plans.

Acknowledgment

It is a pleasure to thank all those people who made my research possible due to their tireless help and support all throughout my research. It was such an honour to work in a field with very supportive and respective research team and would like to be grateful to the following individuals who made a great contribution towards my thesis.

Firstly, I would like to express my sincere appreciation to my supervisor, Associate Professor Yoshinori Sakurai for his guidance, encouragement and continuous support throughout my Ph.D. study. Associate Professor Sakurai introduced me to the exciting field of BNCT. Regardless of his busy schedule he was always willing to provide his knowledge and assistance.

I would also like to thank Associate Professor Hiroki Tanaka for his time and effort in supervising and assisting me with experimental measurements. He always made time to discuss with me the progress of the research and kindly answered any questions I had. His endless support throughout my studies and making my Ph.D. journey an enjoyable experience will never be forgotten.

I wish to thank Assistant Professor Takushi Takata for his kind assistance throughout my research. He taught me the basics of dosimetry methods used in BNCT and helped me with Monte Carlo simulations. He offered me his precious time and I am extremely grateful for his generosity.

I would like to thank Distinguished Professor Anatoly Rosenfeld, at the University of Wollongong, for his generosity in agreeing to establish a collaboration with Kyoto University for my Ph.D. research. He has been kind and supportive the entire time and I hope the research and collaboration will continue.

I would like to express my appreciation to Dr. Thuy Linh Tran, at the University of Wollongong, for her enormous help with the microdosimeters. She always devoted time to respond to any questions I had and always provided the information I required. It was an absolute pleasure to work with her.

My appreciation is also extended to the following people for their help and support

during my Ph.D. study:

- Mr. Ryohei Uchida for teaching me the computer network and cluster system used for running simulations. Also, for teaching me how to use the PHITS Monte Carlo program.

- Dr. Dale Prokopovich of ANSTO for supervising and assisting me with the experiments during my visit to ANSTO.

- Dr. Zeljko Pastuovic of ANSTO for operating the ion beam accelerator during my experiments and offering me an overview of the accelerator system installed in ANSTO.

- My fellow postgraduate students at KURNS for assisting me during my difficult transition from Australia to Japan. Mentally it was difficult when I first moved to Japan, but thanks to the friendly people around me, the transition was easy.

- Ushino Lighting Inc. for financially supporting me throughout my Ph.D. study. Thanks to their generous financial aid, I was able to focus all my attention to my research.

To the Sakurai research laboratory postgraduate students: Thank you Keita Okazaki for assisting me with my Japanese language and showing me around the student room at KURNS, and to Michitaka Sato for generally making the student room a pleasant and fun place to be.

Last but not least, I would like to thank my family for supporting me throughout my Ph.D. study. Although they were living overseas, they were always there for me when I needed anything.

Preamble

All of the experiments, work and simulations presented within this thesis were performed by myself, Naonori Ko, with assistance from the following:

The analysis of the Ion Beam Induced Charge Collection study for the 3D bridge SOI and mushroom microdosimeter, presented in chapter 4, was carried out by Dr. Thuy Linh Tran from University of Wollongong. I carried out the experimental work, however, due to my limited stay at ANSTO, I was not able to perform the data analysis. A special in-house software was necessary for analysis, which I did not have access from Japan.

Publication

1. Naonori HU, Hiroki TANAKA, Takushi TAKATA, Keita OKAZAKI, Ryohei UCHIDA, Yoshinori SAKURAI, "Microdosimetric quantities of an accelerator-based neutron source used for boron neutron capture therapy measured using a gas filled proportional counter" Journal of Radiation Research (2019) [In press].

2. Naonori HU, Ryohei UCHIDA, Keita OKAZAKI, Takushi TAKATA, Hiroki TANAKA, Yoshinori SAKURAI, "Neutron beam quality measurement of accelerator based neutron source using microdosimetric technique" Proceedings of the 18th International Congress on Neutron Capture Therapy (2018).

3. Naonori HU, Linh Thuy TRAN, Anatoly ROSENFELD, Yoshinori SAKURAI, "Investigation of the effect of boron distribution inside a silicon microdosimeter" Proceedings of the World Congress on Medical Physics & Biomedical Engineering (2018).

4. Naonori HU, Ryohei UCHIDA, Linh Thuy TRAN, Anatoly ROSENFELD, Yoshinori SAKURAI, "Feasibility study on the use of 3D silicon microdosimeter detectors for microdosimetric analysis in boron neutron capture therapy", Applied Radiation and Isotopes. 2018; 140:109-114.

5. Naonori HU, Takushi TAKATA, Satoru ENDO, Hiroki TANAKA, Yoshinori SAKURAI "Neutron beam quality measurement of the Kyoto University Research reactor using microdosimetric technique" Proceedings of the 115th Scientific Meeting of JSMP (2018).

6. Naonori HU, Ryohei UCHIDA, Linh Thuy TRAN, Anatoly Rosenfeld, Yoshinori SAKURAI, "3D Silicon Microdosimetry for Boron Neutron Capture Therapy: A Simulation Study" Proceedings of the 17th Asia-Oceania Congress of Medical Physics (2017).

7. Naonori HU, Ryohei UCHIDA, Linh Thuy TRAN, Anatoly Rosenfeld, Yoshinori SAKURAI, "3D Silicon Microdosimetry for Boron Neutron Capture Therapy: A Simulation Study" Proceedings of the 8th Japan-Korea Joint Meeting on Medical Physics (2017).

Presentation

1. Naonori HU, Ryohei UCHIDA, Keita OKAZAKI, Takushi TAKATA, Hiroki TANAKA, Yoshinori SAKURAI, "Neutron beam quality measurement of accelerator based neutron source using microdosimetric technique" 18th International Congress on Neutron Capture Therapy, 2018.10.28 (Taipei, Taiwan).

2. Naonori HU, Linh Thuy TRAN, Anatoly ROSENFELD, Yoshinori SAKURAI, "Investigation of the effect of boron distribution inside a silicon microdosimeter" World Congress on Medical Physics & Biomedical Engineering, 2018.06.03 (Prague, Czech Republic).

3. Naonori HU, Takata TAKUSHI, Endo SATORU, Yoshinori SAKURAI, Hiroki TANAKA, "Beam quality determination of Kyoto University Research Reactor using microdosimetry" Institute for Integrated Radiation and Nuclear Science BNCT scientific meeting 2018.05.24 (Osaka, Japan).

4. Naonori HU, Takata TAKUSHI, Endo SATORU, Yoshinori SAKURAI, Hiroki TANAKA, "Neutron beam quality measurement of the Kyoto University Research Reactor using microdosimetric technique", 115th Scientific meeting of JSMP 2018.04.12 (Yokohama, Japan).

5. Naonori HU, Ryohei UCHIDA, Linh Thuy TRAN, Anatoly Rosenfeld, Yoshinori SAKURAI, "Investigation of SOI microdosimeter in Boron Neutron Capture Therapy" 9th Young Researchers' BNCT meeting 2017.11.13 (Kyoto, Japan).

6. Naonori HU, Ryohei UCHIDA, Linh Thuy TRAN, Anatoly Rosenfeld, Yoshinori SAKURAI, "3D Silicon Microdosimetry for Boron Neutron Capture Therapy: A Simulation Study" 17th Asia-Oceania Congress of Medical Physics 2017.11.04 (Jaipur, India).

7. Naonori HU, Ryohei UCHIDA, Linh Thuy TRAN, Anatoly Rosenfeld, Yoshinori SAKURAI, "Feasibility study of 3D silicon microdosimeters for boron

neutron capture therapy" The 14th Congress on Neutron Capture Therapy 2017.09.29 (Fukushima, Japan).

8. Naonori HU, Ryohei UCHIDA, Linh Thuy TRAN, Anatoly Rosenfeld, Yoshinori SAKURAI, "3D Silicon Microdosimetry for Boron Neutron Capture Therapy: A Simulation Study" 8th Japan-Korea Joint Meeting on Medical Physics 2017.09.16 (Osaka, Japan).

9. Naonori HU, Ryohei UCHIDA, Linh Thuy TRAN, Anatoly Rosenfeld, Yoshinori SAKURAI, "Beam quality determination using 3D silicon microdosimeters for boron neutron capture therapy" Institute for Integrated Radiation and Nuclear Science BNCT scientific meeting 2017.09.01 (Osaka, Japan).

10. Naonori HU, Yoshinori SAKURAI, "To establish a quality control and quality assurance program for patient dosimetry in boron neutron capture therapy" G20 Think 20 Global Solutions Summit 2017.05.29 (Berlin, Germany).

Awards

1. Trainee grant scholarship at IEEE Nuclear Science Symposium and Medical Imaging Conference (NSS/MIC) in Sydney, Australia (2018).

2. Fairchild award at the 18$^{\text{th}}$ International Congress on Neutron Capture Therapy (2018).

3. English presentation award at 115$^{\text{th}}$ Scientific meeting of JSMP (2018).

4. Best oral paper award at the 17$^{\text{th}}$ Asia Oceania Congress of Medical Physics (2017).

5. Young Investigator Award at the 8$^{\text{th}}$ Japan-Korea Joint Meeting on Medical Physics (2017).

6. Kyoto University student short term overseas research scholarship (2017).

7. ACPSEM Richard Bates Travel Scholarship (2017).

Contents

List of Figures

List of Tables

Chapter 1

Introduction

1.1 Introduction to cancer treatment

Cancer is the second leading cause of death globally, and is responsible for approximately 14 million new cases and 8 million cancer related deaths in 2012, affecting populations in all countries and regions [13]. In Japan, cancer has been the leading cause of death since 1981. The number of cancer deaths in Japan in 2017 were approximately 378,000 and the number of cancer incidences were approximately 1 million [14]. Age-adjusted rates of cancer mortality for males increased until the late 1980's, reached a peak in the middle 1990's, and has been decreasing since. The decrease is due to advancement in medical imaging technology which allows detection of early stage cancer, resulting in higher probability of a patient receiving curative treatment. Due to the rapidly advancing technology and new treatment techniques made available for cancer therapy, the mortality rate is expected to reduce even more.

Currently, there are several treatment options available for cancer therapy [15], however, the three main types of therapy are surgery, chemotherapy and radiation therapy. This thesis will focus on the later, radiation therapy.

Radiation therapy uses high doses of radiation to kill cancer cells and shrink tumours. Out of the 14 million new cases diagnosed each year, radiation therapy has the potential to improve the rates of cure of 3.5 million people and provide

palliative relief for an additional 3.5 million people. These estimates are based on the fact that approximately 50 percent of all cancer patients can benefit from radiation therapy in the management of disease; of these, approximately half present early stage to pursue curative treatment [16, 17, 18].

There are two main types of radiation therapy; internal and external radiation therapy. Traditional external radiation therapy uses high-energy gamma rays or x-rays to destroy cancer cells. These high-energy x-rays are irradiated into the patient's body, traversing through the body and reaching the target area (i.e. tumour). Internal radiation therapy uses a radioactive source that is directly placed inside the patient's body. The advantage of internal radiation therapy is the ability to minimise radiation dose to healthy tissue, however, many require undergoing surgical procedure to insert the radioactive source into the body.

In recent years, advancement in technology and computer performance allowed for more advanced treatment techniques to be used, such as intensity modulation radiation therapy and stereotactic radiation therapy. These techniques allow for a much more precise delivery of radiation to the target area, as compared to conventional techniques. It allows shaping of the radiation beam to the tumour area which minimises unwanted exposure of radiation to healthy tissue. However, no matter how well the beam is shaped, there will always be some radiation delivered to normal tissue. The tumour may be located behind (or in front of) a healthy organ and to control the tumour, exposure of the surrounding healthy organs becomes inevitable.

To overcome this problem, proton and heavy ion particles that are generated using a particle accelerator are used. To distinguish between photons and electrons, the term hadron therapy is used. The main difference between protons and heavy ions to high energy x-rays is the dose distribution inside a medium. High energy x-rays penetrate deep into a medium, but the dose absorbed by the medium shows a typical exponential decay with increasing thickness. For protons or heavier ions, the dose increases while the particle penetrates the medium and loses energy continuously, known as the Bragg curve. Immediately before the particle comes to a

rest, there exists a peak known as the Bragg peak. This peak occurs because the interaction cross section increases as the charge particle's energy decreases. Beyond the Bragg peak, the dose drops to zero (for protons) or near zero (for heavier ions). This phenomenon is utilised in radiation therapy, to deliver dose to the tumour volume while sparing the surrounding healthy tissue. With hadron therapy, the treatment of recurrent tumour and areas where radiation therapy had already been delivered can be treated. Also, heavy ion particles have a high LET. The biological response to ionising radiation depends on the type of radiation and is characterised by its relative biological effectiveness (RBE). High LET radiations result in biological damage that is generally larger per unit dose than for x-rays, resulting in an elevated RBE. Hence a lower dose is required to achieve an equivalent effect.

Despite all these advantages high energy x-ray and hadron radiation therapy possess, the dose distribution is in the order of millimetres. In the case where the cancer cell exists inside a normal tissue or if the tumour is directly adjacent to an organ at risk, delivering high dose to these target areas become difficult. A trade-off between curing the cancer or sparing the healthy tissue needs to be made.

1.2 Overview of Boron Neutron Capture Therapy

One type of hadron therapy, called neutron capture therapy (NCT) has the advantage of delivering dose in the order of micrometres. NCT is a technique that was designed to selectively target high LET heavy charged particle radiation to tumours at the cellular level. Soon after the discovery of neutrons by Chadwick in 1932, Goldhaber discovered that ^{10}B has a large thermal neutron capture cross-section. He discovered that immediately after capturing a thermal neutron ^{10}B briefly becomes ^{11}B, then immediately disintegrates into an energetic alpha with a recoiling ^{7}Li ion. The reaction is as follows:

$$
\begin{aligned}
^{10}B + n &\rightarrow {}^{7}Li + \alpha + 2.79 \text{ MeV} \quad (6.3\%) \\
&\rightarrow {}^{7}Li^{*} + \alpha + 2.31 \text{ MeV} \quad (93.7\%) \\
&\hookrightarrow {}^{7}Li + \gamma + 0.478 \text{ MeV}
\end{aligned}
$$

Produced particles have a combined range in tissue of 12 – 13 μm, which is comparable to a human cell dimension, and a combined average kinetic energy of

2.33 MeV. The use of non-radioactive isotope ^{10}B for NCT is commonly known as BNCT. Gordon Locher first proposed the principle of BNCT as early as 1936 [19]. The concept of BNCT is as follows:

1. The boron drug compound is selectively concentrated in a tumour.

2. Low energy neutrons (thermal or epithermal) are delivered to the tumour from outside the body.

3. Thermal neutrons are captured by the ^{10}B inside the tumour, resulting in short ranged alpha and lithium ions delivering high dose within the tumour.

The cross section of ^{10}B is shown in figure 1.1. The cross-section for thermal neutrons (0.025 eV) is about 3840 barns. So hence, it is ideal to irradiate the tumour loaded with ^{10}B using thermal neutrons. Using a direct thermal neutron flux is suitable for superficial tumours. For deep-seated tumours, a slightly higher energy neutron (0.025 – 0.4 eV) called epithermal neutrons are used. The thermal neutron flux at different mono energetic neutron energies as it traverses through a cylindrical water phantom is shown in figure 1.2. For a thermal neutron with average energy of 0.025 eV, the peak thermal neutron flux occurs about a few millimetres from the surface. The epithermal neutrons interact with the hydrogen atoms inside the water, losing energy as it traverses through the medium and becomes a thermal neutron. The peak thermal neutron flux occurs at a depth of about 3 cm. The thermal neutron peak for fast neutrons occur even deeper than epithermal neutrons, however, the probability of fast neutrons to reduce to thermal neutrons inside the medium is low.

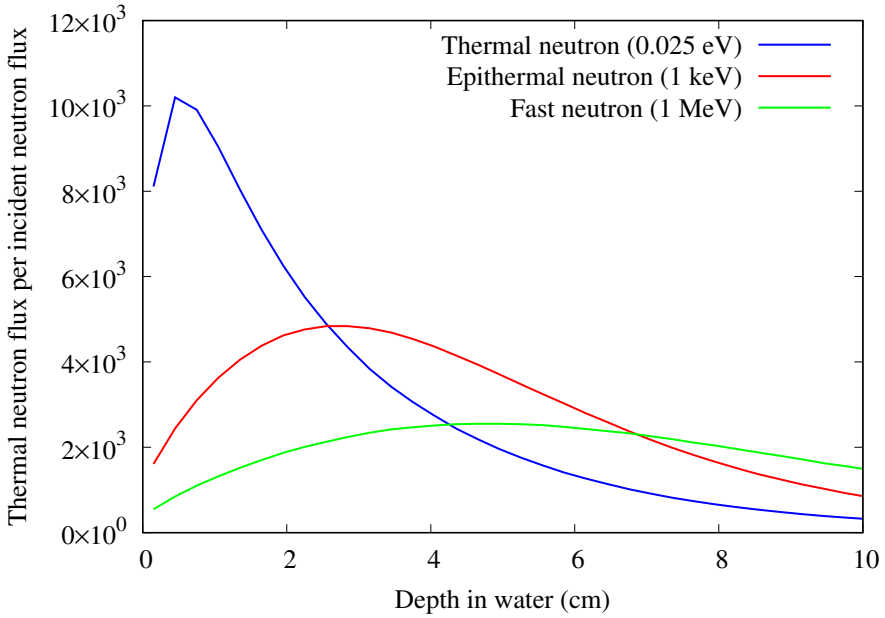

Figure 1.2: Thermal neutron flux inside a cylindical water phantom when irradiated by mono energetic neutrons of different energies, calculated using PHITS Monte Carlo system.

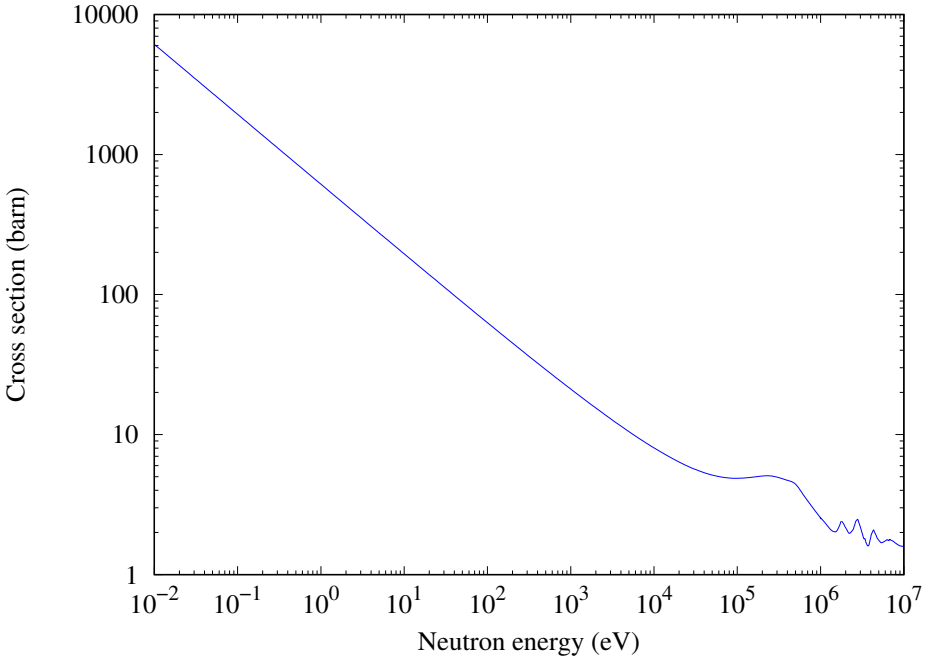

Figure 1.1: ^{10}B(n,α)^{7}Li cross section as a function of neutron energy [1]

So far, clinical practice has relied on two main boron-based drugs; sodium borocaptate ($Na_2B_{12}H_{11}SH$) (BSH) and a phenylalanine dihydroxy-boryl derivative, known as Boronphenylalanine (BPA) [20]. The essential difference is how it is ac-

cumulated and distributed within a tumour cell. BSH has a series of boron clusters. BSH cannot penetrate the blood brain barrier (BBB), however, the BBB is damaged in tumour regions which allows the BSH to penetrate and accumulate in malignant tumour regions. BSH does not actively accumulate in cancer cells. BPA has an amino acid structure. BPA was initially used in malignant melanoma research. The application of BPA for BNCT showed promising results and through fluro-borono-phenylalanine positron emitting tomography (FBPA PET) imaging, it was discovered that the compound only accumulates in malignant melanoma, but also in various malignant tumours [21]. BPA differs significantly from BSH in that it selectively accumulates in cancer cells.

With development in boron drugs, the use of BNCT has expanded. For areas where conventional external beam radiation therapy is not suitable, BNCT can be performed. For patients with no other available form of cancer therapy, BNCT can be performed to extend their quality of life (QOL). With further progression in BNCT research, it will have a vital role in radiation therapy.

1.3 History of BNCT

Soon after the discovery of the neutron, G.L. Locher recognised the potential of this discovery and suggested that neutron capture could be used to treat cancer [19]. Between 1950 and early 1960, the first clinical trials of BNCT was performed at Massachusetts General Hospital (MGH) and at the Brookhaven National Laboratory (BNL) using thermal neutrons, led by neurosurgeon W. H. Sweet [22, 23]. The outcome of the clinical trial demonstrated no significant prolongation of life nor evidence of therapeutic efficacy. To improve the clinical outcome, MGH initiated a third trial of BNCT at the Massachusetts Institute of Technology Research Reactor (MITR-I). However, similar outcome with no evidence of any prolongation of survival was found. Due to no significant improvement, the BNCT program can to a halt.

H. Hatanaka, after being mentored in BNCT research at MGH for several years, pioneered clinical BNCT for brain tumours in Japan in 1967 [24, 25]. Between 1968

and 1975, Hatanaka performed BNCT clinical trials for melanoma using the Hitachi Training Reactor (HTR) [26]. In 1975, the Heavy Water Thermal Neutron Facility at Kyoto University Reactor (KUR) was developed for biological irradiation. In the same year, HTR was permanently closed and to continue BNCT, a medical reactor was necessary. The KUR reactor was a suitable candidate, however, this was the only reactor utilised for joint research among other universities and preschedules reactor operation program for six months prevented the use of scheduling patients [27]. The Musashi Institute of Technology Reactor (MITR) became the next medical reactor for BNCT [28]. At the time, the reactor power was not high enough, 100 kW. Through experience from the HTR and results from KUR experiments, the MITR was remodelled to produce high flux of thermal neutron suitable for clinical use. Thermal neutrons are not suitable for the treatment of deep-seated tumours. To overcome this issue, craniotomy was performed in theatre and then the patient was transported to the irradiation room. In 1990, KUR and the research reactor at Japan Nuclear Energy Agency (JAEA) was regularly utilised for clinical BNCT [29, 30]. At the same time, research had been performed at the United States to produce intermediate energy neutrons for treatment of deep-seated tumours using NCT [31]. The epithermal beam was successfully developed at BNL and MIT reactor and clinical studies recommenced in 1994 [32, 33].

In 1996, KUR was modified to produce a wide range of neutron spectrum, ranging from almost pure thermal neutrons to epithermal neutrons [34]. The new facility is called KUR Heavy Water Neutron Irradiation Facility (KUR-HWNIF). In 1998, the research reactor at JAEA also underwent modification to produce epithermal neutrons [35, 36]. Up until 2001, craniotomy with thermal neutron irradiation has been primarily performed [37], however, from 2002 onwards, epithermal neutron irradiation without craniotomy started to become the standard treatment form for BNCT [38]. In 2001, the world's first recurrent cancer of the parotid gland treatment was performed with positive result. Following this, treatment area expanded to brain and head and neck tumours [39, 40]. In 2005, clinical trials have expanded

to extracranial regions such as liver, lung and pleural mesothelioma cancer [41, 42]. Although there were several interruption periods, over 500 clinical irradiations had been carried out using the reactor as of November 2014.

In countries, other than Japan and the United States, clinical trials using epithermal neutrons at the High Flux Reactor (HFR) in Petten began in 1997 [43]. Following this, Finland (1999) [44], Czech Republic (2000) [45, 46], Sweden (2001) [47], Italy (2002) [48], Argentina (2003) [49] and Taiwan (2010) [50] began BNCT clinical trials. Recently, a low power in-hospital compact nuclear reactor has been designed and built in Beijing, China to treat cutaneous melanomas [51]. With advancement in technology and positive clinical outcomes, the popularity and users of BNCT are increasing worldwide.

1.4 KUR BNCT

The KUR-HWNIF utilises a 5 MW full power reactor. The beam spectrum is adjusted using heavy water, Boral and cadmium filters. In order, it consists of the reactor core, epithermal neutron moderator (80%/20% volume ratio of aluminium and heavy water, total thickness of 66 cm), a neutron energy spectrum shifter (consists of three D_2O tanks, 10, 20 and 30 cm thick), a 30 cm D_2O water shutter, two thermal neutron filters (consisting of 1 mm Boral and 6.4 mm cadmium plates), and an adjustable bismuth layer typically 18.4 cm thick [34]. Various irradiation modes are made available by having the cadmium and Boral filters open or closed, full or empty heavy water in the neutron energy spectrum shifter and heavy water shutter tanks, and the thickness of the centre part of the bismuth layer. An example of the irradiation mode coding scheme is shown below.

- CB-1111-F-E1: All filters in place with D_2O tanks full.
- OO-0000-E-E1: All filters open with D_2O tanks empty.

The first and second characters in the symbol defining irradiation mode represent open or closed conditions of the cadmium and Boral filters. The next four digits

represent the conditions of the tanks of the heavy water shutter and the spectrum shifter, where "0" represents empty and "1" indicating full. The last character represents the condition of the centre thickness of the bismuth layer. The characters "E", "G", "F" and "H" represent 0, 5, 18.4 and 23.4 cm of bismuth, respectively. The most commonly utilised bismuth layer is 18.4 cm. There are three standard irradiation modes at KUR for BNCT:

1. Thermal neutron irradiation mode, OO-0011-F.
2. Epithermal neutron irradiation mode, CO-0000-F.
3. Mix neutron irradiation mode, OO-0000-F.

The thermal and epithermal neutron irradiation mode is currently utilised for clinical treatment. The mix neutron irradiation mode is utilised for research. Present day, the Boral filter is no longer in use. In replacement, two cadmium filters are used.

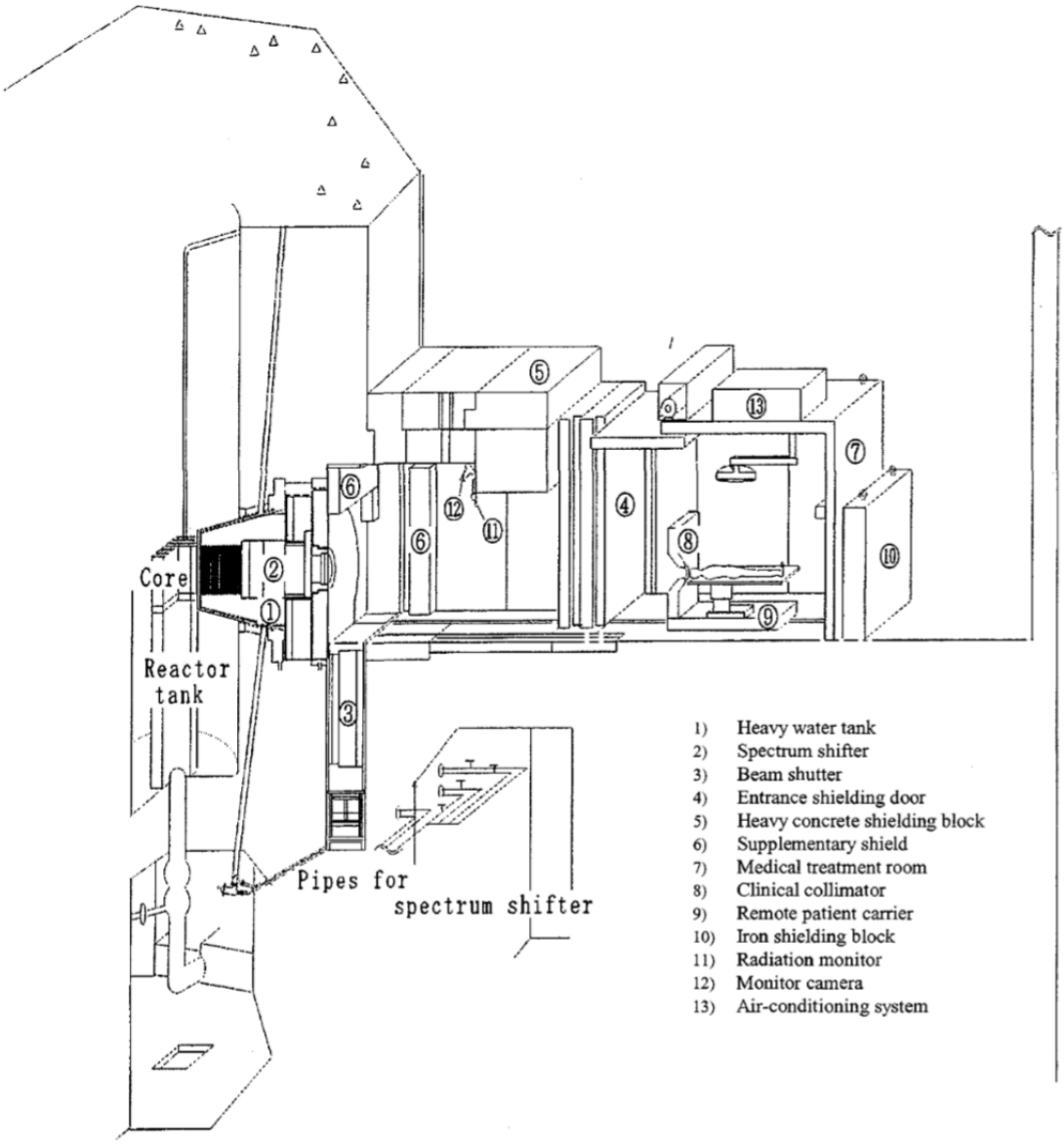

Figure 1.3: Layout of the KUR HWNIF

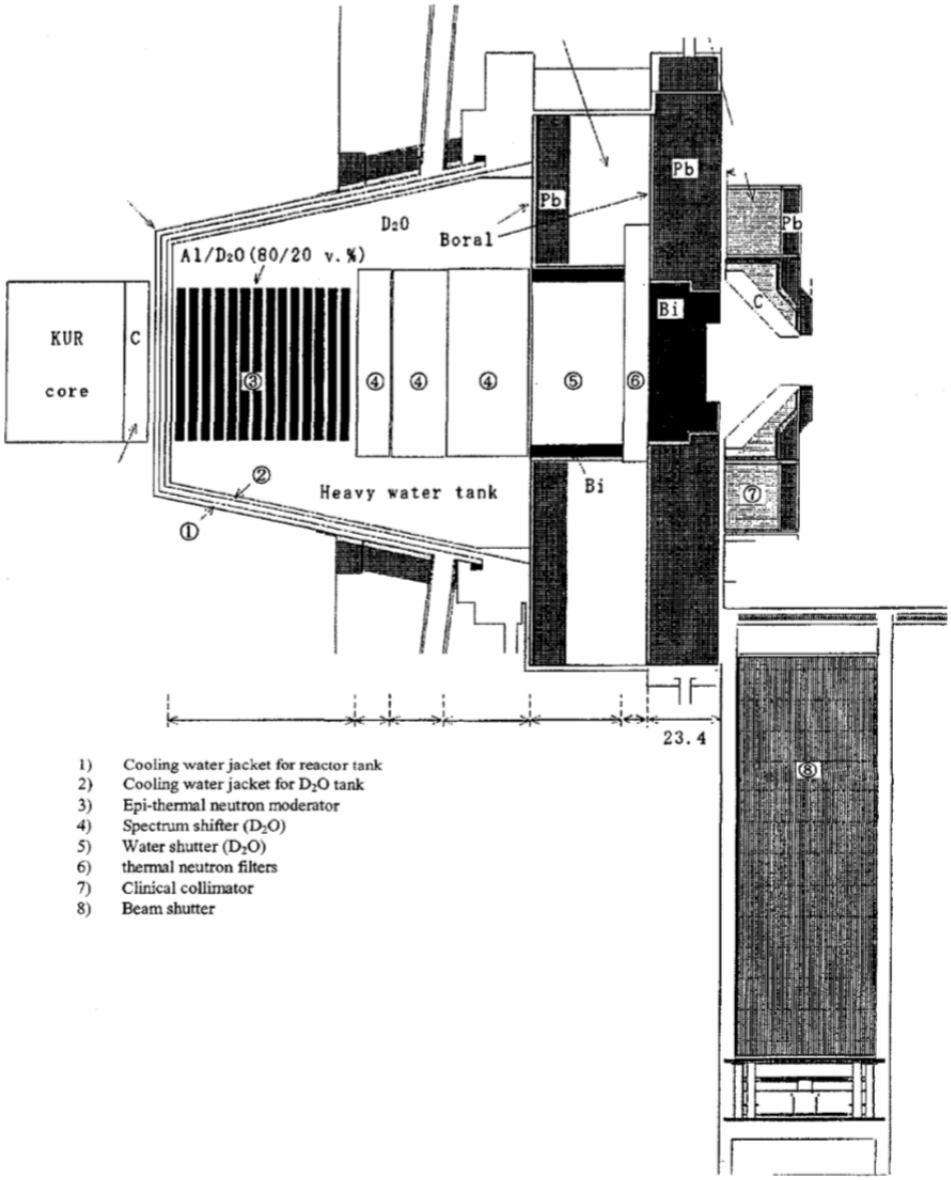

Figure 1.4: Cross-section of the KUR HWNIF

1.5 Accelerator BNCT

The recent trend is to step away from reactor-based and transition to accelerator-based BNCT systems (AB-BNCT). Several AB-BNCT facilities are being designed, constructed and tested at various centres around the world. The transition is motivated because reactor-based systems are more costly, difficult to operate, licensing issues, and, more importantly, they are not suitable for installation in a hospital environment. To promote BNCT and make it available for standard therapeutic op-

tion, a safe, simple and low-cost system is necessary. Research of AB-BNCT started in the early 1980's in the United States and in 1994, the first international workshop on AB-BNCT was held in Jackson, WY. Most AB-BNCT systems utilise an intense proton beam accelerated using a cyclotron directed at a lithium or beryllium target to generate neutrons. Without considering the engineering element, the optimal target for low energy neutron production is lithium. It has a high neutron yield and the kinetics are such that the secondary neutron spectrum is relatively low energy. Many of the early AB-BNCT systems utilised a lithium target [52, 53, 54, 55]. However, pure lithium targets are problematic as it has a low melting point (180°C), low thermal conductivity (44 W/mC) and it is chemically reactive with air. Due to these limitations, several groups decided to utilise beryllium as a neutron producing target [56, 57]. Although beryllium targets have a lower neutron yield at a given proton energy, it has a much higher melting point (1278°C) and thermal conductivity and is less reactive to air. To obtain a similar neutron yield obtained from using a lithium target, the required incident proton energy is approximately 4 MeV (compared to 2.5 MeV for lithium targets). A beryllium target is simpler in terms of target configuration, however, the cost increases along with the complexity of the accelerator system to produce a higher proton energy. In Japan, AB-BNCT research has been performed primarily at Kyoto University Research Reactor Institute (currently known as Kyoto University Institute for Integrated Radiation and Nuclear Science) and Tohoku University [58, 59]. In early 2009, the world's first AB-BNCT system for clinical irradiation, known as Cyclotron-Based Epithermal Neutron Source (C-BENS) was developed under collaboration with Sumitomo Heavy Industry and Stella Pharma company [60]. The system uses a 30 MeV proton beam with a beryllium target. The high-energy neutrons generated are moderated to thermal and epithermal neutrons through a moderator that consist of lead, iron, aluminium and calcium-fluoride. The thermal neutron and gamma ray flux are reduced by cadmium and lead filters, respectively, resulting in an epithermal neutron beam suitable for BNCT. Clinical trials using C-BENS had started in 2012. Since

the 2011 earthquake off the pacific coast of Tohoku, referred to in Japan as the Great East Japan Earthquake, research reactors throughout the country were temporarily put on halt and strict regulatory control and maintenance were put in place. Thus, installation of new research reactors for BNCT has become extremely difficult and the need for AB-BNCT systems is increasing. A summary of the currently installed (and under construction) AB-BNCT systems worldwide, as of 2014 extracted from [12] are shown in table 1.1. From this table it can be seen that a linear accelerator type machines are more common than cyclotron-based systems.

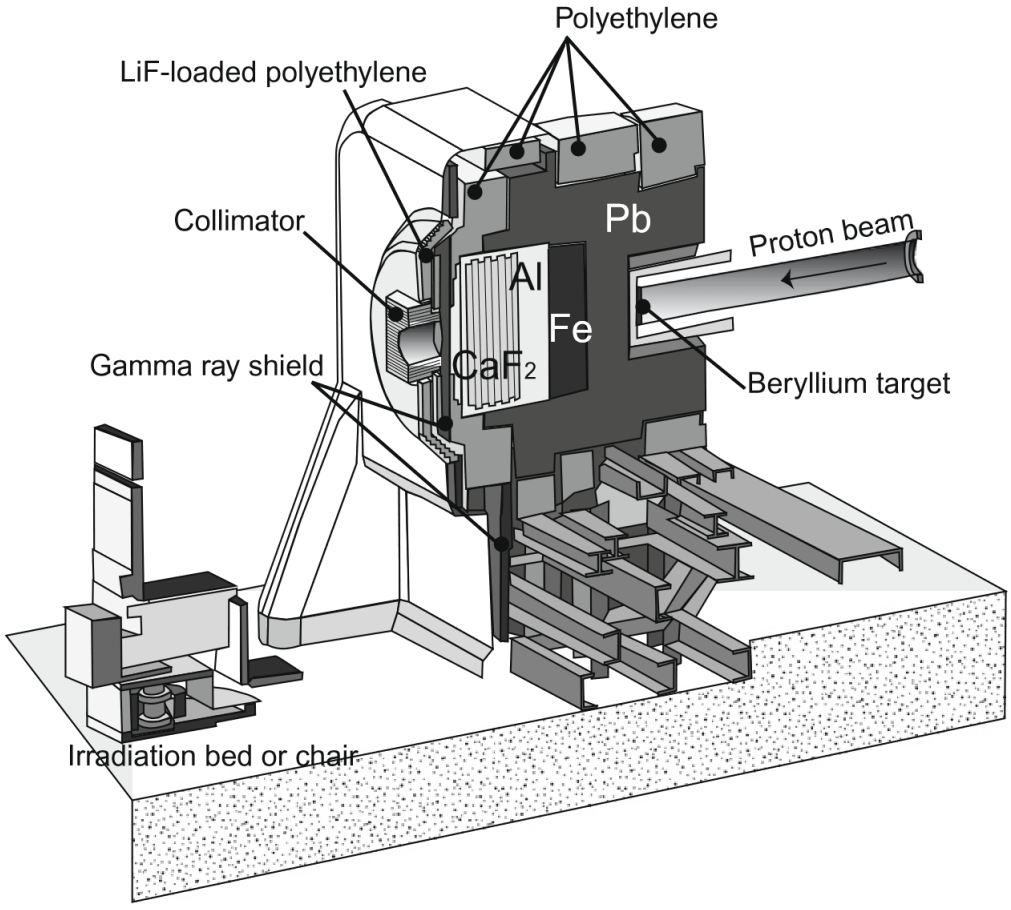

Figure 1.5: Layout of the 30 MeV proton cyclotron based BNCT (C-BENS) at Kyoto University.

Table 1.1: Current status of the different accelerators intended for AB-BNCT facilities worldwide, data taken at 2014 [12]

Institute - Location	Machine (status)	Target and reaction	Neutron energy (MeV)	Beam current (mA)
Budker Institute, Russia	Vacuum insulated Tandem (ready)	Solid^{7}Li(p,n)	2.0	2
IPPE-Obninsk, Russia	Cascade generator KG-2.5 (ready)	Solid^{7}Li(p,n)	2.3	3
Birmingham Univ., UK	Dynamitron (ready)	Solid^{7}Li(p,n)	2.8	1
KURNS, Japan	Cyclotron (clinical trials started)	^{9}Be(p,n)	30	1
Soreq, Israel	RFQ-DTL (ready)	Liquid^{7}Li(p,n)	4	2
INFN Legnaro, Italy	RFQ (under construction)	^{9}Be(p,n)	4-5	30
Tsukuba, Japan	RFQ-DTL (under construction)	^{9}Be(p,n)	8	10
CNEA, Buenos Aires	Single ended ESQ (under construction)	^{9}Be(p,n)	1.4	30
Argentina	Tandem ESQ (under construction)	Solid^{7}Li(p,n)	2.5	30

1.6 Microdosimetry

Microdosimetry is an essential tool to understand the safe and effective use of radiation for both clinical and industrial purposes. Rossi and Zaider formally define microdosimetry as "the systematic study and quantification of the spatial and temporal distribution of absorbed energy in irradiated matter". Microdosimetry is a dosimetry technique designed to measure the stochastic interactions of ionising radiation on cellular and sub cellular level. Stochastic interactions occur randomly and hence cannot be predicted deterministically. The microdosimetric quantities were given in ICRU report 36. Experimental microdosimetry is based on stochastic quantities such as energy imparted ϵ, specific energy z and lineal energy y. The energy imparted is defined as the summation of all the energy deposited in a defined volume.

$$\epsilon = \sum_i \epsilon_i \tag{1.1}$$

The specific energy z is defined as the quotient of the energy imparted ϵ by ionising radiation to a matter by its mass m:

$$z = \frac{\epsilon}{m} \tag{1.2}$$

The units of specific energy are J/kg or Gy.

The microdosimetric quantity used to describe the energy imparted to teh matter in a volume of interest by a single energy deposition event ϵdivided by $\bar{l}$is called lineal energy y:

$$\bar{l} = \frac{4V}{S} \tag{1.3}$$

where V is the volume and S is the surface area of the volume.

If $F(y)$is the probability that the lineal energy is equal to or less than y, the probability density or lineal energy distribution $f(y)$ can be determined by:

$$f(y) = \frac{dF(y)}{dy} \tag{1.4}$$

The frequency weighted mean lineal energy is a non-stochastic quantity given by:

$$\bar{y_F} = \int y f(y)\, dy \tag{1.5}$$

If $D(y)$is the fraction of an absorbed dose with a lineal energy equal to or less than y, $d(y)$is the dose probability density and can be determined by:

$$d(y) = \frac{dD(y)}{dy} = \frac{1}{\bar{y_F}} y f(y) \tag{1.6}$$

The dose weighted mean lineal energy is given by:

$$\bar{y_D} = \int y d(y)\, dy \tag{1.7}$$

The dose weighted mean lineal energy can also be expressed as:

$$\bar{y_D} = \frac{1}{y_F} \int y^2 f(y)\, dy \tag{1.8}$$

Microdosimetric spectra are usually presented in log scale because the lineal energy and its distribution span through a wide range of y values. To graphically To graphically display the spectrum, $yf(y)$versus $\log(y)$ is used and presented as:

$$\int_{y_1}^{y_2} f(y) dy = \int_{y_1}^{y_2} [y f(y)]\, d\log(y) \tag{1.9}$$

With knowledge of the microdosimetric spectra, the dose equivalent used in radiation protection can be derived using:

$$H = D \int Q(y) y^2 f(y) d(\log(y)) \tag{1.10}$$

where $Q(y)$ is a quality factor obtained from the radiobiological experiments and D is the absorbed dose.

1.7 Radiobiological model

When cells are exposed to ionising radiation, their structure is damaged. If the damage cannot be repaired or when they are incorrectly repaired, it causes cell death. The concept of radiobiology is to investigate the dose response relationship at the cell level. The survival fraction of cells is measured and typically plotted on a logarithmic scale against dose on a linear scale, commonly known as the cell survival curve. The classical model describing such dose response relationship is the linear quadratic model (LQ model). The LQ model is a mathematical model used to predict the survival levels at different doses for different types of ionising radiation.

$$S(D) = exp(-\alpha D - \beta D^2) \tag{1.11}$$

The parameters α and β represent the cellular radiosensitivity to fractionation. In classical radiobiology the α/β ratio is an important parameter to characterise the cell radiosensitivity [61]. There are many factors that affect the cell killing efficiency. One parameter is the radiation type. Low LET radiation (LET $<$ 10 keV/µm) are X-rays, gamma rays or light charged particles (e.g. electrons). Other radiations, such as neutrons or heavy charged particles are high LET radiation (LET $<$ 10 keV/µm). The difference between the two is the distribution of ionising events on a micron-scale. Low LET radiation events are distributed far apart, where high LET radiations are densely distributed [62]. To quantify the difference of cell killing efficiency of low and high LET radiation, the concept of relative biological effectiveness (RBE) was introduced. RBE is the ratio of biological effectiveness of one type of ionising radiation relative to another, given the same amount of absorbed energy.

$$RBE = \frac{D_X}{D_R} \tag{1.12}$$

where $D_X$is a reference absorbed dose of radiation of a standard type (usually X-rays) and $D_R$is the absorbed dose of a radiation type R that causes the same amount of biological damage. There are several models from clinical, mechanistic

and microdosimetric methods to derive RBE. Neutron therapy was one of the first treatment modalities using high LET particles. Kellerer and Rossi [63] proposed the theory of dual radiation action (TDRA) to understand the RBE values as a function of dose per fraction for high LET radiations. This theory is based on the idea that lesions are created from pairs of sub-lesions. When pairs of sub-lesions occur in a defined sensitive site, it results in a biological effect. Hence, biological effects are correlated with the energy deposited in a defined sensitive site. However, TDRA does not consider the probability of cell repair after irradiation. This led to the introduction of microdosimetric based and repair kinetic models to estimate the biological effect, which is known as the microdosimetric kinetic model (MKM). The MKM was first proposed by Hawkins [64, 65] to overcome the shortcomings of the TDRA. The model is based on a sub-cellular structure referred to as a domain. The domain has a spherical shape and were introduced to set the restricted region in a cell nucleus as a pair of sub-lethal lesions created near each other by a single event that produces a lethal lesion. It is based on microdosimetric quantities measured with a proportional counter and on the statistical aspect of dose deposition. Later Kase et al. [66] proposed a modified version for carbon ion therapy at National Institute of Radiological Sciences (NIRS), Japan. At the end of 2011, the first patient was treated at NIRS with the spot-scanning beam calculated using a new treatment planning system that incorporated the MKM [67]. The Local Effect Model (LEM) was introduced by Scholz and Kraft [68]. The fundamental of LEM is that the cell inactivation after irradiation is determined by the spatial local dose distribution inside the cell nucleus. LEM assumes lethal effects are independent of the radiation quality, but instead depend on the track structure produced in the sub volume of these lethal events. Sub volumes are where the biological damages are calculated, are integrated to estimate the total survival probability. At GSI Helmholtz Centre for Heavy Ion Research, the active beam scanning system was implemented to allow for a better dose conformity. With this technique, the biological effectiveness is unique for each spot scan and voxel. Therefore, a mathematical model to calculate

RBE was preferred. The LEM was developed for this purpose. This approach in RBE calculation can only be verified with radiobiological experiments, while MKM approach is based on experimental measurements of the microdosimetric spectra followed by RBE derivation.

1.8 Current challenges in BNCT quality assurance and quality control

Since 2010, the reactor at KURNS has resumed treating patients and in 2012, clinical trials using C-BENS has started. The number of patients is increasing and the popularity of BNCT is on the rise. To develop BNCT as a standard radiotherapy treatment, there is a need to establish a proper QA and QC system. In conventional radiotherapy, there are numerous steps (diagnosis, treatment planning, treatment, post treatment evaluation). At each step, there should be a QA and QC protocol put in place to ensure the safety and accuracy of the whole system. The American Association of Physicists in Medicine (AAPM) report number 13, Physical aspects of quality assurance in radiation therapy, states "The therapeutic system should be capable of delivering a dose to the tumour volume within 5% of the dose described" [69]. For the current standard radiotherapy modality, high energy photons and electrons, once it interacts with the human tissue, the dominant particle responsible for cell damage are the secondary electrons which has RBE of unity. On the other hand, in a BNCT field, there exists neutrons with energy below 0.5 eV (thermal neutrons), neutrons with energies between 0.5 eV and 40 keV (epithermal neutrons) and neutrons with energy above 40 keV (fast neutrons). Adding the gamma ray component, this makes it 4 individual components where each interacts differently with tissue and the generated secondary particles all have differing RBEs. Therefore, as mentioned by Blue et al. [70], the RBE of a neutron field varies with the energy. Due to the above reason, applying a similar approach to utilise the currently established QA/QC protocols for high energy photon/electron radiotherapy

for BNCT purposes is no simple task. It is important to understand the differences between the modalities and build a QA/QC protocol to suit the needs of BNCT.

1.9 Dose calculation in BNCT

The total dose delivered to a patient receiving BNCT is calculated by multiplying the absorbed dose of each radiation component present in the field with the corresponding RBE and taking the sum. This is known as the equivalent dose and has a unit of Gy. To calculate ^{10}B dose, a factor called Compound Biological Effectiveness (CBE) is used instead of RBE. CBE considers the boron distribution inside a cell and is dependent on the boron compound type and the type of tissue being evaluated. Total dose delivered in BNCT is given by the following equation:

$$D_T = CBE \times D_B + RBE_N \times D_N + RBE_H \times D_H + RBE_\gamma \times D_\gamma \tag{1.13}$$

where D represents the absorbed dose from each component listed below.

1. D_T is the total biologically weighted dose.
2. D_B is the absorbed dose from the $^{10}B(n,a)^7Li$ reaction which occurs when a thermal neutron is captured by boron (boron dose)
3. D_N is the absorbed dose from the $^{14}N(n,p)^{14}C$ reaction which occurs when a thermal neutron is captured by nitrogen (nitrogen dose)
4. D_H is the absorbed dose from the recoil products (mainly protons) which occurs when a fast neutron collides with the nucleus of the target (hydrogen dose).
5. D_γ is the absorbed dose from $^1H(n,\gamma)^2H$ reaction and gamma ray components existing in the beam itself (gamma dose).

RBE_N, RBE_H and RBE_γ are RBE values of nitrogen, hydrogen and gamma rays, respectively. The absorbed dose resulting from neutrons interacting with hydrogen and nitrogen inside the body (D_H, D_N) are multiplied with RBE values of 2.5 - 3.0. The RBE for gamma rays is 1. When BPA is used with a ^{10}B concentration of 25 ppm, the CBE factor used is 1.35.

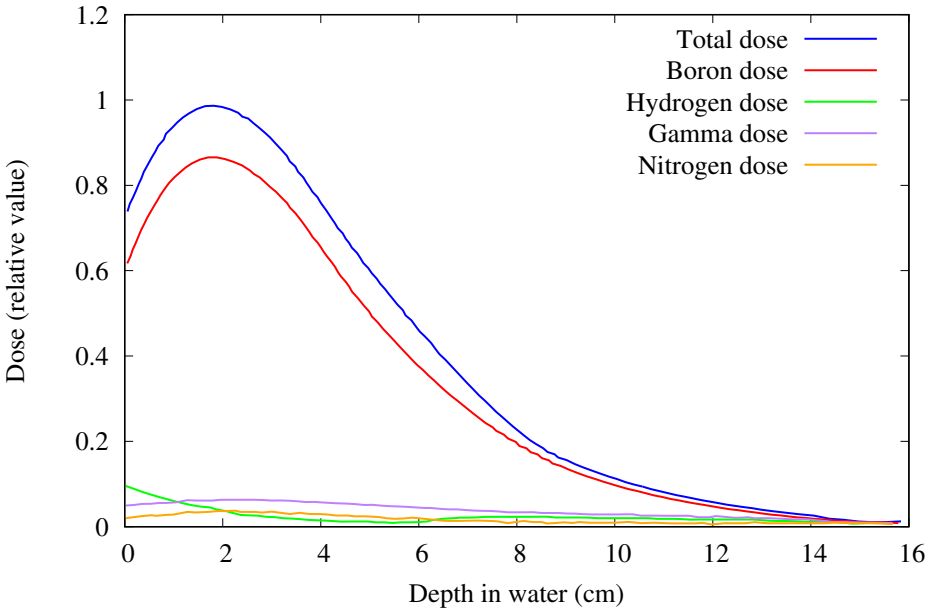

Figure 1.6: Relative depth dose distribution of each radiation component present during BNCT [2]

Chapter 2

Literature review

2.1 Experimental microdosimetry

In general, microdosimetry involves the study of energy depositions that occur in micro-volumes of the size of cellular and sub-cellular structures. Early studies to understand the cellular radiation effects concluded that knowledge of the energy distribution at a cellular scale was essential [71]. In the 1920s, Dessauer [72] and Crowther [73] developed target theory in its earliest form that dealt with discrete acts of energy transfer, termed hits. This theory did not consider the spatial distribution of these events, therefore, could not explain the relative biological effectiveness (RBE) of different types of ionising radiation. Between late 1930s to late 1940s, several important concepts to characterise radiation quality was developed [74, 75]. Lea [76] introduced the term "energy dissipation" which was later called "linear energy transfer", LET by Zirkle et al. [77]. ICRU report defines LET as a measure of the loss of energy per unit distance along the path of a charged particle [78]. However, there are several limitations of the LET concept in explaining RBE and beam quality. Kellerer and Chmelevsky [79] investigated the effects of these limitations and the ranges and energies over which they are important. The limitations of the LET concept is described in detail in ICRU report 36 [80] and a summary is described below:

1. The delta ray energy distribution is not adequately considered. In a microscopic volume, delta ray distribution is a significant factor in determination of spatial distribution of energy.

2. The limited ranged of the charged particles relative to the target size influences the spatial distribution of energy. Such effect is more predominant at lower ion energies and in sites with a large dimension.

3. The concept of LET, being a non-stochastic average quantity, does not account for the random fluctuations in energy deposition.

These limitations led to the formulation of a set of measurable stochastic quantities that provide the fundamental basis for the field of microdosimetry. These quantities are lineal energy and specific energy. These quantities were explained in the previous chapter. The goal of experimental microdosimetry is to measure these quantities in well-defined volumes.

2.2 Tissue equivalent proportional counter

The first TEPC was developed by Rossi and Rosenweig to simulate the measurement of energy deposition in volumes of tissue with dimensions similar to the nucleus of a mammalian cell [81]. It employed a spherical chamber with tissue equivalent walls and fill gas. The spherical shape was selected so that its response would be less independent of the angular direction of which the incident radiation that enters the chamber. The cavity diameter ranged from 6 mm to 20 cm. A metal anode wire sits across the internal diameter of the chamber and a bias was applied between the chamber wall and the collecting anode [82]. A helical anode structure, as oppose to a straight wire, was used to ensure a uniform electric field, particularly toward the edges near the chamber wall. Currently, the primary tool of experimental microdosimetry is a low-pressure proportional counter. The walls of the counter are commonly made of tissue equivalent material. The development of TEPC has been motivated by the increasing application of neutron and proton therapy worldwide.

Also, the interest of understanding of the biological effects of densely ionising radiation. In the past few years, several research groups have developed various types of mini TEPCs. Kliauga measured single event distributions using a single-wire mini TEPC with a diameter of 0.5 mm [83]. Cesari et al. measured the distribution of a proton therapeutic beam with a mini TEPC of 1 mm diameter [84]. Burmeister et al. applied a mini TEPC to measure the distribution in a high-flux mixed fields [85]. Moro et al. utilised a mini twin TEPC for BNCT dosimetry [86]. However, the construction of a central wire in a small cavity is extremely difficult and expensive.

2.3 Silicon microdosimeter

McNulty and Roth proposed the use of an array of silicon reversed biased p-n junctions for characterising complex radiation environments inside a spacecraft and aircraft [87]. The purpose of this work was aimed towards predicting single event effect (SEE) risks to the microelectronics caused by incident radiation. The operation of these microelectronics involves the selected storage and switching of various electrical charges at the given junction. When ionising particles enter the junction, they cause a change in bias across the junction which induces a change to the electrical state of the circuit, which is referred to as an 'upset'. Upset phenomena are 16 significant concerns in the microelectronic field, especially in the space technology area where there is microelectronics constantly exposed to ionising radiation fields. Roth later developed a working model containing more than a million sensitive volumes, however the device has been used for qualitative separation of neutron and gamma fields using an MCA for observation of the two groups of events with low and higher LET without any quantification of these fields and deriving of microdosimetric quantities [88]. Such a detector removed several of the previously mentioned problems associated with the tissue equivalent proportional counters but was not considered a microdosimeter. The Centre for Medical Radiation Physics (CMRP), University of Wollongong (UOW) firstly developed a solid state microdosimetry device to overcome the limitations of the TEPC (A.Rosenfeld et al.) [89]. Later, Rosenfeld came

up with an idea of silicon on insulator (SOI) solid state microdosimeter [90]. This development was driven primarily by an application in hadron therapy and in particular in BNCT [3] and proton therapy [91] and later for space application where heavy ion radiation fields such as GCR (galactic cosmic rays) [92] is a serious hazard for space missions. The first generation of SOI microdosimeter consisted of an array of reverse biased semiconductor p-n junctions each with a sensitive volume of 30 $\times$ 30 $\times$ 10 μm^3 in size and all are connected in parallel [4], as shown in figure 2.1. Studies of the charge collection characteristics of these devices found that the charge collection efficiency of the device varied with the position of the incident particle around the sensitive volume of the detector. This was due to the lateral distribution of the electric field within the planar RPP sensitive volume and diffusion of charge into the sensitive volume from the outside [3, 93]. The rectangular geometry of the sensitive volume also gave rise to poor chord length variance that led to an overestimation of energy deposited within the sensitive volume. The first generation of silicon microdosimeter was not perfect and there were still some areas where improvement was required. The main imperfections of silicon microdosimeter were a poorly defined sensitive volume, inaccurate tissue equivalence, lateral diffusion from outside the volume and the present limitations of device fabrication.

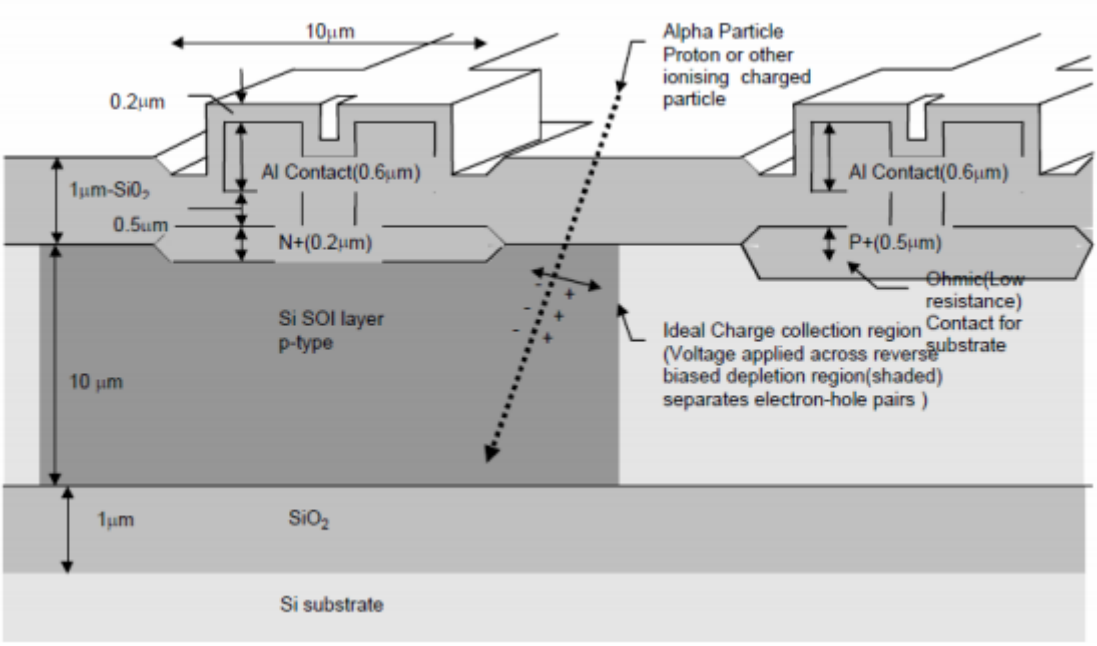

Figure 2.1: Detailed cross sectional view of the SOI microdosimeter sensitive volume fragment with approximate dimensions. Image from [3].

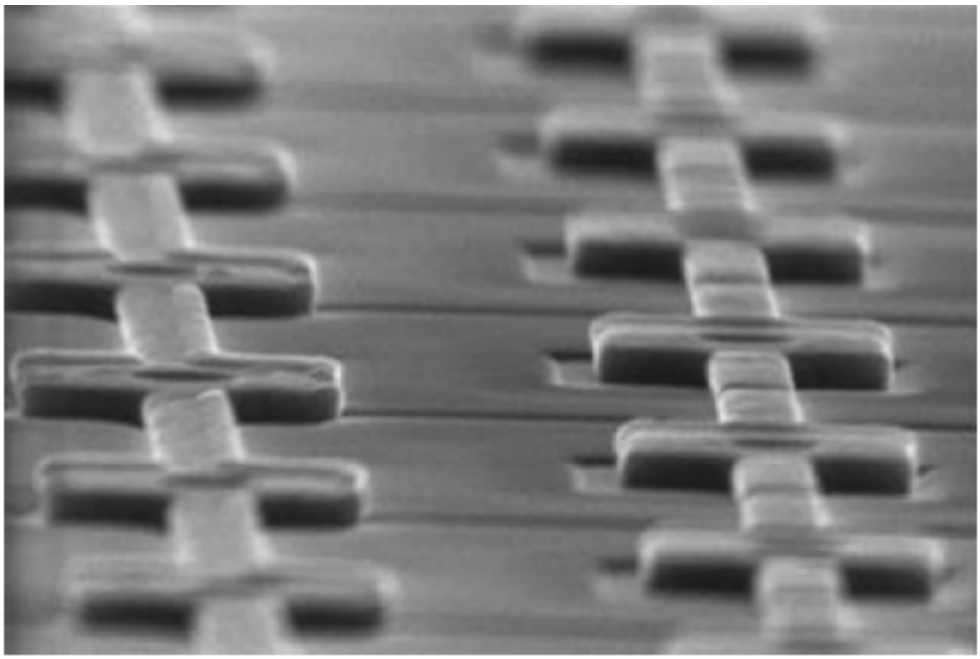

Figure 2.2: Scanning Electron Microgram (SEM) of a section of the SOI microdosimeter showing the raised aluminium tracks. Image from [4].

The CMRP designed, and in collaboration with the University of New South Wales (UNSW) and Australian Nuclear Science and Technology Organisation (ANSTO) fabricated and characterised a new type of silicon microdosimeter to overcome the problems addressed with the previous generation microdosimeter. The new type of

microdosimeter was based on an array of 3D cylindrical p-i-n diode sensitive volumes. Each diode is on a mesa structure above the substrate, which prevents the lateral diffusion of charge from the surrounding area. These devices were fabricated at the Semiconductor Nanofabrication Facility, UNSW, Australia [5], as shown in figure 2.3. It involved planar processing techniques on high resistivity, more than 10 kΩ·cm p-silicon on insulator (SOI) bonded wafer. Phosphorus and boron were diffused into the silicon wafer to produce the co-axial p-i-n diode structures. An etching process was used to create the raised mesa structure sensitive volumes, 2 μm in thickness. A spherical semiconductor microdosimeter would be ideal to mimic a human cell, however such geometry is very difficult to achieve with the current fabrication technology. Therefore, a cylindrical geometry was used to fabricate the second generation microdosimeters. The cylindrical geometry produces a better chord length variance when compared to the first generation microdosimeter with elongated rectangular geometry. The cylindrical volume supports a radial electric field distribution that improves efficiency of the collection of all deposited charge. Two types of the second-generation microdosimeter were designed and fabricated on silicon-on-insulator with a superficial silicon layer thickness 2 μm, one with the intrinsic silicon width of 2 μm and another with 10 μm. The cylindrical sensitive region area of the 2 μm and 10 μm width devices are approximately 50 μm^2 and 500 μm^2 respectively. This microdosimeter consists of an array of 900 individual diodes connected in two parallel odd-even arrays so that every single odd connected diode is surrounded by four identical even-connected diodes, read out independently from the odd array, as shown in figure 2.4. This allows a dual-channel read out which has the potential to identify different high energy particles of the same linear energy transfer based on their different track structure. The array structure increases the total area of the sensitive volume to approximately 45000 μm^2. Although tests showed the reduction in lateral diffusion, the effective yield of the sensitive volumes was not 100% due to the technological challenges related to track interconnects between the sensitive volumes in case of mesa structures.

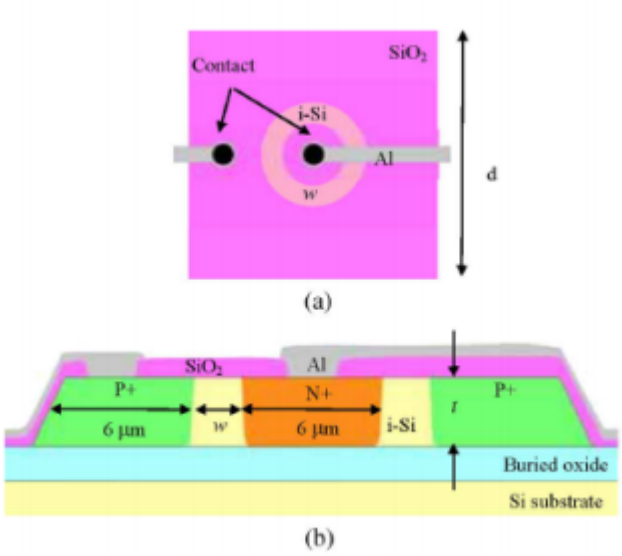

Figure 2.3: Schematic view of the second generation microdosimeter (a) top view (b) cross sectional side view. Not drawn to scale. Image from [5].

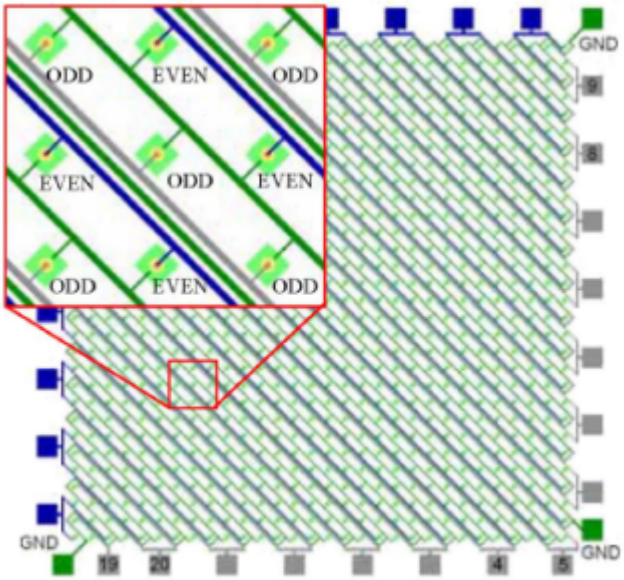

Figure 2.4: Second generation microdosimeter array consisting of 900 cylindrical diodes. Individual detectors are connected odd-even in such a way that any single odd connected detector is surrounded by 4 identical even connected detectors.

The third generation of SOI device was large area, 4 mm ×5 mm segmented microdosimeters with individual cylindrical 2D planar sensitive volumes fabricated on a 10 µm thick n-SOI, that demonstrated a 100% yield of functioning sensitive volumes [6], as shown in figure 2.5. This detector was used in various mixed radiation field environments, such as space [92, 94] avionics [95], and hadron therapy [96]. The

results showed the SOI microdosimeter closely matched the microdosimetric spectra obtained with the TEPC.

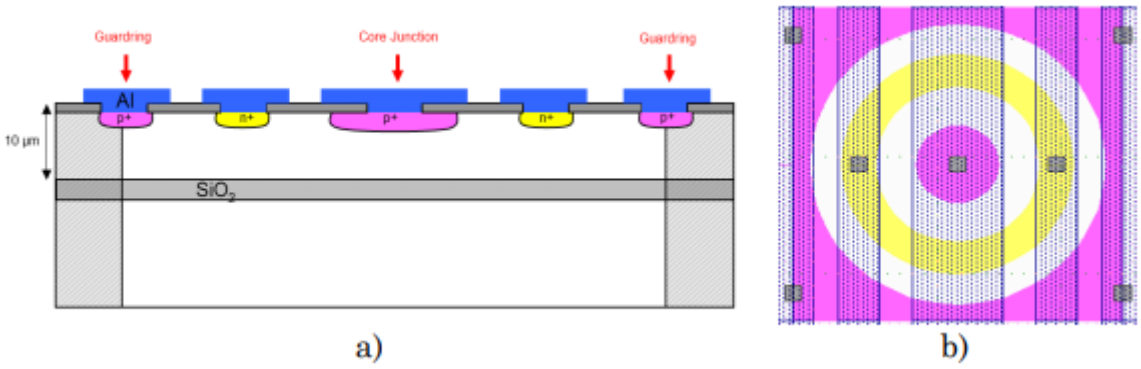

Figure 2.5: Schematic of the third generation microdosimeter (a) cross sectional side view (b) top view. Image from [6]

The fourth generation SOI microdosimeter was developed as an intermediate step toward achieving a fully 3D microdosimeter with free standing sensitive volumes. This microdosimeter has a mesa structure which was produced by using the plasma etching technology at the microelectronic fabrication facility at SPA-BIT, Kiev, Ukraine, shown in figure 2.6. The surrounding silicon was etched away, leaving a thin silicon bridge between the sensitive volumes to support the aluminium tracks. The mesa design was previously implemented in the second generation SOI microdosimeters [5], but the results showed a low yield of sensitive volumes because the aluminium tracks were damaged when suspended over the mesa structure of each sensitive volume. This new microdosimeter is called a "bridge" microdosimeter due to the thin bridges connecting the sensitive volume. Chapter 3 will present some of the characterisation of the 3D bridge microdosimeter and its use in BNCT.

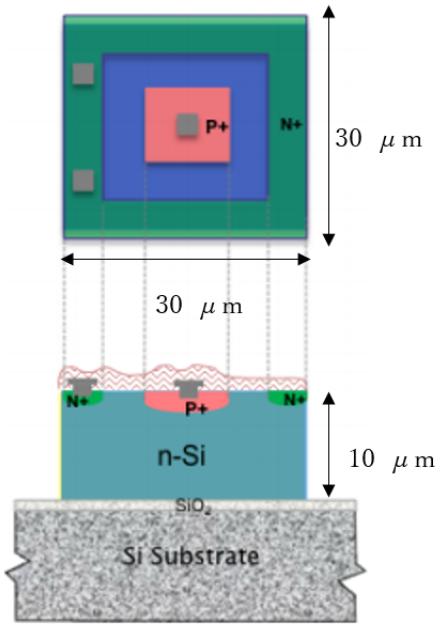

Figure 2.6: Schematic of the 3D bridge microdosimeter. Each sensitive volume is 30 μm×30 μm×10 μm (width×length×height). Image from [7].

The bridge SOI microdosimeter has shown effective for measuring microdosimetric spectrum and deriving RBE of charged particle beams, such as proton and carbon ions [97, 98]. For measurements in heavy ion therapy, where the beam is normally incident to the surface of the detector, the mean chord length of the sensitive volume is approximately equal to the thickness of the detector. However, in BNCT, the neutron field is normally incident on the surface of the detector, but the secondary charged particles (protons, alpha particles, recoil heavy ions etc.) that are generated are necessarily not. Also, the planar technology has the limitation of only being able to pattern the silicon 1 – 2 μm below the surface. With the sensitive volume thickness being 10 μm, this creates a non-uniform charge collection inside the SV [99]. To overcome these issues, the CMRP proposed to develop an optimal SOI microdosimeter called "mushroom" microdosimeter with 3D sensitive volumes embedded in PMMA using 3D active edge detector technology [100, 101], shown in figure 2.7. The sensitive volumes are cylindrically shaped to provide a well-defined sensitive volume and less variance in the chord length. An array of n+ electrodes and surrounding ring p+ electrodes are produced using deep reac-

tive ion etching (DRIE), followed by polysilicon deposition and doping. This new mushroom detector is fabricated at the SINTEF Microsystem and Nanotechnology Laboratory (MiNaLab) which is in Oslo, Norway. The key techniques for production of the mushroom detector are micro machining and 3D sensor technologies, which are available at SINTEF [102, 103, 104]. TCAD modeling and charged collection characterisation of this detector has been performed [105]. The results showed it yields almost 100% charge collection inside the sensitive volume. Chapter 6 will present some of the characterisation of the 3D mushroom microdosimeter and its use in BNCT.

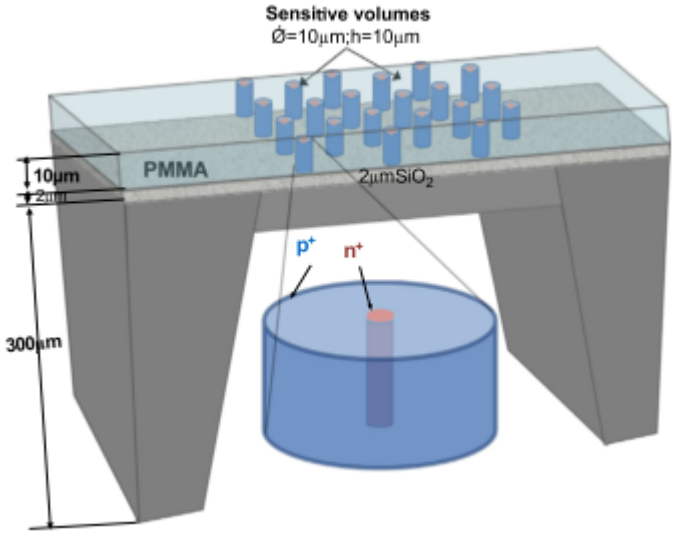

Figure 2.7: Proposed design of the 3D mushroom microdosimeter. Image from [7]

2.4 3D detector technology

In 1994, Parker and Kenney [100] proposed the combined use of Very Large Scale Integration (VLSI) and Micro-Electro-Mechanical Systems (MEMS) technologies to create new kinds of radiation detectors from high-sensitivity silicon. It consists of narrow holes and trenches that are etched through the silicon wafers then back filled with conductive polysilicon (n and p doped). This design was motivated to overcome the limitations of traditional planar silicon sensors after exposure to high fluence of non-ionising particles. The three main problems with planar sensors have been found

to be (i) higher leakage currents due to the creation of generation/recombination centres, (ii) changes in effective doping concentration, which lead to an increase of the full depletion region, and (iii) decrease of the charge collection efficiency due to carrier trapping [8]. In 3D sensors, the distance between the p+ and n+ electrodes can be significantly reduced, as indicated in figure 2.8. This reduces the depletion voltage and lowers the trapping probability of generated carriers. Also, high electric fields can be achieved at lower voltages so that the charge collection times can be much faster.

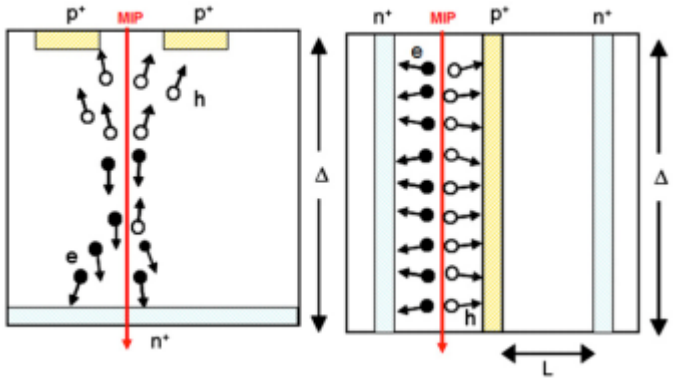

Figure 2.8: Schematic cross sections of a planar sensor (left) and 3D sensor (right) indicating the active thickness (Δ) and collection distance (L) in 3D sensors. Image from [8].

Chapter 3

Investigation of the use of tissue equivalent proportional counters for microdosimetry in BNCT

3.1 Introduction

3.1.1 Tissue equivalent proportional counters

Gas-filled ionisation detectors are radiation detection instruments used to detect the presence of ionising particles. As particles traverse through a volume of air, if it has enough energy, it will ionise the air molecule, producing electrons and ions along its track. In the presence of an electric field, these electrons and ions can be collected in the form of an electric signal. There are three main types of gas-filled ionisation detectors; ionisation chamber, proportional counter and Geiger-Muller detector. These all have the same basic design of two electrodes separated by air (or special fill gas), but each uses a different method to measure the total number of ion-pairs that are collected. Here, the proportional counter will be explained in detail. Proportional counters operate at a higher voltage than ionisation chamber, but lower than Geiger-Muller detectors (figure 3.1). The key property of the proportional counter is the ability to measure the energy of the incident radiation by producing a

detector output pulse that is proportional to the radiation energy absorbed by the detector due to an ionising event. It is widely used to accurately measure radiation beam quality, such as discrimination between alpha and beta particles. The gas fill of the chamber is an inert gas. There are many different types of gas fill available for different purposes. For this study, the purpose is to measure the dose and/or dose equivalent to small volumes of human tissue, so the chamber was filled with a tissue equivalent gas.

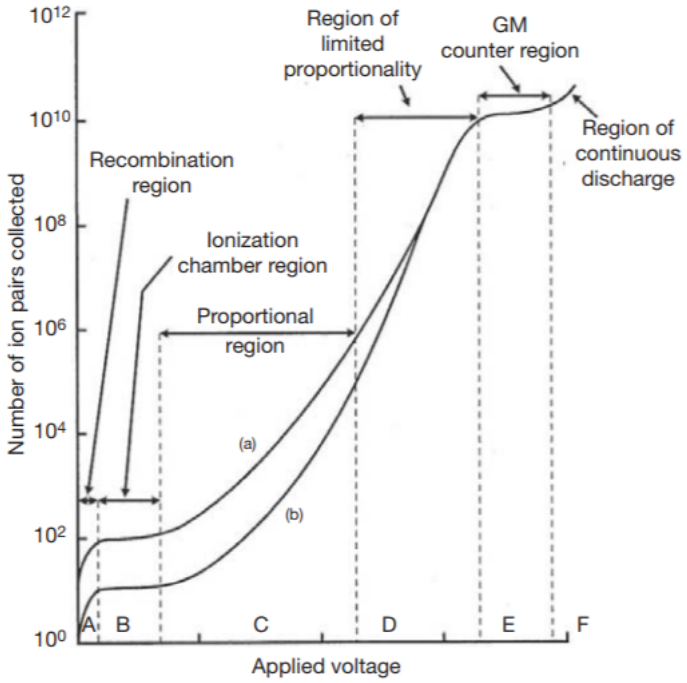

Figure 3.1: Different ionisation chamber regions as a function of applied voltage. Region A represents the recombination region, region B the ionisation region, region C the proportionality region, region D the region of limited proportionality and region E the GM. Curve (a) is for 1 MeV β particles, curve (b) for 100 keV β particles [9].

Tissue equivalent proportional counter (TEPC) plays an important role in the dosimetry of gamma rays and neutrons [106]. The chamber is constructed with the wall and fill gas mixture to mimic the elemental composition of biological tissue. As the incident neutron interacts with the chamber wall, secondary charged particles (primarily recoil protons for fast neutrons) are generated in the wall material. For walls that are thick compared to the range of the secondary charged particles,

equilibrium exists where the flux of the secondary charged particle leaving the inner surface of the wall is independent on the wall thickness. As mentioned in the previous chapter, it is important to determine the quality factor Q to convert measurements of absorbed dose into dose equivalent. The LET value determines the quality factor and the TEPC allows direct measurement of LET distribution if the gas pressure is low enough so that particles entering the gas loss a negligible amount of their energy in passing through the cavity. The pulse signal depends on the product of the LET of the particle and the path length that it travels through the gas medium. In a low-pressure gas medium, the pathlength can be approximated to be straight lines. By knowing this distribution and the measured pulse height, the LET distribution of the particle can be determined. This process is particularly useful in the analysis of neutron fluxes whose energy distribution is unknown or in mixed neutron/gamma ray fields [107]. The output pulses have to be amplified and analysed electronically. The signal is fed into a charge-sensitive preamplifier which integrates the charge on a feedback capacitor and delivers an output voltage with amplitude proportional to the charge released by the counter. The pulses from the preamplifier are amplified and shaped in a linear amplifier. This step is necessary to improve the signal-to-noise ratio of the amplifier and reduce pile-up of detector pulses. Experimental microdosimetry deals with a very large range of pulse heights so the spectrum is usually obtained using few different gain settings.

3.1.2 Neutron source

As mentioned in chapter 1, the KUR-HWNIF operates in three main modes: thermal, epithermal and mixed mode irradiation. The thermal and epithermal irradiation modes are utlised for clinical treatment of BNCT. The mixed mode irradiation (mixture of thermal and epithermal irradiation mode) is currently primarily used for research purposes, such as small animal irradiation studies. Studies of beam quality measurement using TEPC for the clinical epithermal irradiation mode has been previously carried out [108, 109]. However, beam quality measurements for

the mixed mode irradiation using the TEPC has not been carried out. Although this mode is currently not utilised clinically, it is important to determine the beam quality for accurate dose calculation during small animal irradiation experiment.

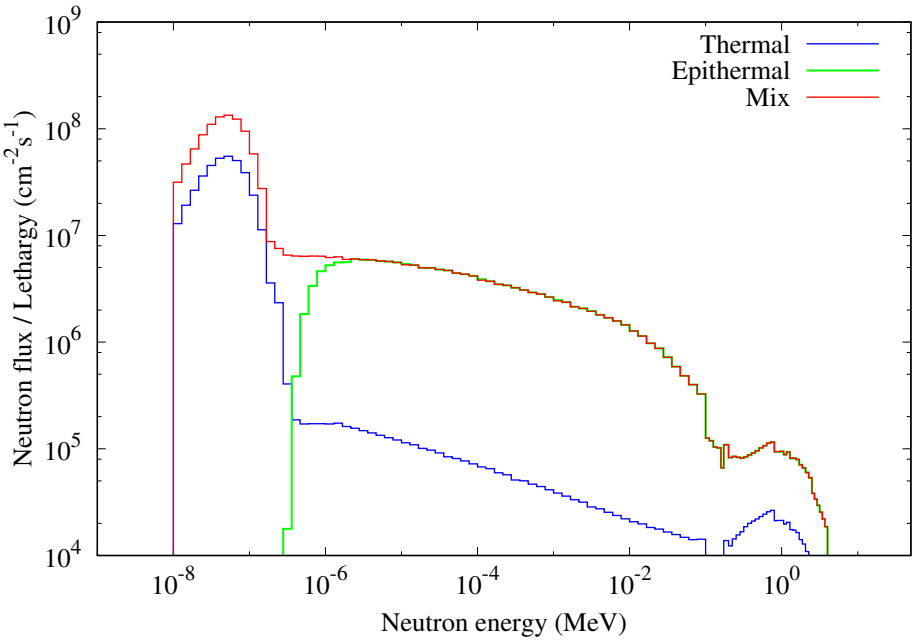

Figure 3.2: Neutron spectrum of the three main modes of Kyoto University Reactor.

The number of accelerator-based neutron sources are increasing and there are already several units being installed. Accelerator-based neutron sources utilise a high energy proton beam that strike a metallic target to generate fast neutrons. The accelerator-based neutron source located Quantum Science Center (QSC) in Aomori prefecture, Japan, has a similar design to C-BENS, which is located at Kyoto University Institute for Integrated Radiation and Nuclear Science facility. They both utilise a beryllium target, but the QSC accelerator operates at a lower proton energy of 20␣MeV. This system was modified for small animal irradiation and research purposes. The moderator system consisted of a combination of lead, graphite, heavy water and bismuth to decrease the fast neutron and gamma contamination component and increase the thermal neutron component. This chapter investigates the use of TEPC for beam quality measurement of BNCT neutron sources.

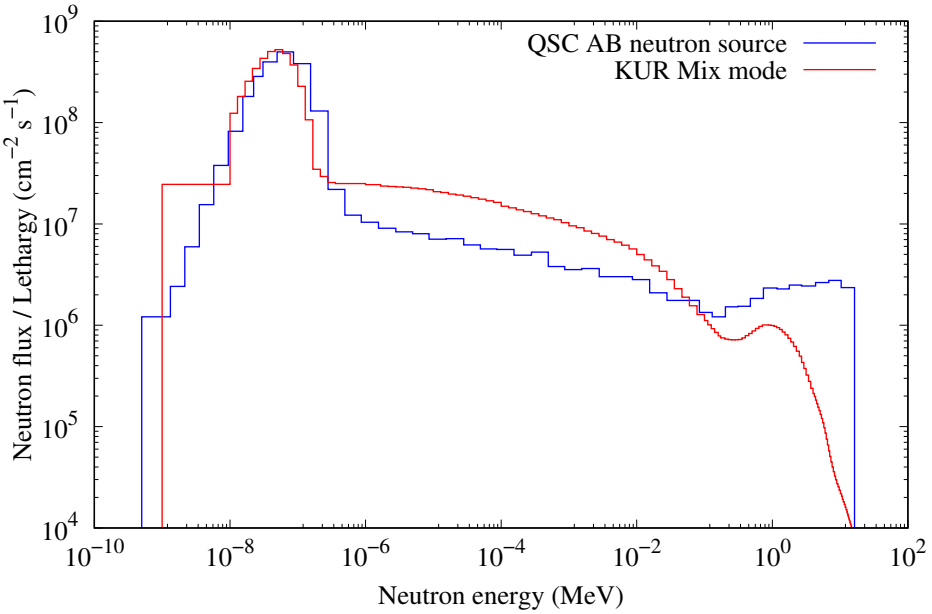

Figure 3.3: Neutron spectrum comparison of KUR mix mode (blue) and QSC accelerator (red).

3.2 Material and method

3.2.1 Calculation of microdosimetric quantities

As mentioned in chapter 1, lineal energy is a stochastic quantity and the probability density of lineal energy, *f(y)* has a probability distribution. Therefore, the expectation value of lineal energy distribution (frequency-mean lineal energy) is a non-stochastic quantity. From the single-energy deposition event distribution from the MCA counts per channel, the frequency-mean lineal energy can be rewritten as follows;

$$\bar{y_F} = \int_0^\infty y f(y) dy = \frac{1}{n} \sum_i n_i y_i \tag{3.1}$$

$$f(y) = n_i / \sum_i n_i \tag{3.2}$$

where $n_i$is the number of counts of a single energy deposition event per i$^{\text{th}}$

channel, y_i is the lineal energy per ith channel. Likewise, the dose mean lineal energy can be rewritten as follows;

$$\bar{y_D} = \frac{1}{\bar{y_F}} \int_0^\infty y^2 f(y) dy = \frac{\sum_i n_i y_i^2}{\sum_i n_i y_i} \tag{3.3}$$

The TEPC can directly measure absorbed dose since it can simulate a microscopic human tissue cavity under a Bragg-Gray cavity principle. The absorbed dose is calculated by measuring the energy imparted in a gas cavity as follows;

$$\begin{aligned} D(Gy) &= \frac{d\bar{\varepsilon}}{dm} = \frac{1.602\times10^{-13}}{m_g} \sum_i n_i \varepsilon_i \\ &= \frac{1.602\times10^{-13}}{m_g} \frac{2d_t}{3} \sum_i n_i y_i \end{aligned} \tag{3.4}$$

where 1.602×10^{-13} is a conversion constant (Gy·g/keV), m_g is the mass of the TE gas and d_t is the tissue cavity diameter (μm) simulated by the TEPC. The mean quality factor of the radiation field was calculated as follows;

$$\bar{Q} = \frac{\sum_{i=1}^n Q(y_i) y f(y_i)}{\sum_{i=1}^n y f(y_i)} \tag{3.5}$$

where $Q(y_i)$ is the radiation quality factor expressed as a function of lineal energy [110]. By knowing the mean quality factor and the absorbed dose, the dose equivalent for a single secondary charged particle that deposits its kinetic energy in a microscopic tissue volume can be calculated as follows;

$$H = \bar{Q} \times D \tag{3.6}$$

3.2.2 Proportional counter

The neutron single event spectrum was measured using the Far West Technology Inc. LET-1/2 0.5 inch proportional counter. Two types of proportional counters were used. One was a detector with a spherical cavity in a tissue equivalent plastic (Shonka type A-150) with an internal diameter of 1.27 cm. The other was a spherical cavity with the same internal diameter in a graphite wall. A bias of 500 V was

applied to the detector. The signal was fed into a low noise preamplifier. The proportional counter connector end is so called Quick-Connect, which mates with a Swagelok B-QC4-D-400 DESO-type connector. These connectors contain spring loaded plungers that seat against elastomeric O-rings providing a gas-tight seal. The proportional counter was pumped down using a rotary pump. Once the counter was under vacuum pressure, the cavity was filled with a tissue equivalent gas and pumped down to vacuum again. This procedure was repeated a few times only during the initial use to clear out any impurities inside the chamber cavity and vacuum system pipelines. Once the above procedure was carried out, the proportional counter was filled with tissue equivalent gas at a pressure of 75 hPa to simulate a cavity of 1 μm in diameter. For the graphite walled proportional counter CO_2 gas was filled to a pressure of 43.5 hPa (see appendix for calculation). The gas mixture was sealed by tightening the bellows-sealed valve and the proportional counter was removed from the connector for portable use. The disadvantage of removing the counter from the gas-flow system was the gas leak over time. The effect of gas leak on the acquired spectrum was investigated using a ^{252}Cf check source. A constant bias of 500 V was applied to the detector. The set up was kept the same and measurements were repeated over a period of several days.

Table 3.1: Gas composition ratio inside the tissue equivalent counter.

Compound	Ratio
CH_4	64.4%
CO_2	32.5%
N_2	3.1%

Table 3.2: Gas composition ratio inside the graphite walled counter.

Compound	Ratio
CO_2	100.0%

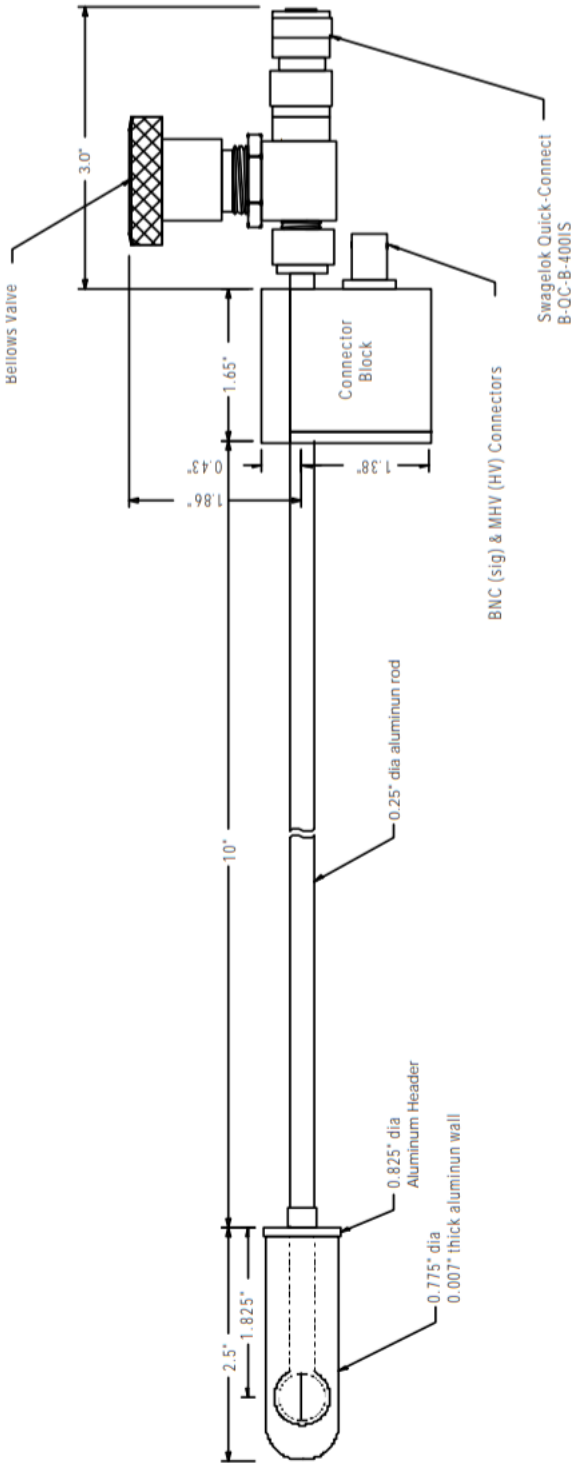

Figure 3.4: Diagram of LET-1/2 counter.

3.2.3 Calibration

The channel number was converted to energy using the spectrum obtained from the ^{252}Cf source type N-252 (figure 3.5). Two ^{252}Cf sources were used to increase the neutron flux. The source specification stated on the nominal source certificate is shown in table 3.3. Considering the radioactive decay of the source, the radiation output at the time of measurement was approximately 2×10^5 n/s.

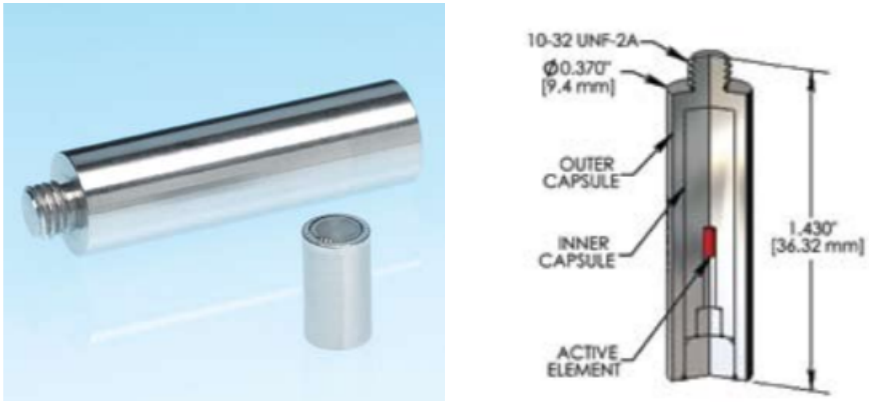

(a) (b)

Figure 3.5: a) ^{252}Cf check source. b) Cross section of the ^{252}Cf capsule [10]

Table 3.3: ^{252}Cf check source specification.

Source No.	Activity (MBq)	Radiation output (n/s)	Reference date
N2-754	3.7	3.83×10^5	15-Feb-2016
N2-755	3.7	3.873×10^5	15-Feb-2016

The microdosimetric single event spectrum of a neutron source obtained with the TEPC was broken into few components. Secondary electrons arising from gamma rays have a maximum lineal energy of approximately 20 keV/µm. Proton components have a maximum lineal energy of approximately 150 keV/µm. Heavy ion recoil components, such as carbon and oxygen, have lineal energies greater than

200 keV/μm. The spectrum has few shoulders or edges that represent each component. The electron and proton edges were used to calibrate the energy scale. To further convert the scale to lineal energy (usually expressed in keV/μm), the energy (keV) was divided by the average chord length of a 1 μm diameter sphere, 0.667 μm.

3.2.4 Experimental set up

The experiment was set up as per the diagram shown in the figure 3.6. For the methane-based tissue equivalent 1-micron diameter sphere, a voltage of 550 V yielded the best resolution. To prevent detector damage (arcing), the detector bias was set to 500V. The signal from the detector was fed into a low noise preamplifier (Ortec Model 142AH). A short length, low noise cable was used to connect the detector to the preamplifier to minimise the noise. The signal from the preamplifier was split into three linear amplifiers (Ortec 671 amplifier), each having different gain settings. A low, medium and high gain setting was set on each amplifier to measure the spectrum at high resolution over a large range. The signals from each amplifier was then fed into a multichannel analyzer system (Fast ComTec MPA-3). A pulse generator (Ortec 448 research pulser) was used to check the linearity of the analyzer.

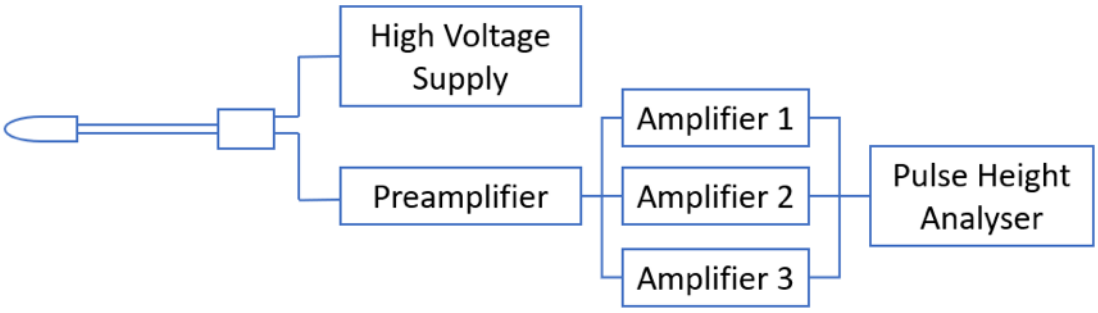

Figure 3.6: Electrical interconnection diagram for LET-1/2 operation.

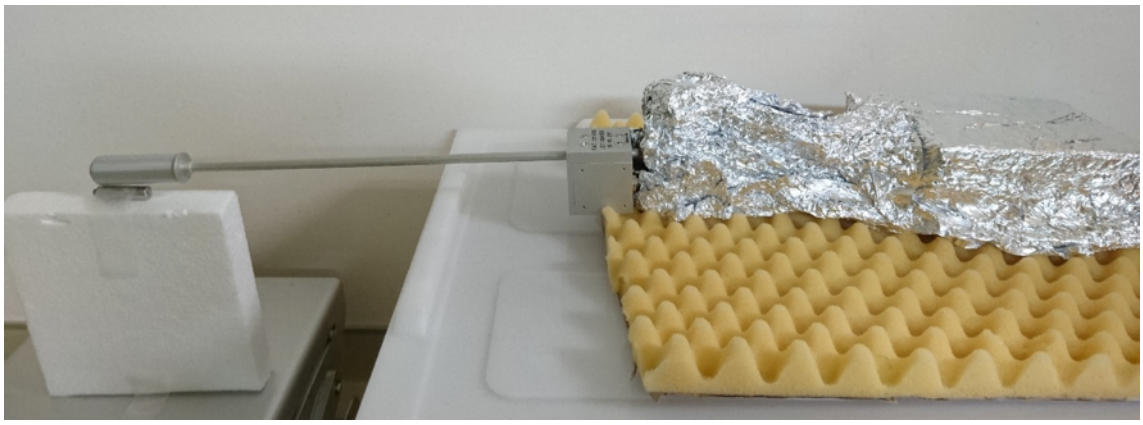

Figure 3.7: Image of the ^{252}Cf spectrum measurement using LET-1/2 detector.

3.2.4.1 Reactor system

The epithermal and mixed mode irradiation of the KUR-HWNIF was used for this study. The TEPC was placed free-in-air on top of the couch in the center of the field. A 500 V bias was applied to the TEPC and the irradiation time was set to 1 hour. The pressure inside the TEPC was set at 74.5 hPa and was filled immediately before the experiment to reduce the gas leak effect. The same measurement was performed with the graphite wall proportional counter.

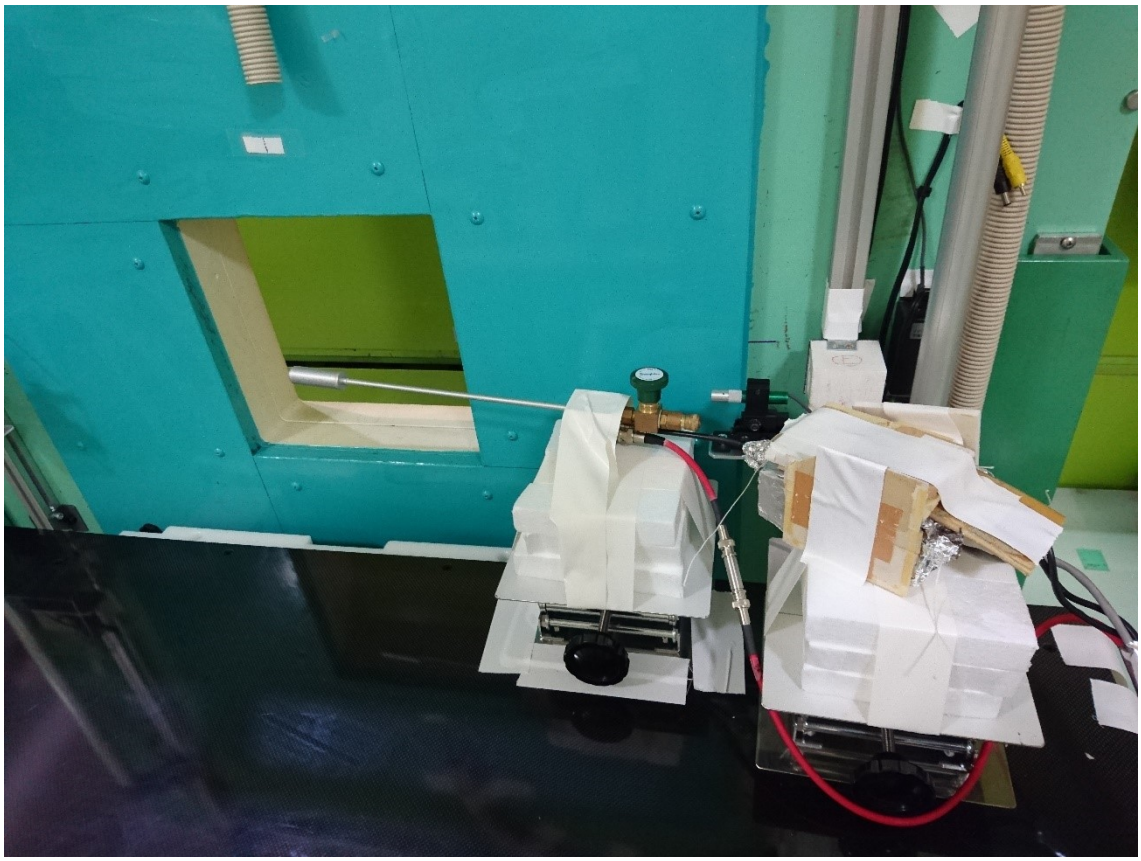

Figure 3.8: Experimental set up of in air beam quality measurement using TEPC at KUR.

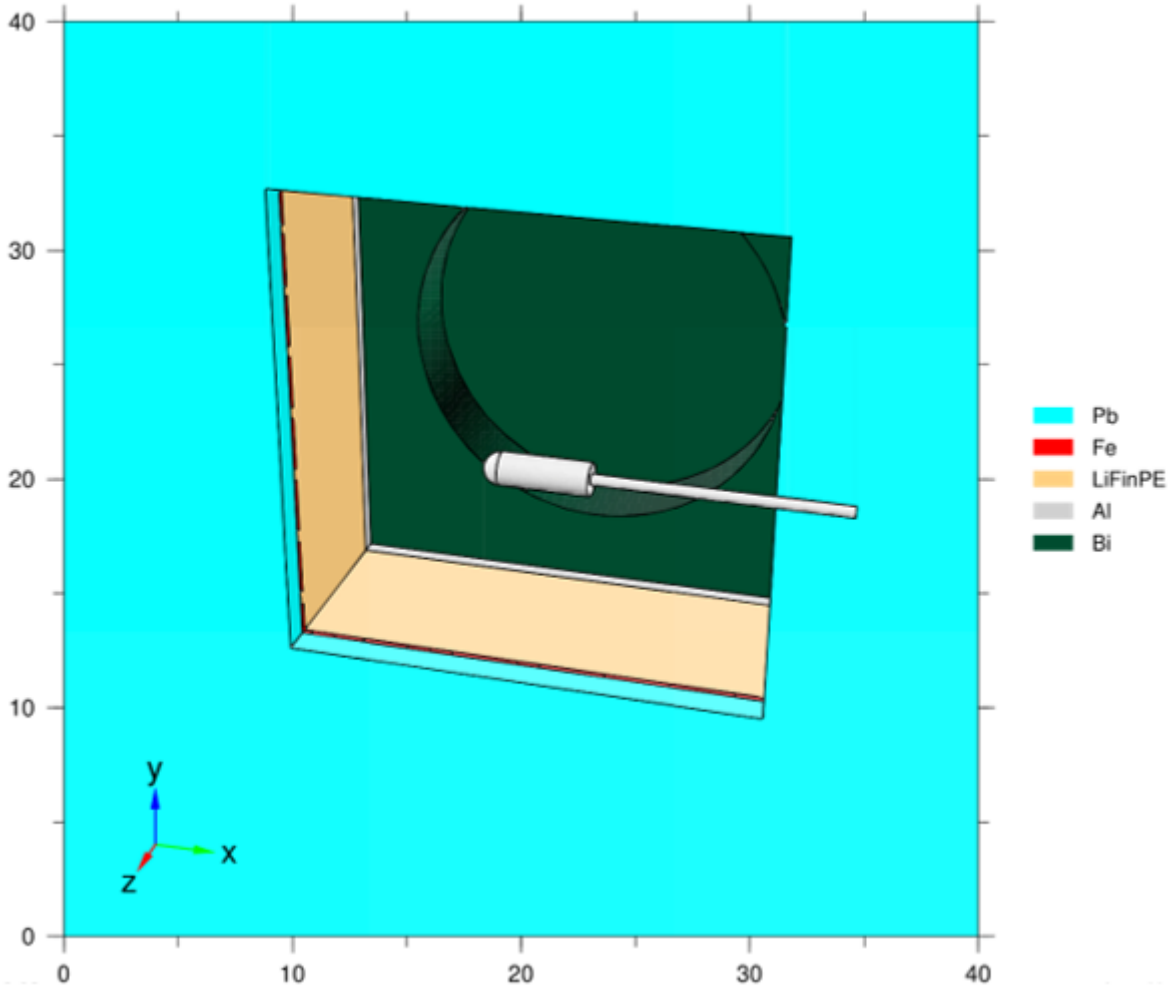

Figure 3.9: 3D geometry of the KUR experimental set up modelled in PHITS.

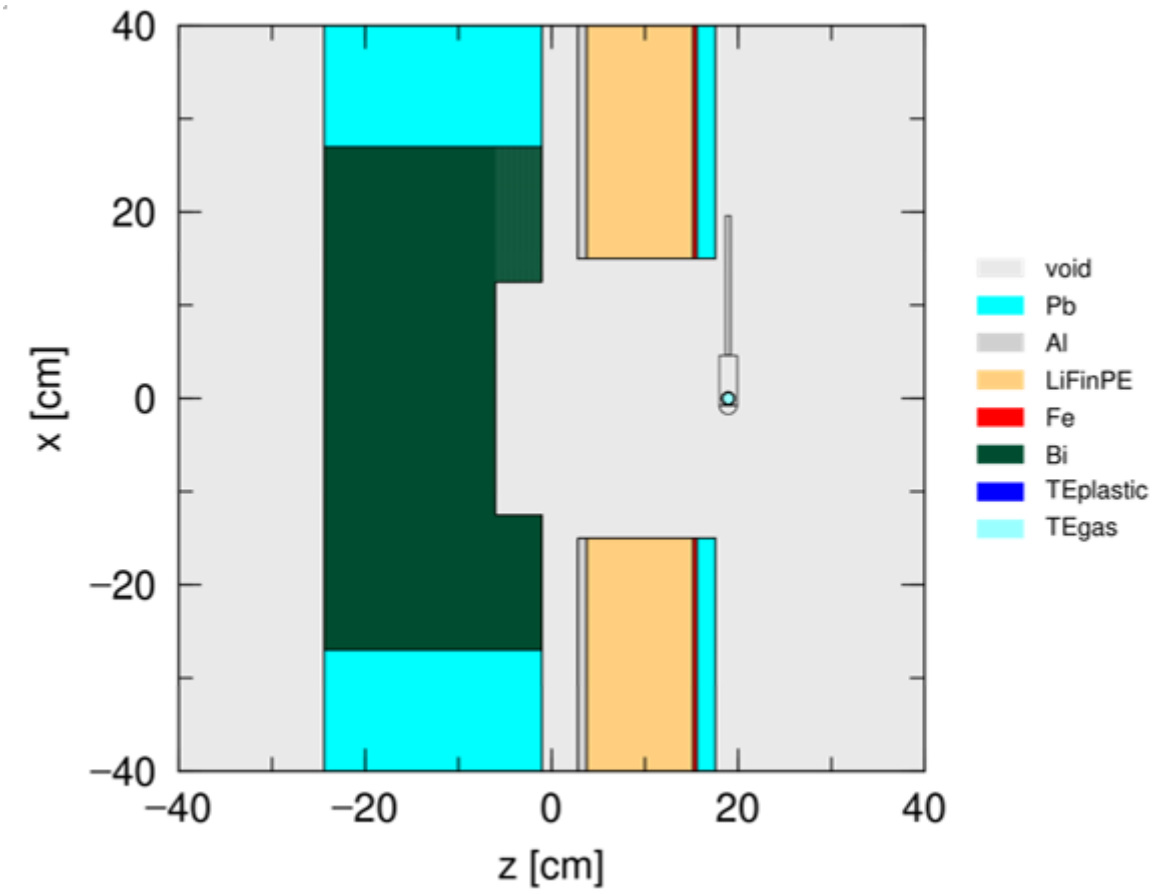

Figure 3.10: Cross sectional geometry of the KUR experimental set up indicating the different materials inside the collimator system.

3.2.4.2 Accelerator system

The accelerator-based neutron source system at QSC was used for this study. There was no gas fill system available at the facility, so the TEPC was filled with tissue equivalent gas at a pressure of 74.5 hPa at the research laboratory in Osaka prefecture. Due to logistical reasons, the irradiation was performed approximately 2 days after the gas fill. The TEPC was placed in the center of the field free-in-air. A 500 V bias was applied to the TEPC and the irradiation time was set to 1 hour.

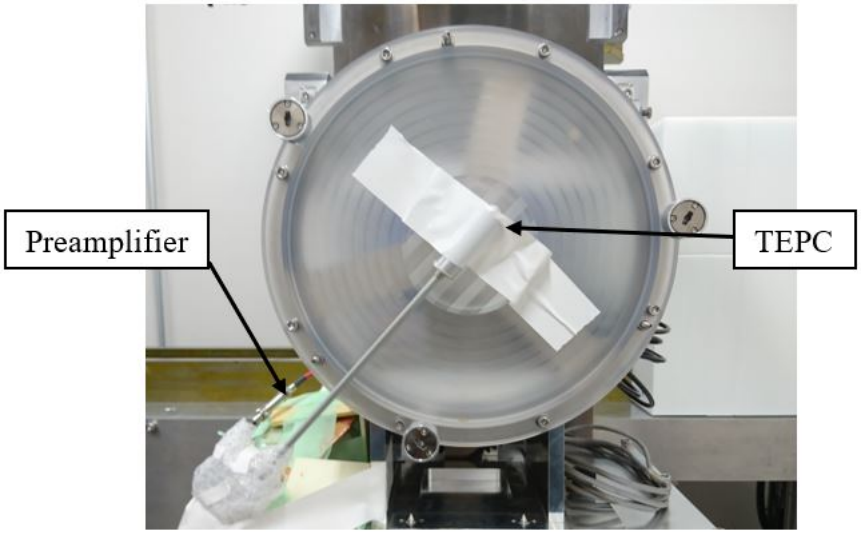

Figure 3.11: Beams eye view of in air beam quality measurement using TEPC at QSC.

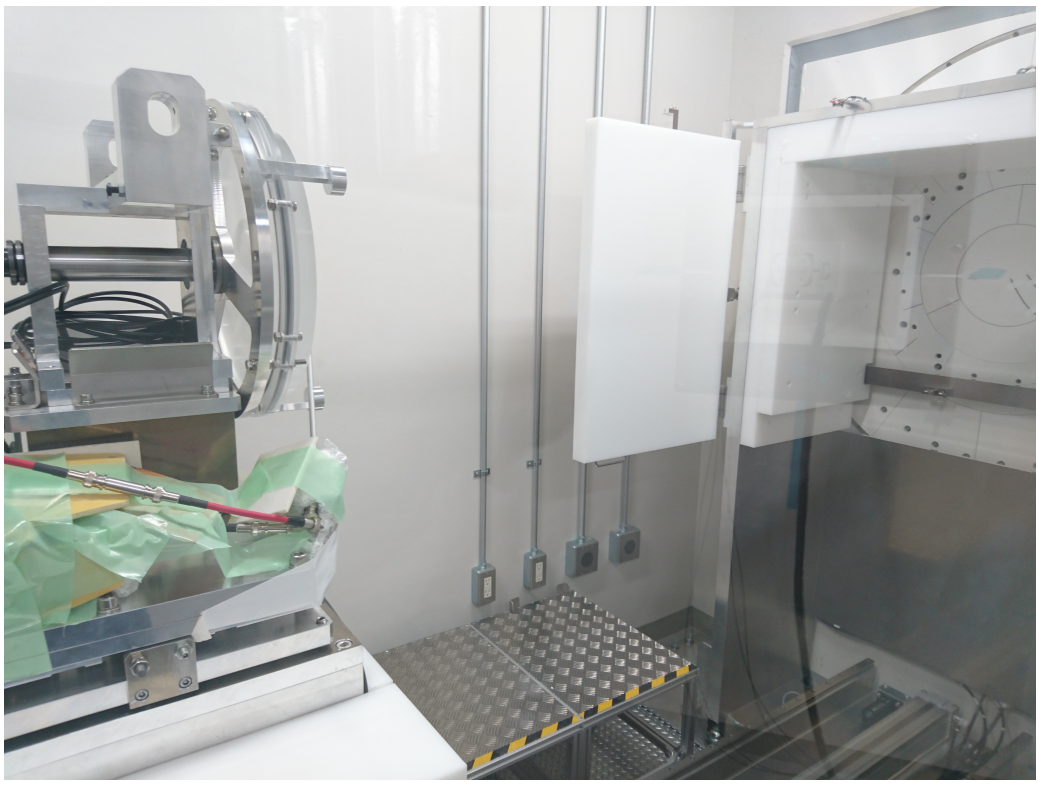

Figure 3.12: Image of the QSC irradiation room.

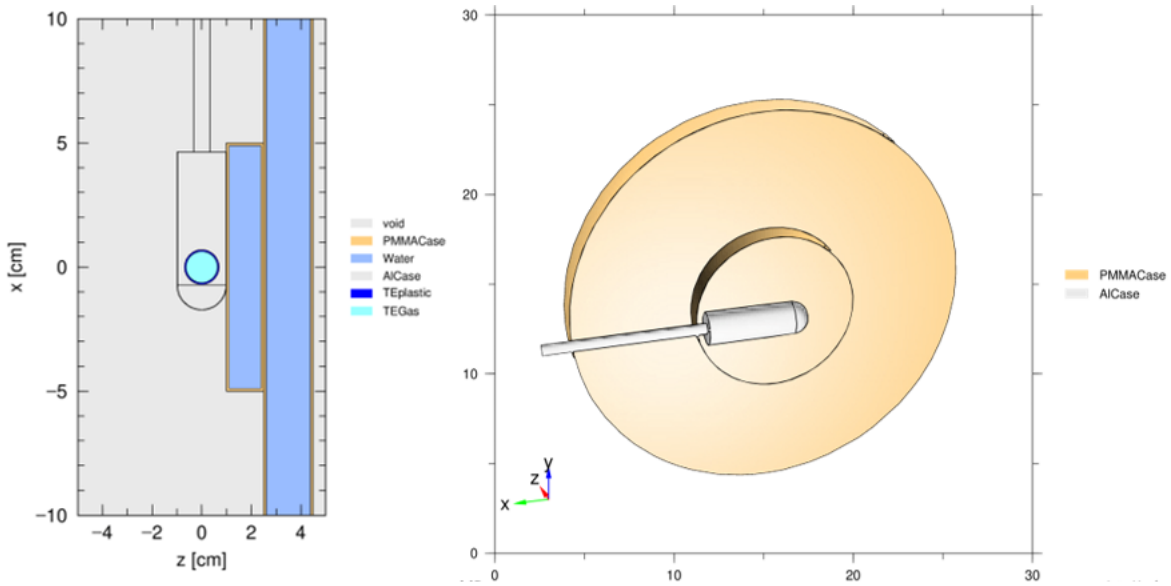

Figure 3.13: The 2D geometry (left) and 3D geometry (right) of the experimental set up modelled in PHITS.

3.2.5 Calculation of RBE

The RBE defined by the biological response to gamma rays from ^{60}Co is an important parameter to evaluate the radiation quality. The RBE was estimated from microdosimetric spectrum using a 2 Gy biological response of fractional cell survival (r(y)). This can be derived from Tilikidis et al. [111] using the following equation.

$$RBE = \int_0^\infty r(y) y f(y)\, dy \tag{3.7}$$

To compare the measured RBE to other studies, the mean energy of the neutron spectrum was calculated using the following expression from the ICRU report [112]

$$\bar{E}_\phi = \int_0^\infty E\psi_E\, dE/\psi = \int_0^\infty E^2\phi_E\, dE/\int_0^\infty E\phi_E\, dE \tag{3.8}$$

where ϕ_E is the neutron fluence at energy E.

3.2.6 Monte Carlo simulation

Monte Carlo simulation was performed using Particle and Heavy Ion Transport code System (PHITS) which is a general-purpose Monte Carlo particle transport simulation code developed under collaboration between Japan Atomic Energy Agency (JAEA), Research Organization for Information Science and Technology (RIST), High Energy Accelerator Research Organization (KEK) and several other institutes. PHITS utilises several nuclear reaction models and nuclear data libraries to simulate the transport of all particles over a wide energy range. The features of PHITS and its accuracy are reported in literature [113, 114]. The probability density of deposition energies inside a microscopic site, i.e. the lineal energy distribution, can be calculated directly in PHITS using the T-SED tally. This tally is capable of calculating the microscopic probability densities using a mathematical function that can instantaneously calculate quantities around trajectories of charged particles. PHITS version 2.88 was used for this study. The geometry of the TE and carbon walled proportional counter modelled using PHITS is shown in figure 3.10. The ^{252}Cf source was set directly above the aluminium casing in the centre of the gas cavity. The source spectrum was modelled using the watt spectrum (see appendix).

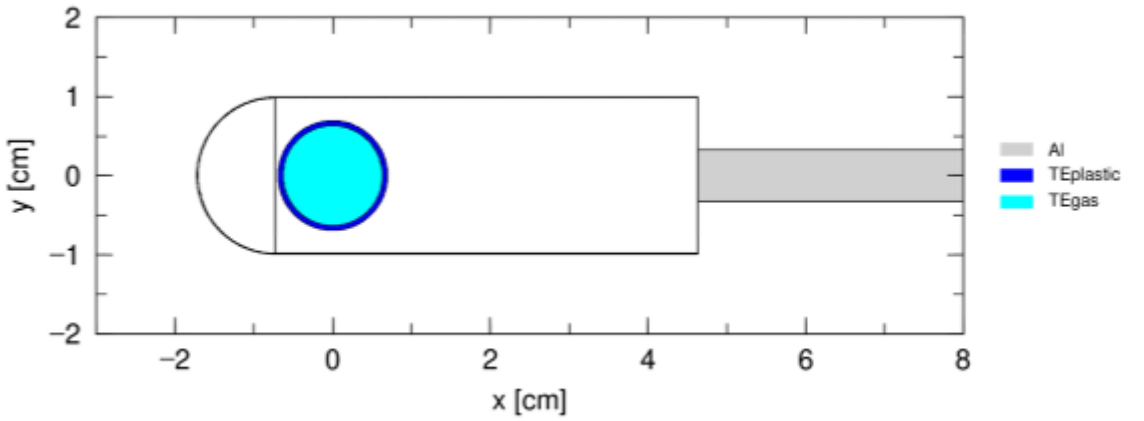

(a)

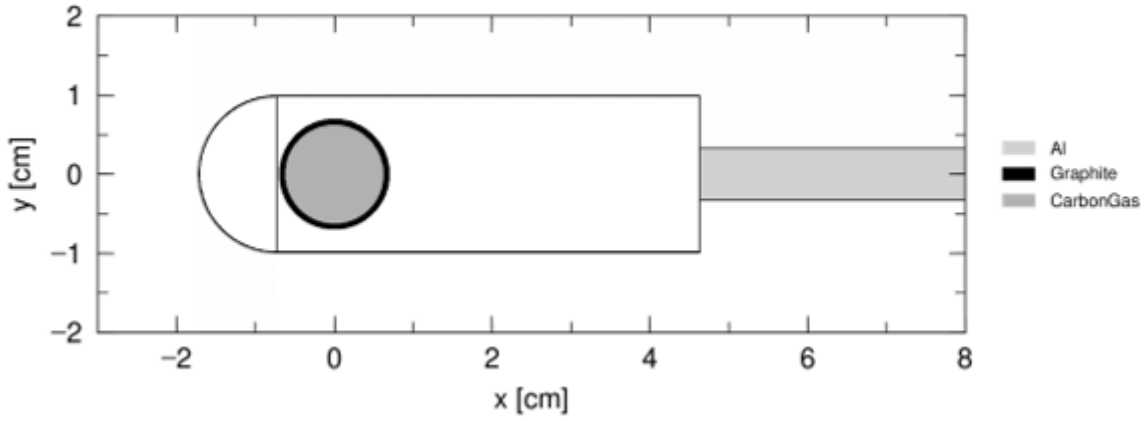

(b)

Figure 3.14: a) Cross sectional side view of the tissue equivalent A150 walled and b) graphite walled (bottom) proportional counter modelled in PHITS.

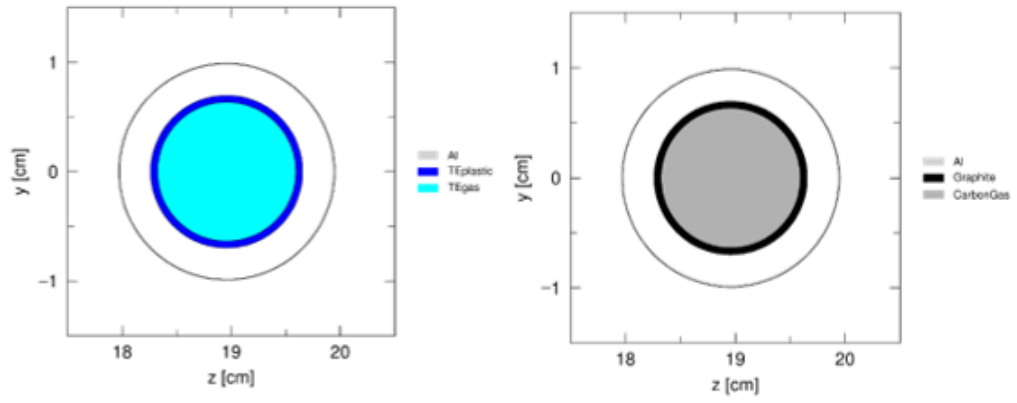

(a) (b)

Figure 3.15: a) Cross sectional front view of tissue equivalent A150 walled and b) graphite walled (right) proportional counter modelled in PHITS.

3.3 Results

3.3.1 Measurement of microdosimetric spectrum of ^{252}Cf

The shift in the measured spectrum as a function of time measured using the TEPC with a constant bias applied to the detector is shown in figure 3.16. The main cause of the spectrum shift was due to the gas leakage. The proton edge position was recorded and plotted against time progressed from the initial gas fill date. A linear fit, shown on figure 3.17, indicates the channel number drift as a function of time. According to the operations manual, the detector drift is usually less than 1 channel out of 100 in 8 hours [115]. The measurement was taken at a resolution of 1024 channels. So, the drift should be expected to be less than 10 channel numbers over a period of 8 hours. The measured channel number drift rate was approximately 1 channel per hour, which was less than the stated value in the operations manual. Hence, no significant gas leakage was detected.

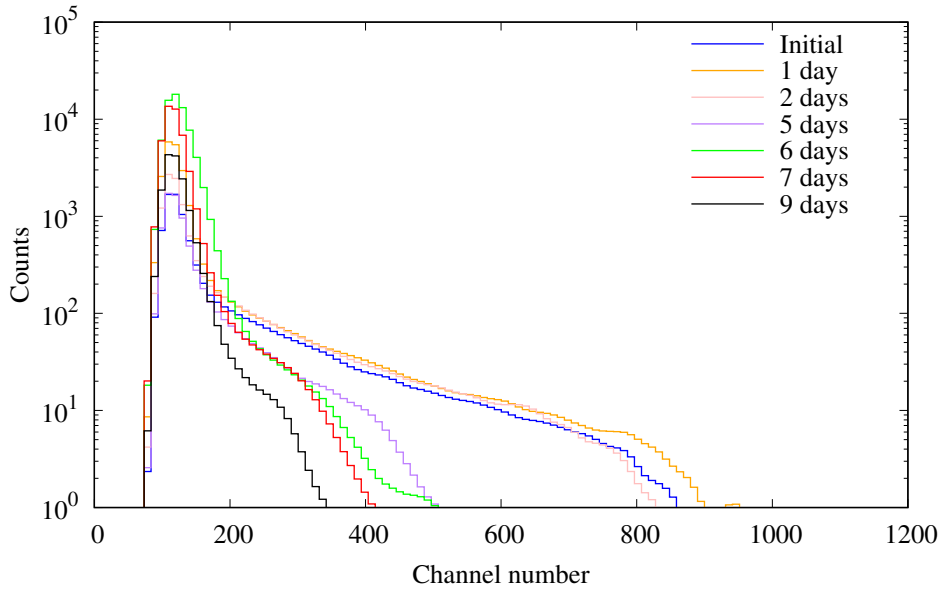

Figure 3.16: Shift in the^{252}Cf spectrum as a function of time.

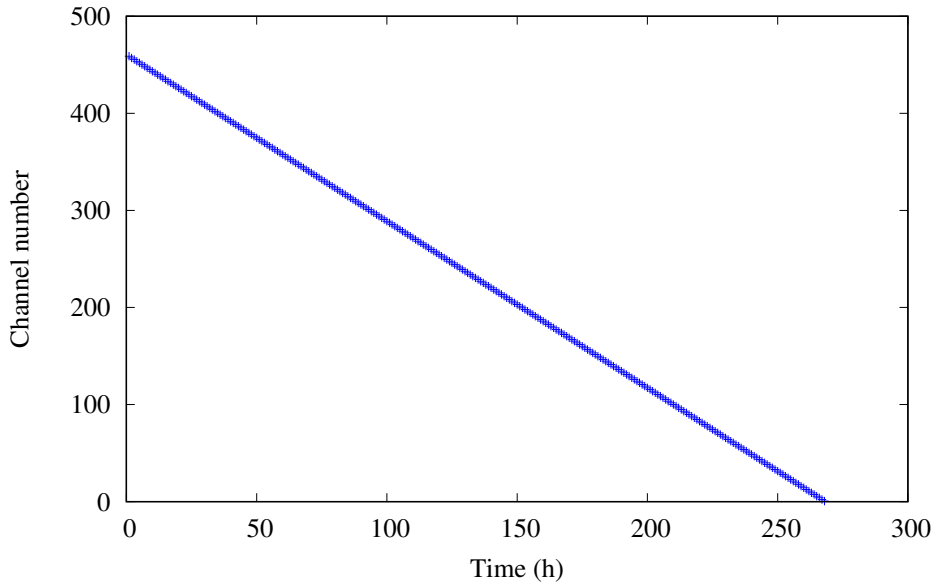

Figure 3.17: Decrease in channel number due to gas leakage as a function of time.

The ^{252}Cf spectrum measured using three different gain settings on the linear amplifier is shown in figure 3.18. The low gain setting was used to measure the high energy events and the high gain setting was used to measure the low energy events. The three measurements were combined to obtain a high-resolution spectrum across the entire range, as shown in figure 3.19. The proton edge at 150 keV/μm was clearly visible. Above 150 keV/μm high LET components such as recoil carbon and oxygen ions were present. The electron edge from the gamma rays were difficult to distinguish, due to the high electronic noise in the system. The dose distribution spectrum, shown in figure 3.20, indicates a large proportion of the dose was from the proton component. The particle track shown in figure 3.21 shows the flux of each particle in trajectory when the TEPC was irradiated with the ^{252}Cf source. The proton component was the largest, with carbon and oxygen ions following.

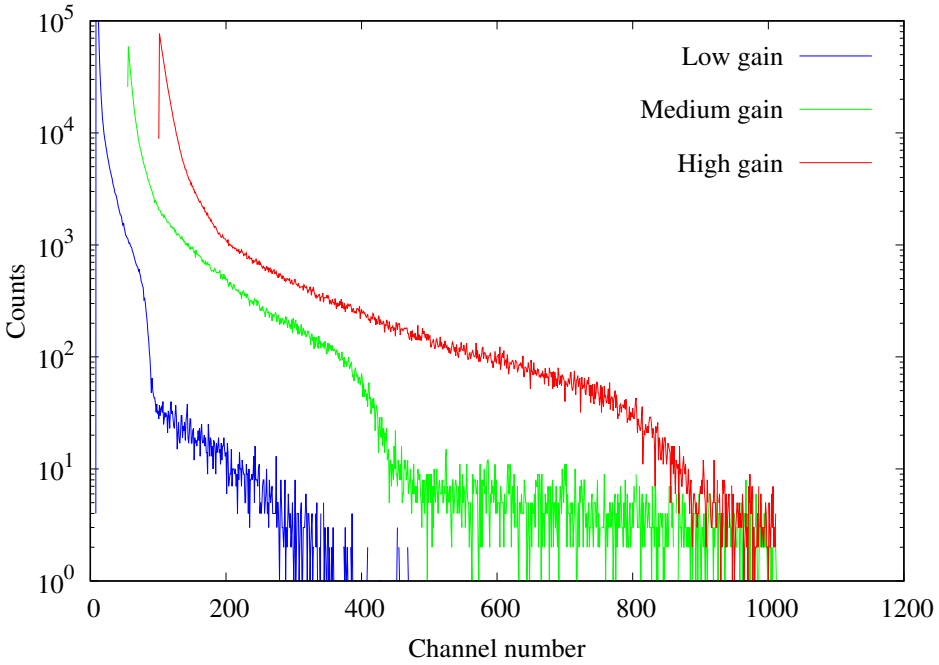

Figure 3.18: ^{252}Cf spectrum obtained using three different gain settings.

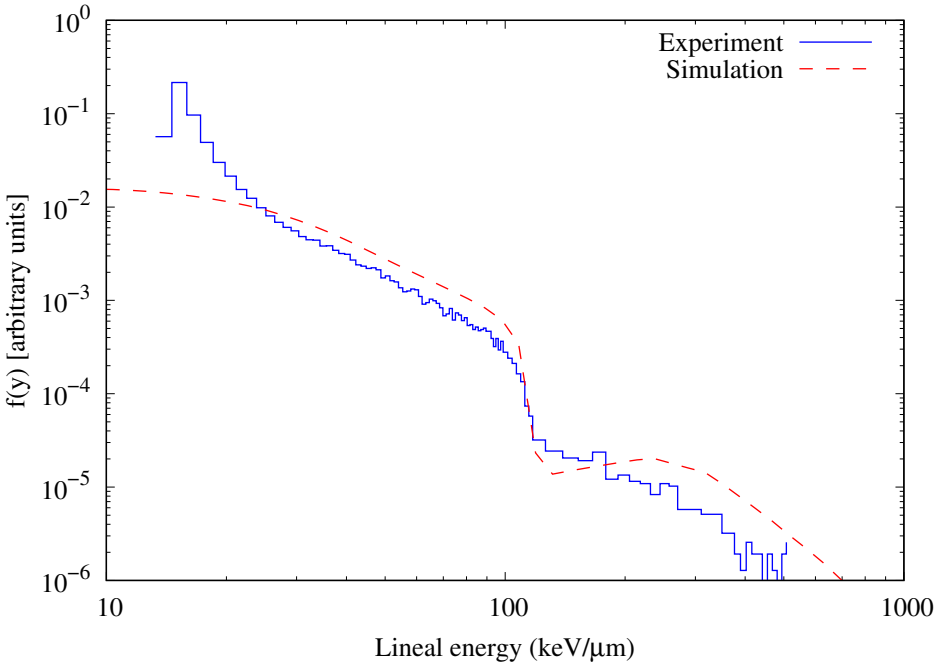

Figure 3.19: Frequency distribution curve of ^{252}Cf obtained from using the TEPC.

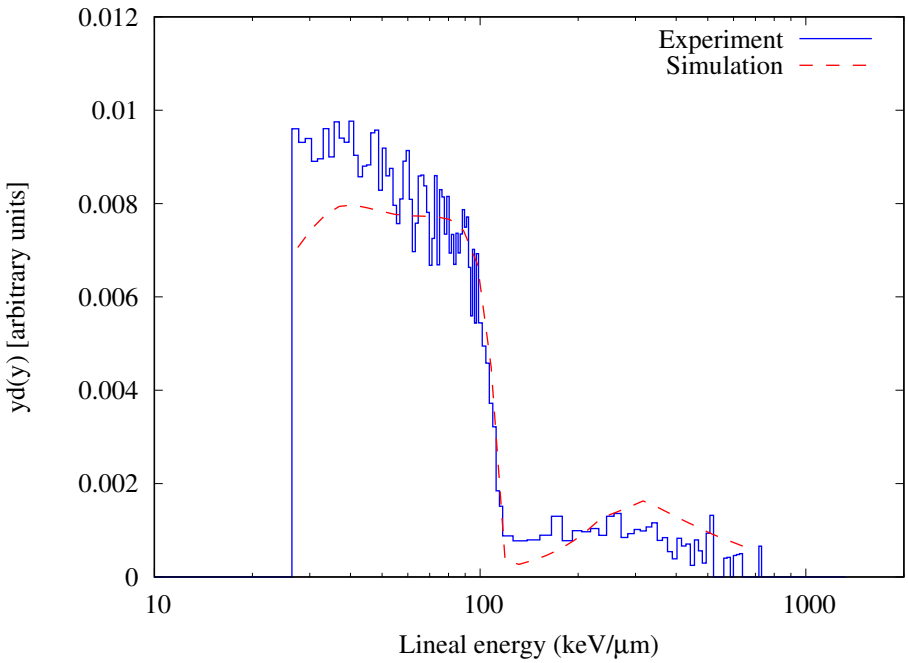

Figure 3.20: Dose distribution curve of ^{252}Cf obtained from using the TEPC.

The frequency and dose distribution microdosimetric spectrum are shown in figure 3.22 and figure 3.24. In comparison to the TEPC, the graphite walled counter does not contain any hydrogen or nitrogen components. Therefore, the proton edge around 150 keV/µm does not exist and theoretically only secondary electrons, carbon and oxygen ions should be detected. Only gamma ray components ($<$ 20 keV/µm) were detected. The recoil carbon ions were not detected. A longer measurement time would be required to detect these events.

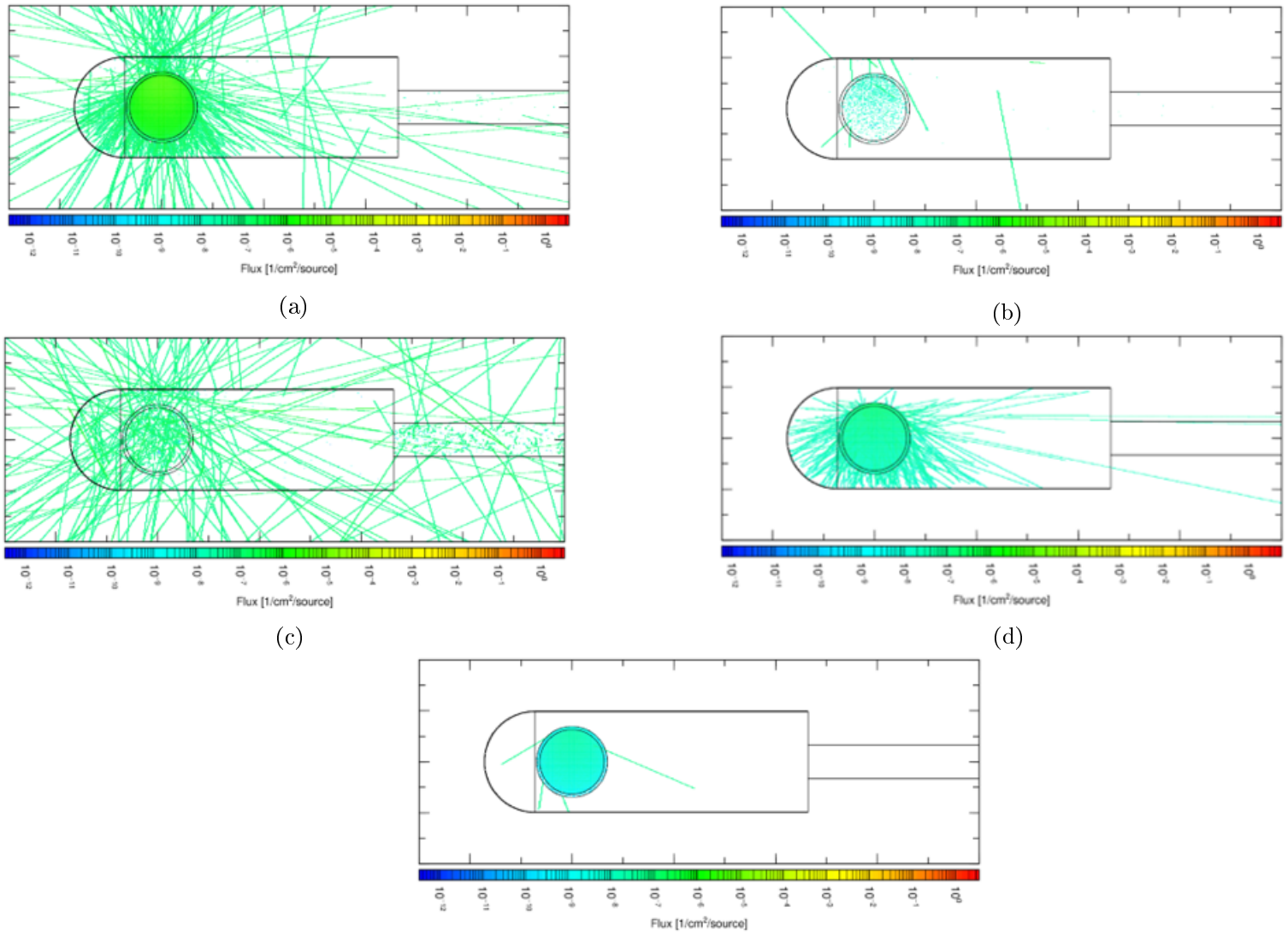

Figure 3.21: The particle track of a) protons, b) alpha particles, c) electrons, d) carbon ions, and e) oxygen ions calculated using PHITS for TEPC.

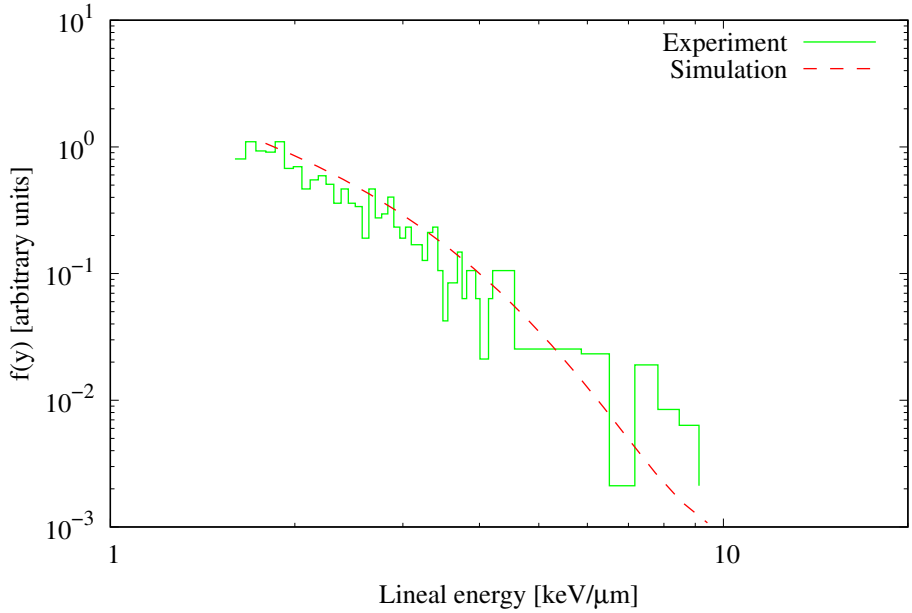

Figure 3.22: Frequency distribution curve of ^{252}Cf obtained using the graphite walled counter.

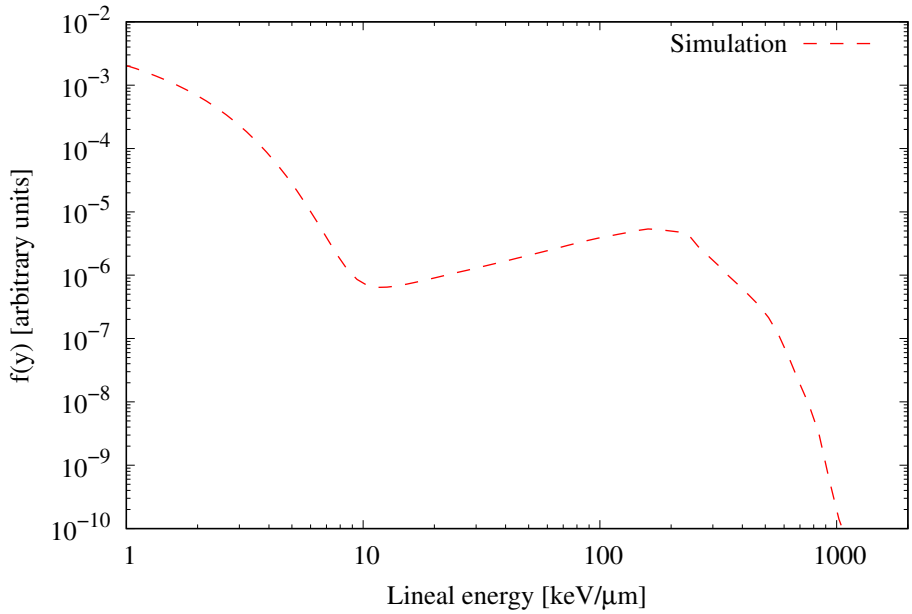

Figure 3.23: Frequency distribution curve of ^{252}Cf obtained using the graphite walled counter simulated using PHITS.

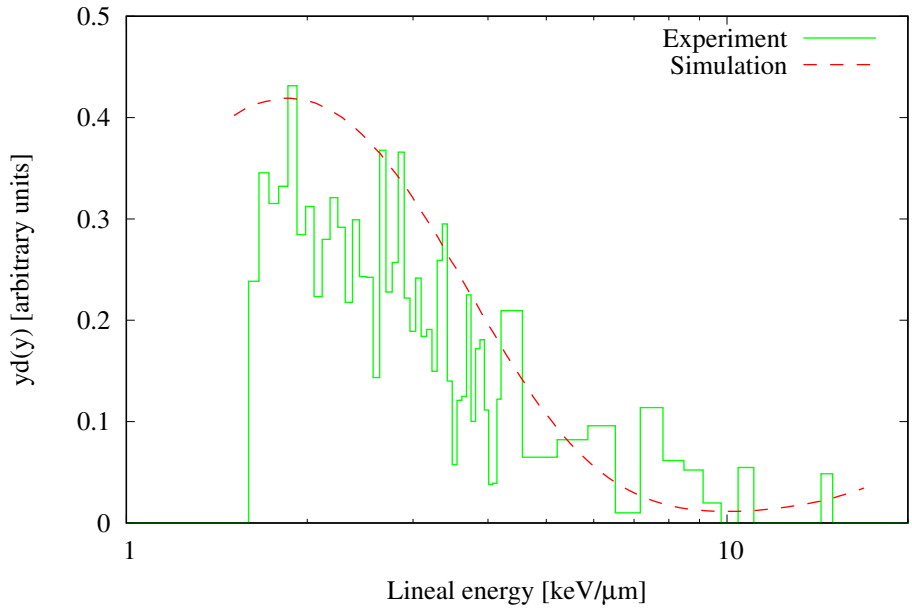

Figure 3.24: Dose distribution curve of ^{252}Cf obtained using the graphite walled counter.

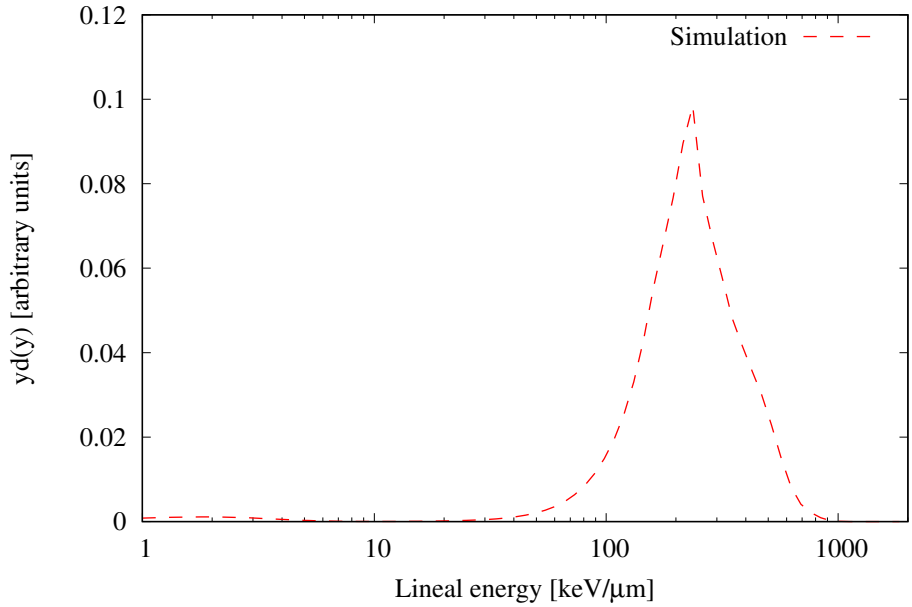

Figure 3.25: Dose distribution curve of ^{252}Cf obtained using the graphite walled counter simulated using PHITS.

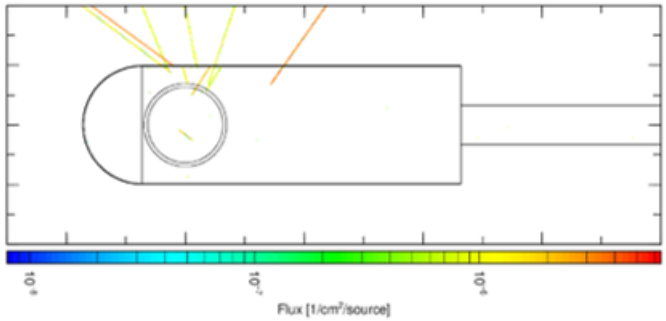

(a)

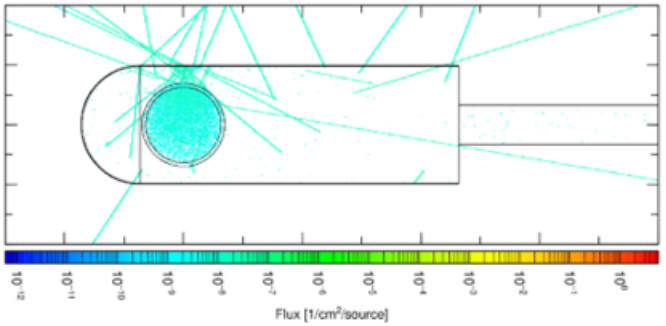

(b)

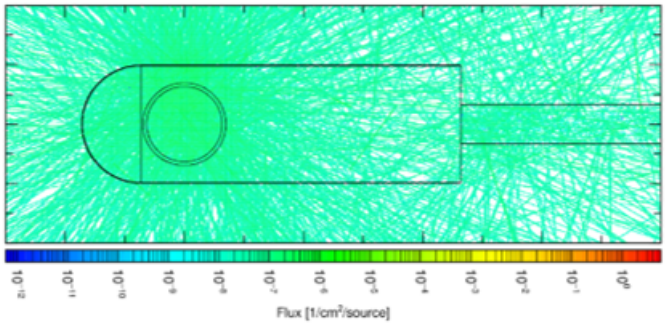

(c)

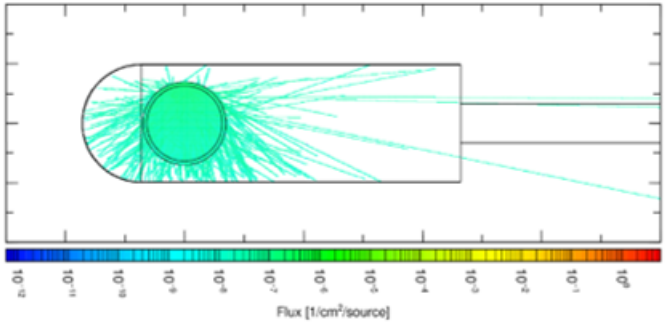

(d)

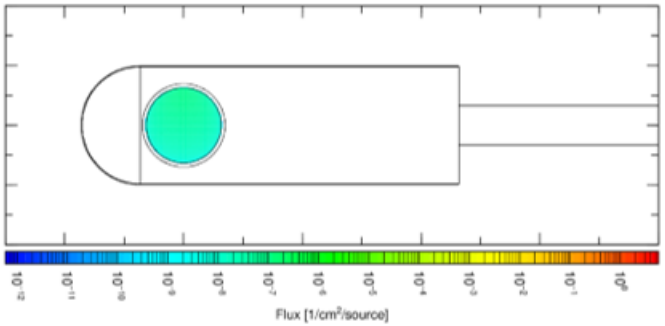

(e)

Figure 3.26: The particle track of a) protons, b) alpha particles, c) electrons, d) carbon ions, and e) oxygen ions calculated using PHITS for graphite walled counter.

3.3.2 Measurement of microdosimetric spectrum of KUR epithermal mode

The raw spectrum obtained using the medium gain setting is shown in figure 3.27. At the low channel number end of the spectrum (indicated in red), a small peak between 100 – 200 channel number was observed. These were not true events, instead were low static noise which were intermittently observed. Unfortunately, due to limited machine access, the measurement could not be repeated. So, this low static noise region was filtered out and the data points were interpolated to fit a smooth curve, as shown in figure 3.28. The frequency distribution and dose distribution microdosimetric spectrum (figure 3.29 and figure 3.30) show a nice agreement with PHITS calculated values. The major dose contributor was found to be the proton component (20 – 150 keV/μm). The frequency distribution and dose distribution spectrum obtained using the graphite wall counter is shown in figure 3.31 and figure 3.33.The measured data was noisy due to low statistics. No events were observed greater than approximately 20 keV/μm. The PHITS Monte Carlo calculation showed some high LET components, primarily recoil carbon ions, however, a longer measurement time will be necessary to observe these events.

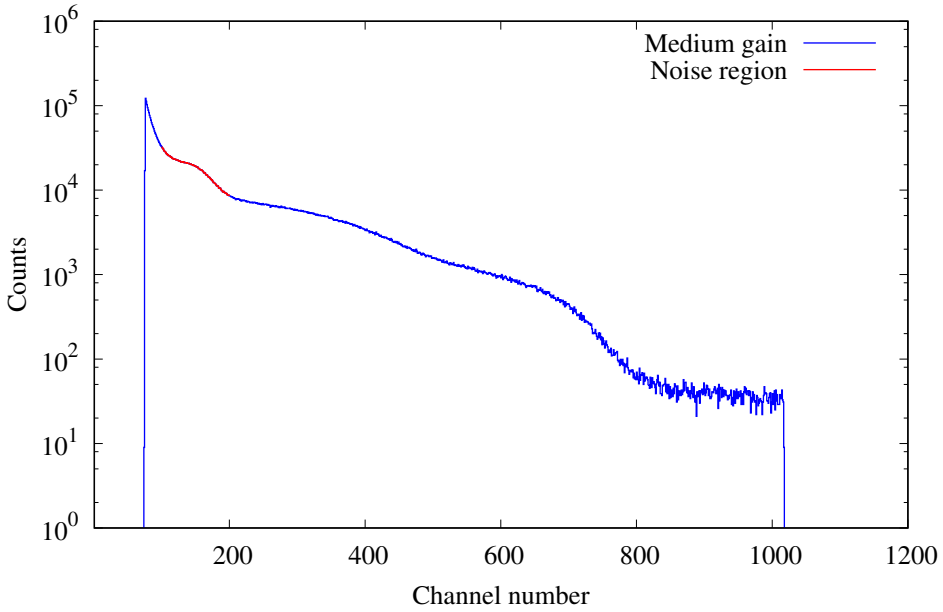

Figure 3.27: Raw spectrum of the epithermal neutron beam at KUR obtained with the TEPC. The red region indicates some static noise present in the electronic circuit.

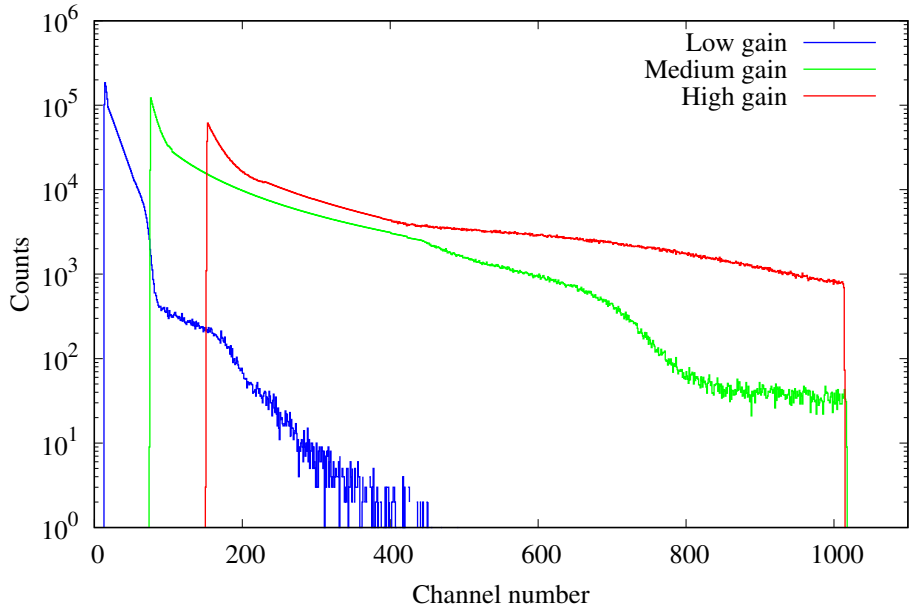

Figure 3.28: Raw spectrum of KUR epithermal irradiation mode measured using the TEPC obtained at three different gain settings.gain settings after removal of low static noise.

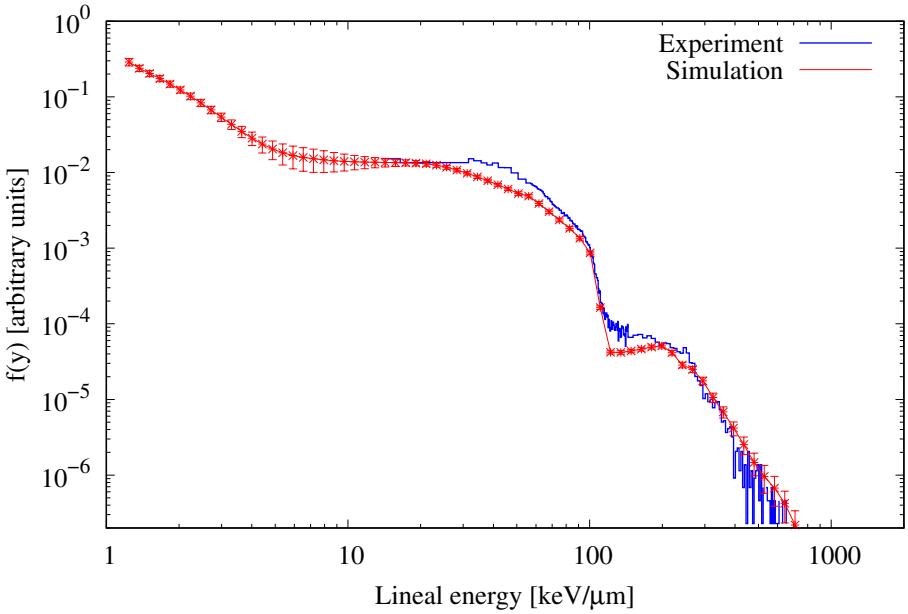

Figure 3.29: Frequency distribution of KUR epithermal mode measured using the TEPC compared against PHITS calculation.

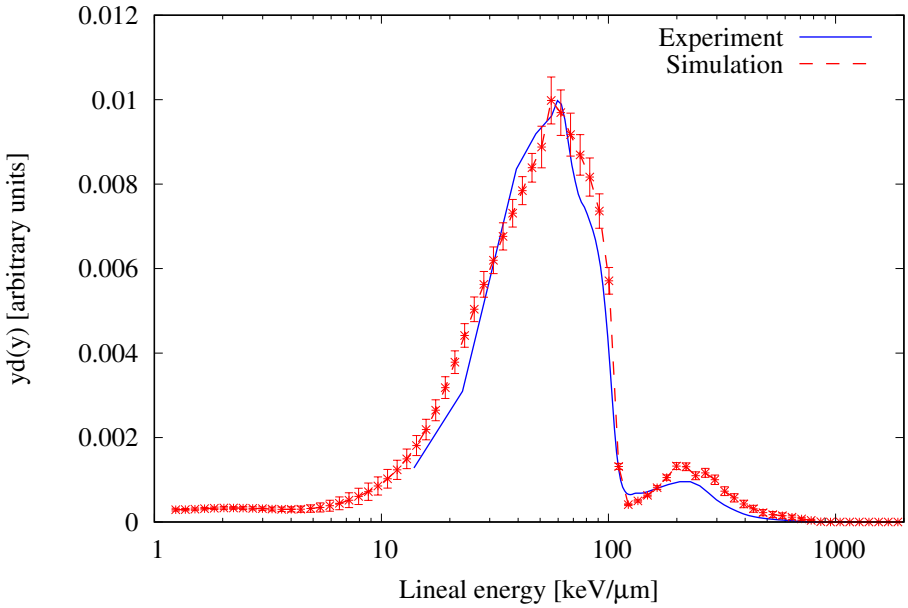

Figure 3.30: Dose distribution curve of KUR epithermal mode measured using the TEPC compared against PHITS calculation.

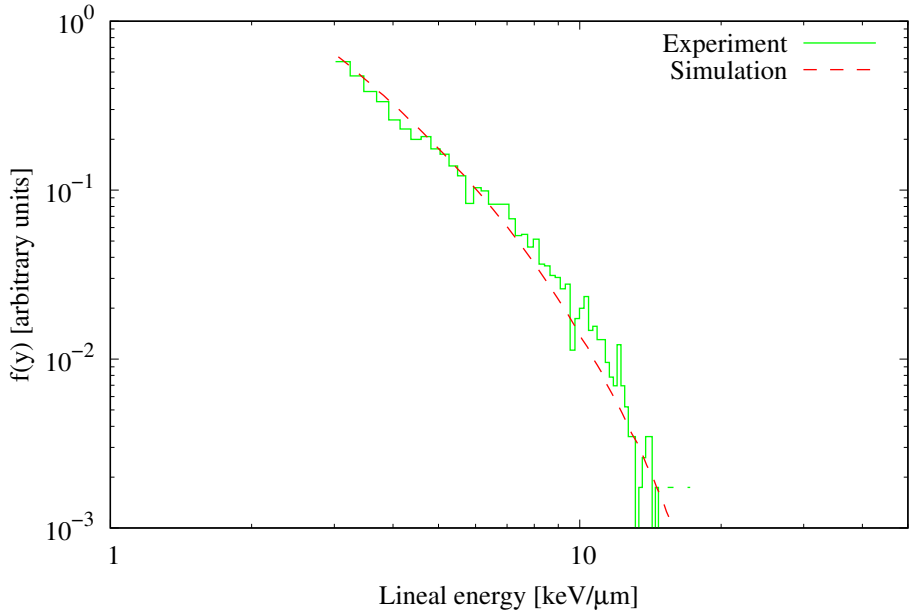

Figure 3.31: Frequency distribution curve of KUR epithermal mode measured using the graphite wall counter compared against PHITS calculation.

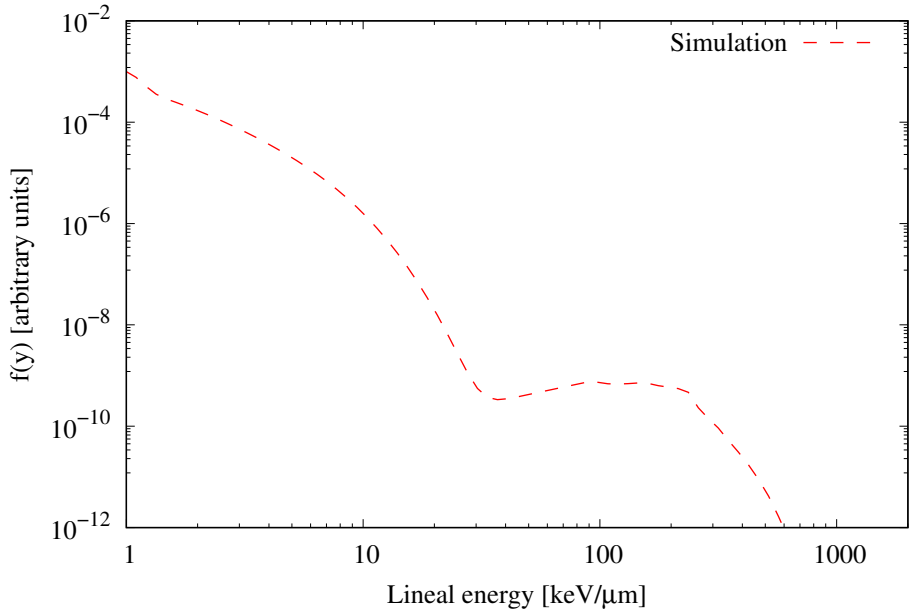

Figure 3.32: Frequency distribution curve of KUR epithermal mode obtained using the graphite walled counter simulated using PHITS.

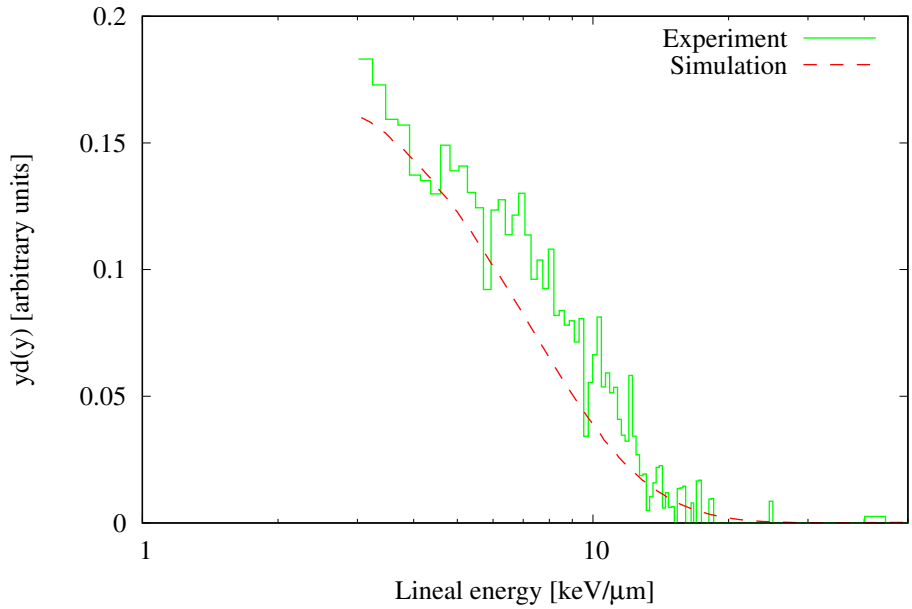

Figure 3.33: Dose distribution curve of KUR epithermal mode measured using the graphite walled counter.

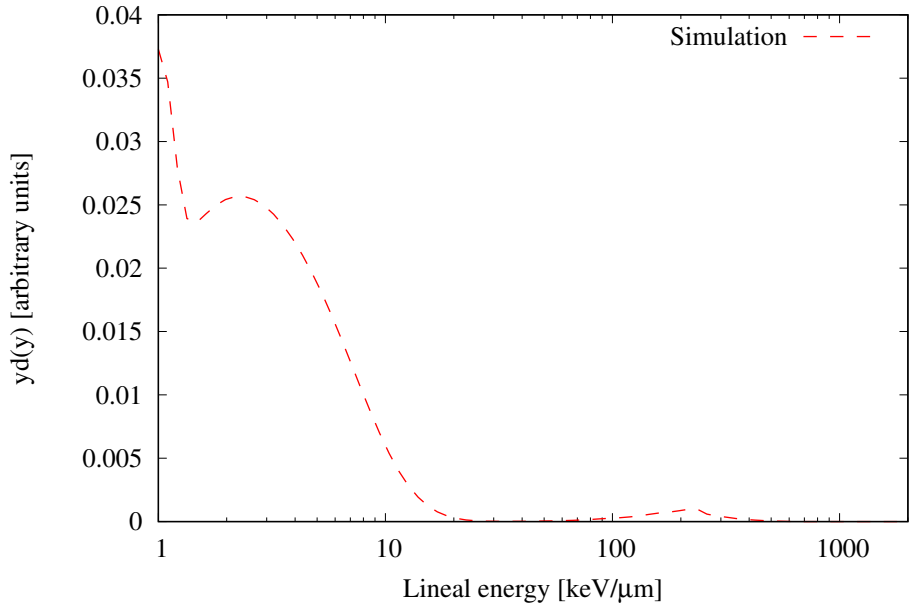

Figure 3.34: Dose distribution curve of KUR epithermal mode obtained using the graphite walled counter simulated using PHITS.

3.3.3 Measurement of microdosimetric spectrum of KUR mixed mode

The raw spectrum measured with the TEPC is shown on figure 3.35. The events detected with the high gain setting were mostly gamma ray events, events from the medium gain setting were mainly proton events and the events using the low gain setting were mostly events from high LET particles. The three spectrum were combined, and the channel number was converted to lineal energy. The microdosimetric spectrum of KUR mix mode irradiation is shown in figure 3.36 and figure 3.37. The dose distribution curve of KUR mix mode indicated the majority of the dose component was between 20 – 150 keV/μm, which represented the proton component. The PHITS Monte Carlo simulation showed a nice agreement below 150 keV/μm. Above 150 keV/μm, there was a slight discrepancy, but was within calculation uncertainty.

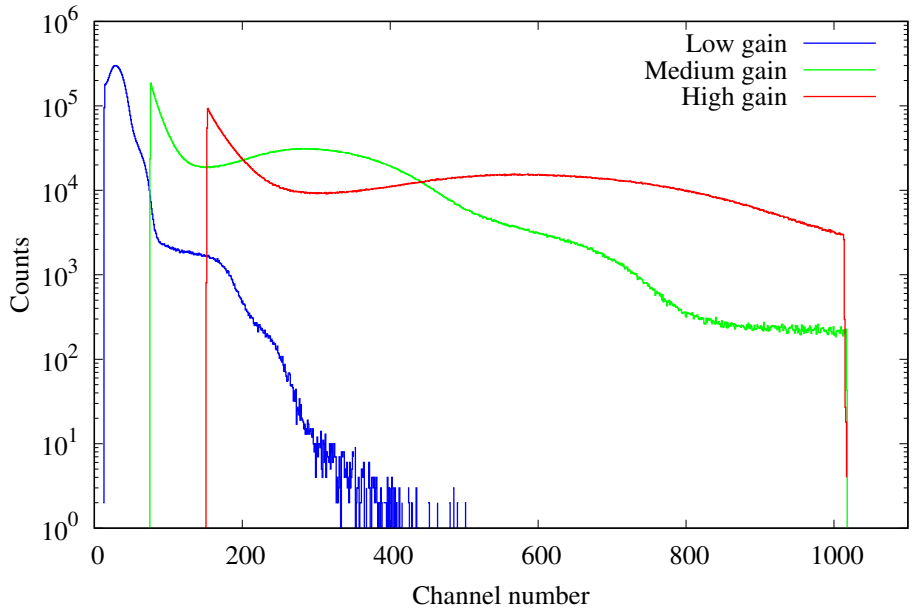

Figure 3.35: Raw spectrum of KUR mix mode measured using TEPC obtained at three different gain settings.

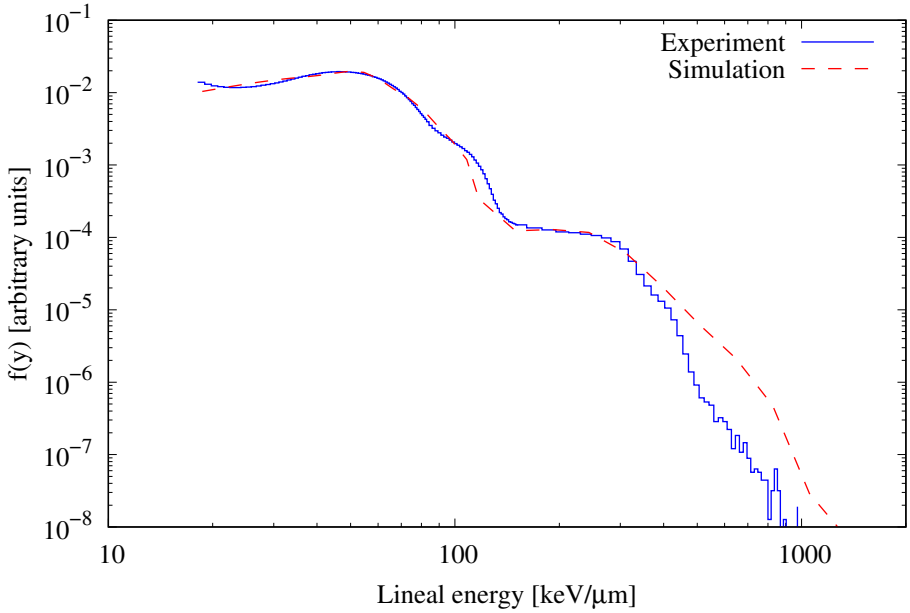

Figure 3.36: Frequency distribution curve of KUR mix mode measured using TEPC compared against PHITS simulation.

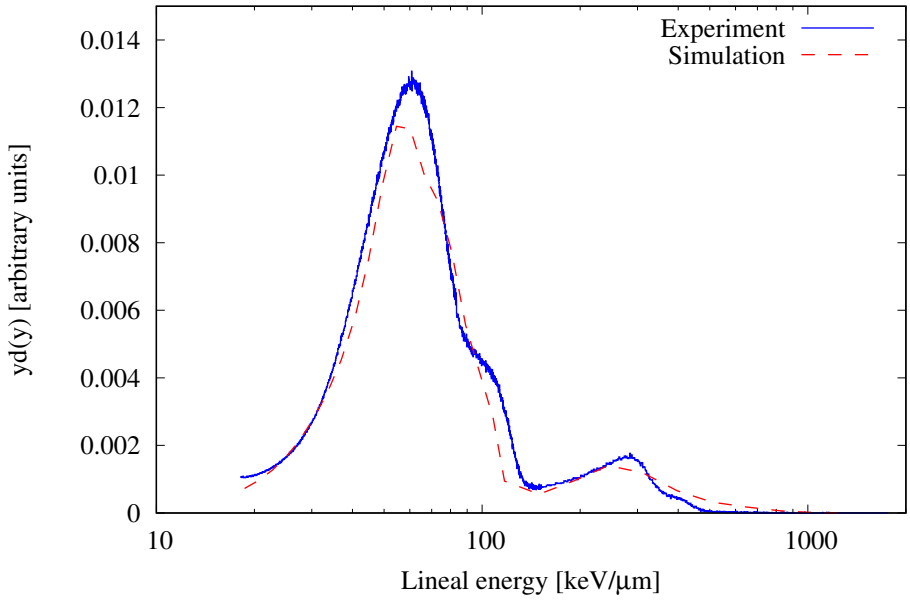

Figure 3.37: Dose distribution curve of KUR mix mode measured using TEPC compared against PHITS simulation.

The frequency distribution and the dose distribution spectrum of the KUR mix mode irradiation measured with the graphite walled counter is shown in figure 3.38 and figure 3.40, respectively. Similar to the epithermal result, only events up to

20 keV/μm were measured, which indicates the gamma component. The KUR mix mode has a larger gamma ray component compared to the epithermal mode, so more events were observed with mix mode and the electron edge was visible.

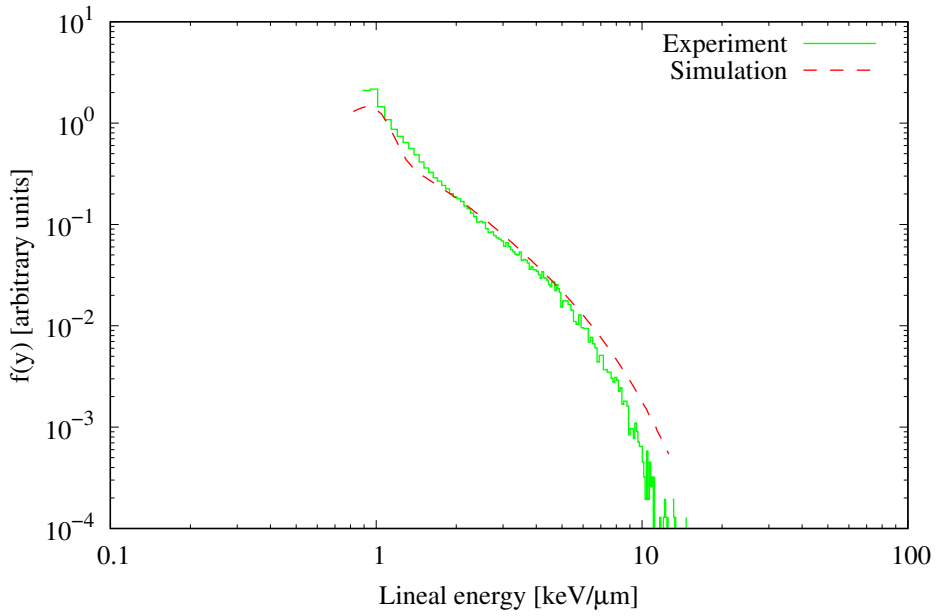

Figure 3.38: Frequency distribution curve of KUR mix mode measured using a graphite walled counter.

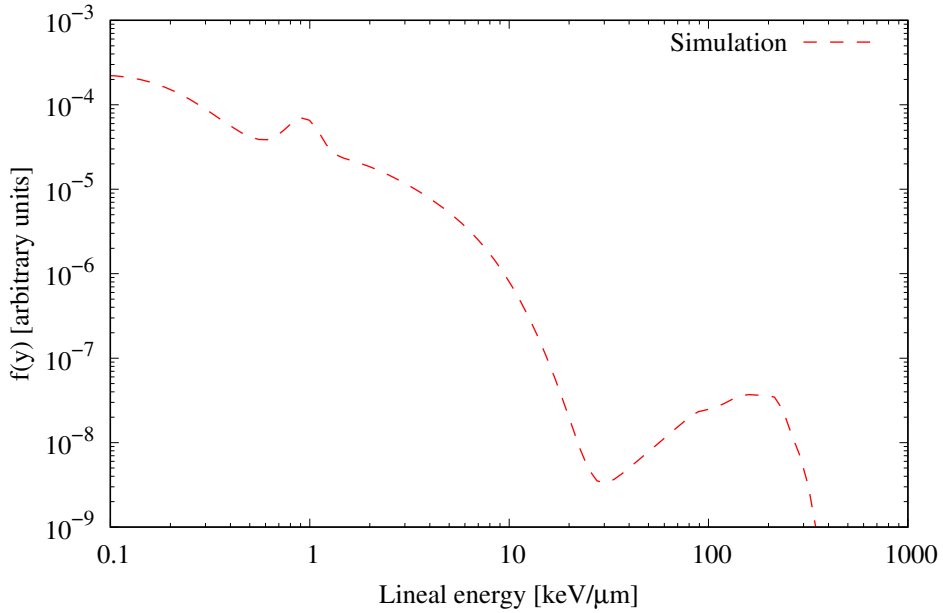

Figure 3.39: Frequency distribution curve of KUR mix mode obtained using a graphite walled counter simulated using PHITS.

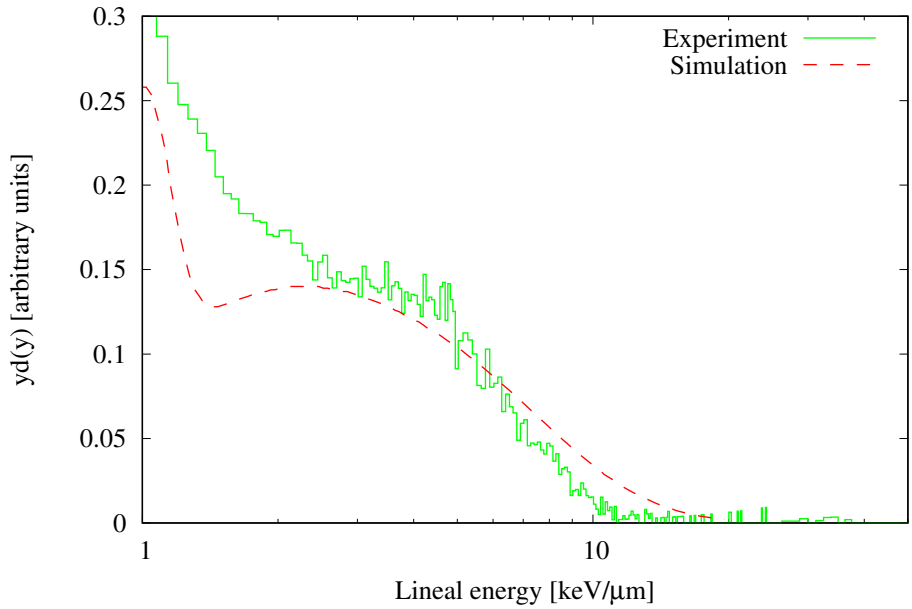

Figure 3.40: Dose distribution curve of KUR mix mode measured using a graphite walled counter.

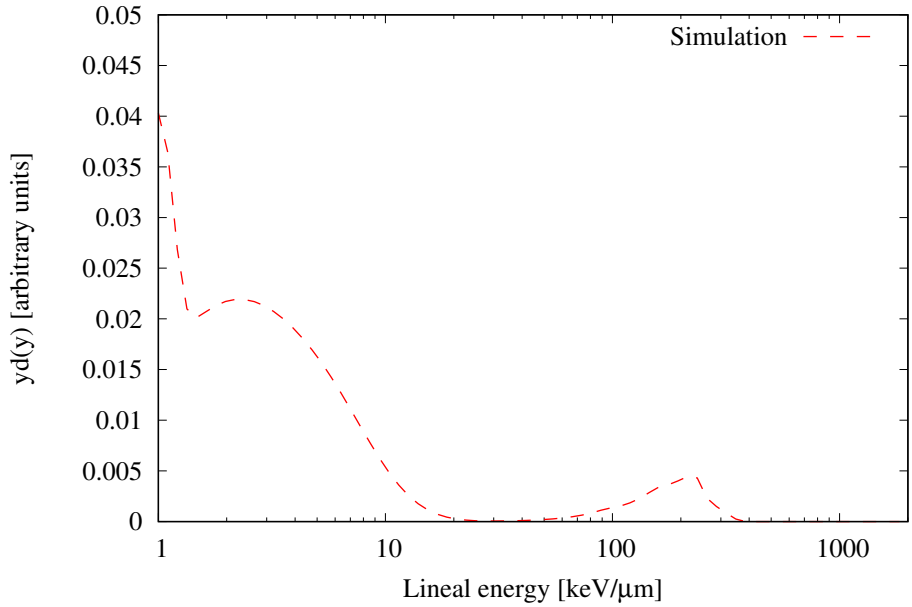

Figure 3.41: Dose distribution curve of KUR mix mode obtained using a graphite walled counter simulated using PHITS.

3.3.4 Measurement of microdosimetric spectrum of an accelerator-based neutron source

The raw spectrum obtained with the TEPC is shown in figure 3.42. The three spectrum were combined and the frequency distribution and dose distribution spectrum are shown in figure 3.43 and figure 3.44, respectively. Similar to the KUR mix mode results, the dominant dose component was the proton component. The PHITS calculation also showed nice agreement up to 150 keV/μm.

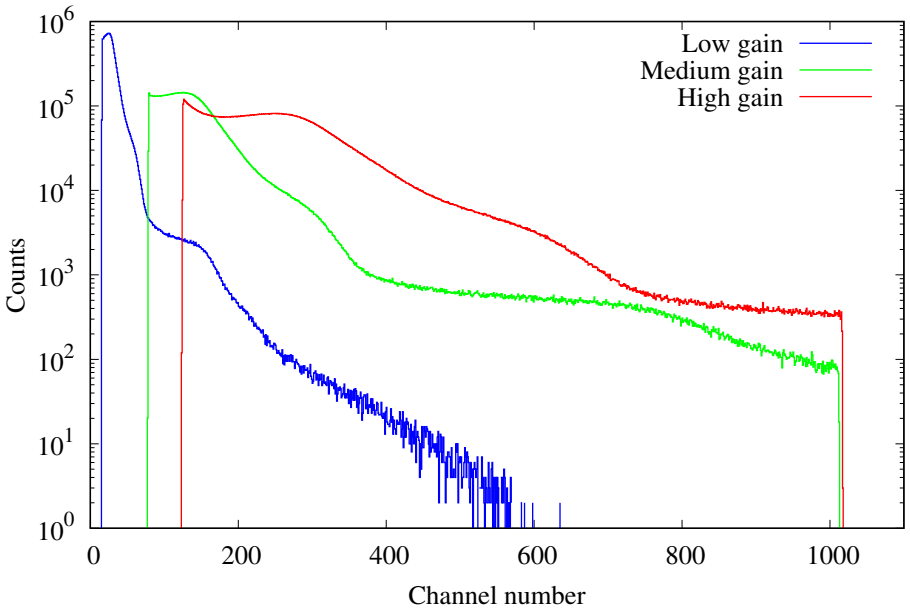

Figure 3.42: Raw spectrum of QSC AB-neutron source measured using TEPC obtained at three different gain settings.

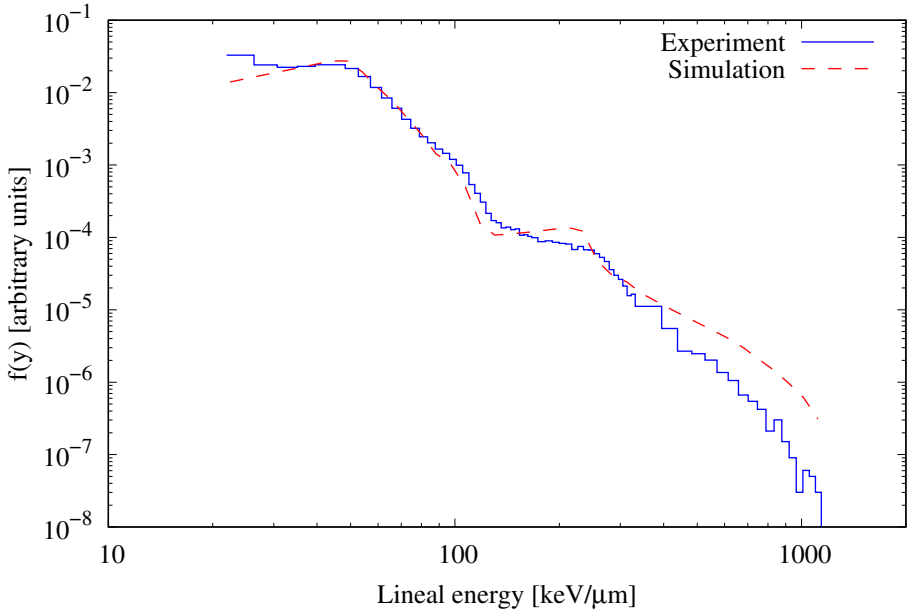

Figure 3.43: Frequency distribution curve of QSC AB-neutron source measured using TEPC compared against PHITS calculation.

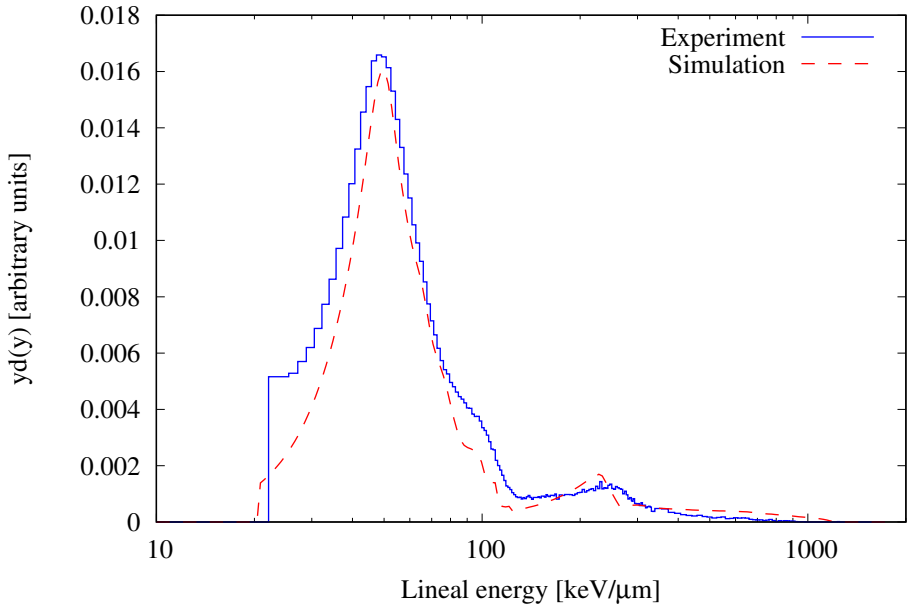

Figure 3.44: Dose distribution curve of QSC AB-neutron source measured using TEPC compared against PHITS calculation.

The frequency distribution and the dose distribution spectrum of the AB neutron source at QSC measured using the graphite walled proportional counter is shown in figure 3.45 and figure 3.47, respectively. Between the three neutron sources (KUR

epithermal, KUR mixed and AB neutron source at QSC), the AB neutron source at QSC had the largest gamma ray component. As a result, the frequency and dose distribution spectrum were smooth and closely matched the PHITS Monte Carlo calculation.

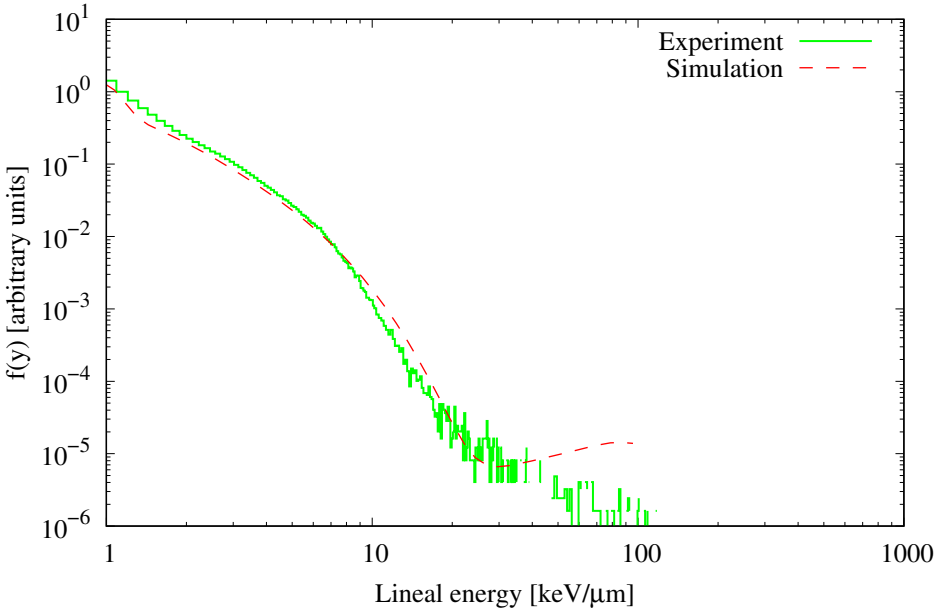

Figure 3.45: Frequency distribution curve of QSC AB-neutron source measured using graphite walled counter.

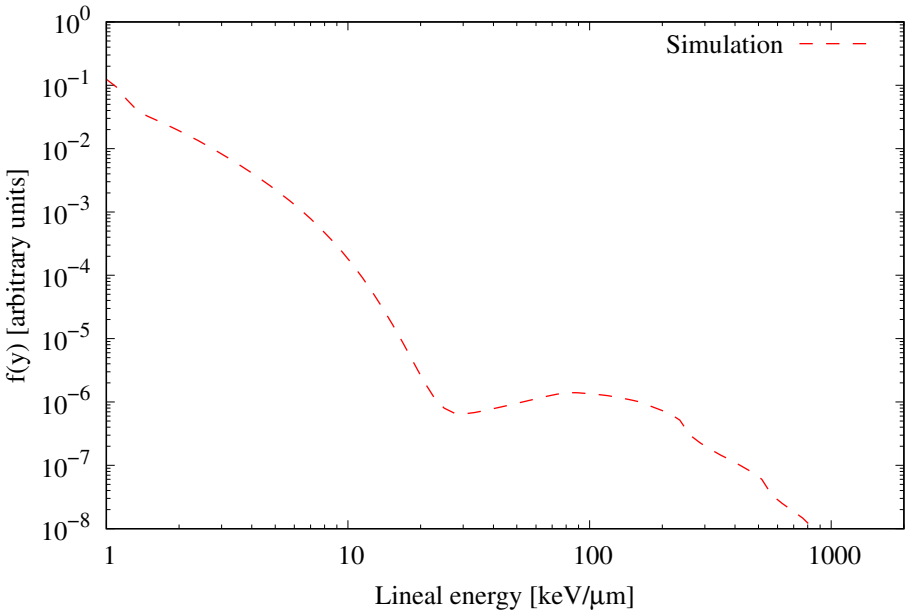

Figure 3.46: Frequency distribution curve of QSC AB-neutron source obtained using a graphite walled counter simulated using PHITS.

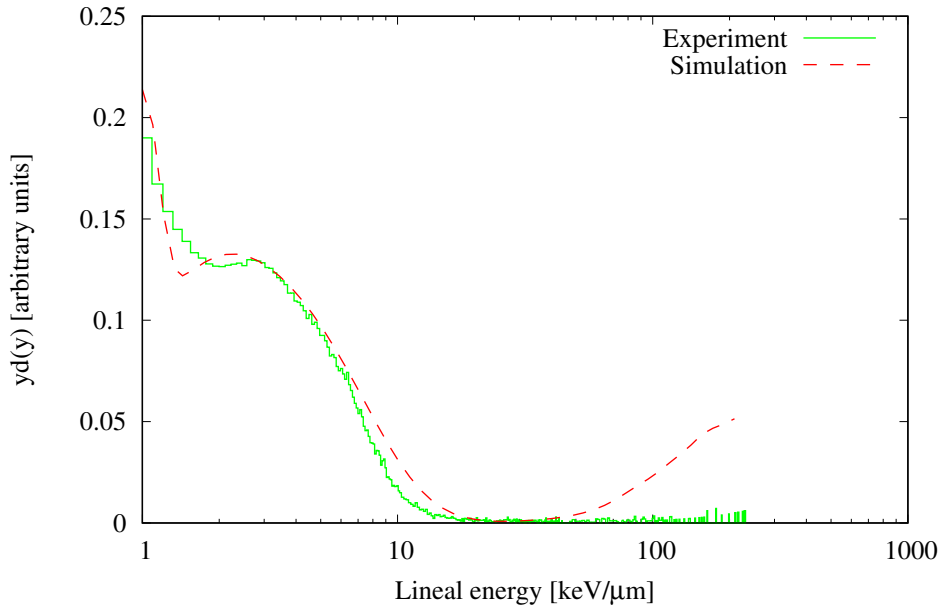

Figure 3.47: Dose distribution curve of QSC AB-neutron source measured using graphite wall counter.

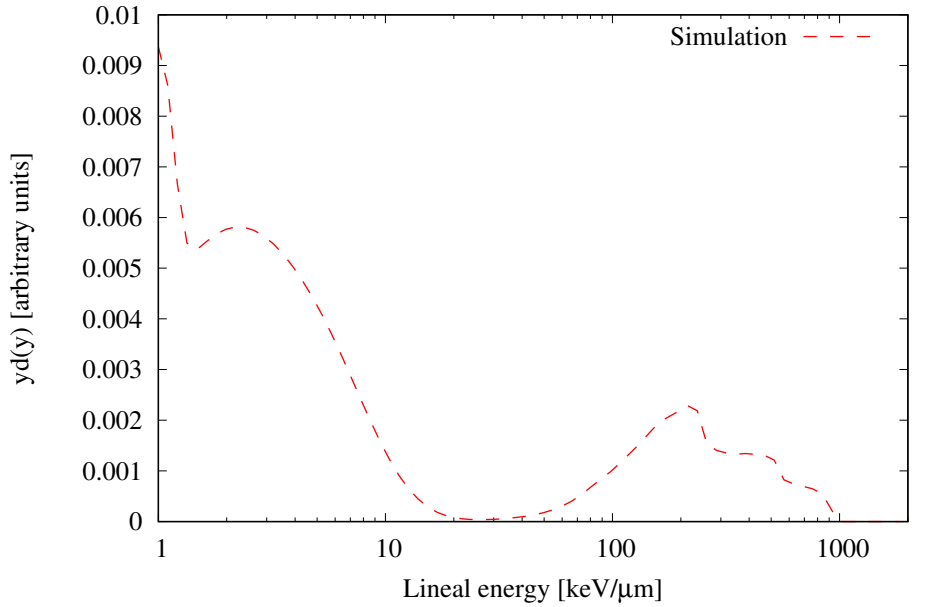

Figure 3.48: Dose distribution curve of QSC AB-neutron source obtained using a graphite walled counter simulated using PHITS.

3.3.5 Comparison of microdosimetric spectrum of a reactor based to accelerator based neutron source for BNCT

The comparison of the frequency distribution spectrum and the dose distribution spectrum obtained using the TEPC for KUR mix mode and QSC AB-neutron source are shown in figure 3.49 and figure 3.50, respectively. The QSC source was found to have higher counts at the high LET region. This was due to the fact the QSC neutron source had a larger fast neutron component as compared to the KUR mix mode irradiation. The QSC spectrum also had a larger background (i.e. higher threshold) than KUR mix mode. One reason could be due to the high radio frequency signal present in an accelerator environment, which added electrical noise to the detector system. The dose distribution curve showed the proton peak was higher with the QSC neutron source.

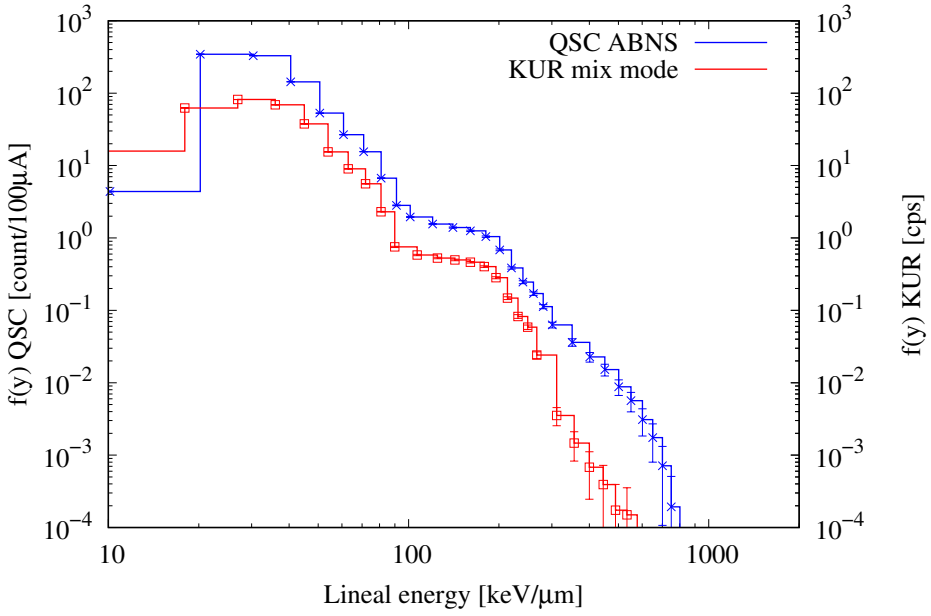

Figure 3.49: Comparison of KUR mix mode and QSC AB neutron source frequency distribution curve measured using TEPC.

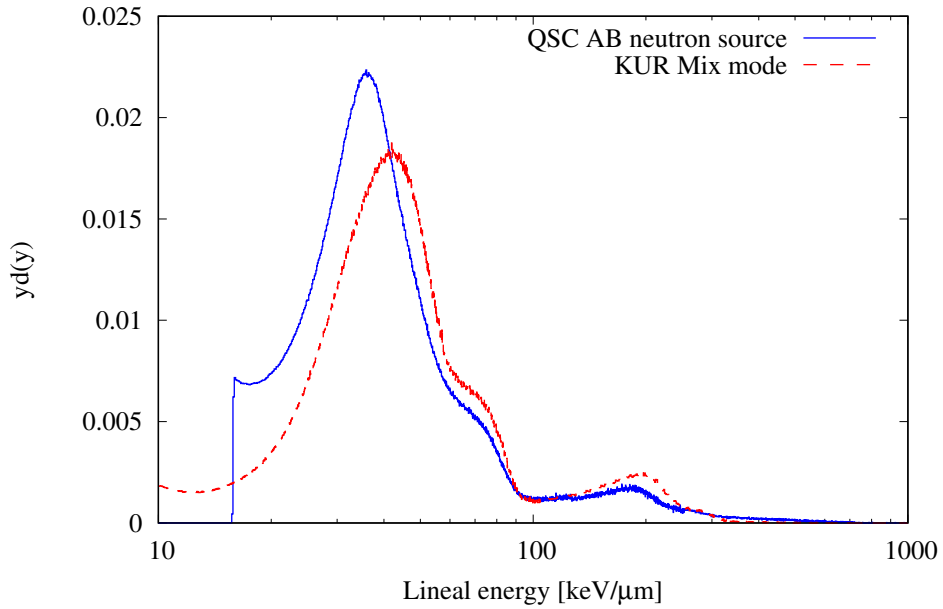

Figure 3.50: Comparison of KUR mix mode and QSC AB neutron source dose distribution curve measured using TEPC.

Table 3.4: Quantities derived from the microdosimetric single event lineal energy distribution measured with the TEPC

	$\bar{y_F}$(keV/μm)	$\bar{Q}$	D (Gy)	H (Sv)
Epithermal	59.9±3.1	7.5±0.5	0.6±0.1	4.4±0.3
Mix	45.7±2.5	13.2±0.9	10.9±0.7	125.3±6.3
QSC	46.6±2.4	14.2±0.8	11.5±0.7	163.3±8.2

3.3.6 Estimating relative biological effectiveness

Using 3.7 and the measured microdosimetric spectrum, the RBE of each neutron source was calculated and shown in table 3.5. For the KUR measured data (epithermal and mix mode), the *yd(y)* spectrum was integrated from 15 to 1000 keV/μm and the accelerator-based neutron source was integrated from 20 to 1000 keV/μm. Ideally, to accurately determine the RBE, the *yf(y)* spectrum should be integrated from 0 to infinite. This was not practical as the measured data contained electronic noise. Monte Carlo simulation assumes no electronic noise, so the PHITS calculated

yf(y) spectrum was integrated across the whole range and a more accurate RBE was calculated and shown in table 3.6.

Several authors have utilised the microdosimetric spectrum measured using a TEPC along with a lineal energy dependent biological weighting function to determine the RBE of a neutron field [109, 116, 117].

Table 3.6: RBE calculated by PHITS for different neutron sources.

Irradiation mode	RBE calculated by PHITS
Epithermal	3.0
Mix	2.9
QSC	3.0

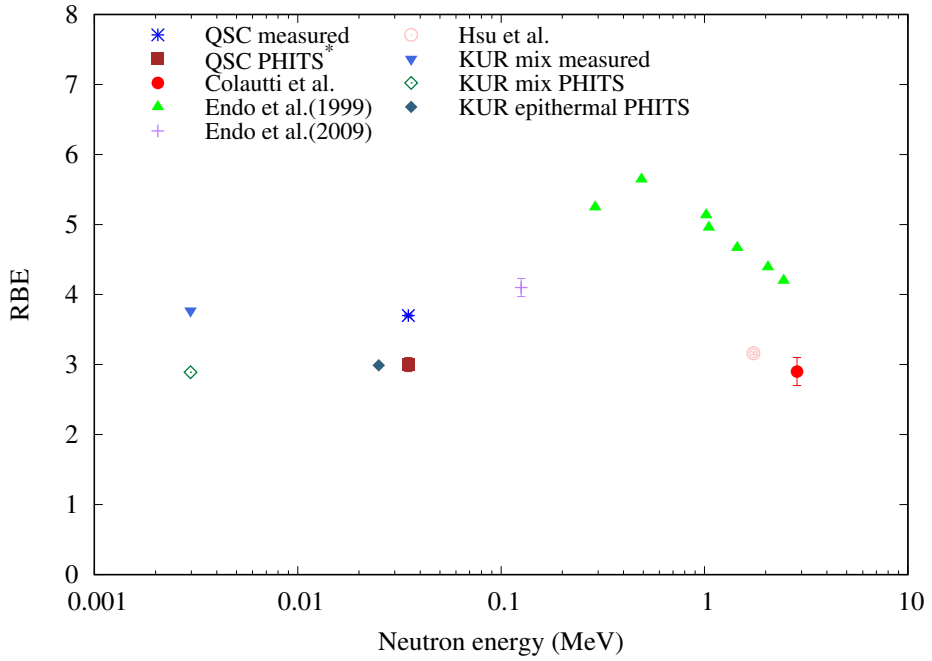

Figure 3.51: Comparison of RBE as a function of neutron energy calculated using a weighted biological function for various neutron sources.
**yf(y)* was integrated from 0 keV/μm to 1000 keV/μm.

Table 3.5: Dose mean lineal energy and RBE for different neutron sources.

	$\bar{y_D}$(keV/μm)		RBE	
	Measured	PHITS	Measured	PHITS
Epithermal[1]	69.9±3.6	68.9	3.8±0.1	4.0
Mix[1]	53.5±2.8	53.5	3.8±0.1	4.0
QSC[2]	53.6±2.8	57.7	3.7±0.1	4.0

[1] *yf(y)* was integrated from 15 keV/μm to 1000 keV/μm.
[2] *yf(y)* was integrated from 20 keV/μm to 1000 keV/μm.

3.4 Discussion and conclusion

The LET-1/2 0.5" proportional counter by Far West Technology was successfully characterised using the ^{252}Cf source. The gas leak test showed no significant leakage and showed that the detector can hold the gas pressure for few days without significant change in the gain. The microdosimetric spectrum of the ^{252}Cf source was obtained and the proton edge was used to calibrate the channel number to energy for the TE counter. The electronic noise in the system was high, such that the electron edge from the gamma rays were difficult to determine. The PHITS Monte Carlo simulation showed a nice agreement with measured data. The graphite walled proportional counter also showed nice results. Since this counter does not contain any hydrogen in the wall or the filling gas, the recoil carbons from elastic scattering and alpha particles from the ^{12}C(n, α) reaction produced in tissue can be simulated. The gamma ray component was detected, however, a longer measurement time was necessary to detect the high LET components. In conclusion, the LET-1/2 0.5 inch proportional counters were characterised using the ^{252}Cf neutron source.

The microdosimetric quantities were measured and agreed with PHITS Monte Carlo simulation. This detector can be utilised as a tool to determine the beam quality of different types of radiation. The beam quality of various neutron sources was measured using the TEPC. During data collection using the epithermal neutron beam, a low static electrical noise was present in the circuit. This was also observed during one of the ^{252}Cf measurement in the previous chapter. It was an intermittent issue and it could not be reproduced. The root cause of this signal was unknown; however, the detector system was very sensitive and prone to adding large amounts of noise to the system when it was physically bumped. With the KUR irradiation system, the TEPC and preamplifier was placed on the treatment couch, and once the set up was verified the couch moved into the irradiation room (known as the rail system). This couch motion could have played a role in adding static noise, such as unwanted cable movement, vibration of the detector or preamplifier. Due to the limited machine time, there was no opportunity to retract the couch back

to verify the source of the noise. To overcome this issue, the data collection mode was changed to list mode, which stores the single event data in time intervals. This allows one to observe and extract data between a specific time frame and if a large amount of noise was fed into the system at a certain time frame, it was removed. Hence, the measurements performed after the epithermal mode, which were the mix mode and accelerator-based neutron source, the low static electrical noise was able to be minimised. The measurements performed with the graphite walled proportional counter had a much lower noise compared to the TEPC. This allowed detection of the gamma ray components down to a few keV/μm. This result also suggested that the relatively large background noise with the TEPC measurement were caused by the detector itself and not in the circuitry system.

The RBE calculated from the measured microdosimetric *yd(y)* curve for the KUR epithermal and mix mode irradiation was 3.8 and 3.9, respectively. Endo et al. performed a similar measurement using the TEPC to measure the beam quality of the epithermal neutron beam at KUR [109]. Endo performed measurements inside a PMMA block with various thicknesses. The RBE at the shallowest depth (5 mm of PMMA) was calculated to be 3.6 with decrease in RBE as the depth increased. Another study by Endo et al. investigated the dose mean lineal energy as a function of neutron energy [118, 119]. The dose mean lineal energy was calculated to be approximately 60 keV/μm, which was similar to the measured values. The calculated RBE from measured results indicate a higher RBE than clinically accepted values for normal tissue, 3.0 [120, 121]. The difference was mainly due to the high noise in the measuring system, resulting in the exclusion of gamma ray component. Using PHITS Monte Carlo calculation, the full *yd(y)* spectrum was simulated and by incorporating the gamma ray component, the RBE of the neutron beam for normal tissue was calculated to be approximately 3. The accelerator-based neutron source at QSC was measured to have a higher dose mean lineal energy and RBE compared to the KUR mix irradiation mode. This was due to the fact the QSC neutron source had a slightly higher flux of fast neutrons. This is an important result since in the near

future, BNCT research and development will be moving toward accelerator-based neutron sources and it is important to understand the difference in the biological effect from the current standard (reactor based).

In conclusion, the microdosimetric single event spectrum was measured for the clinical BNCT field (epithermal) and non-clinical BNCT fields (mix and accelerator-based) using the TEPC. The RBE of the accelerator-based neutron source at QSC was slightly higher than the mix irradiation mode at KUR. The PHITS Monte Carlo calculation showed a nice agreement with measured microdosimetric spectrum and the calculated RBE values were close to the clinically utilised values. This showed that the PHITS T-SED calculation can be used to accurately calculated the microdosimetric quantities. Using a single response function to determine RBE is a suitable method to perform intercomparison between different centres, as described by Gueulette et al. [122]. However, RBE not only depends on the lineal energy, but it also depends on many other factors such as dose, dose rate, α/β ratio of the cell, endpoint etc. So hence, these calculated RBE values using a weighted response function may be used to characterise the radiation quality of a neutron beam, but it cannot be used for clinical purposes. A more realistic approach using information from survival experiments to calculate photon-isoeffective dose may be clinically suitable [123, 124].

Chapter 4

Investigation of the use of 3D bridge silicon on insulator microdosimeter for BNCT

4.1 Introduction

An ideal detector for the measurement of energy imparted and its distribution, as defined in ICRU report 36 [80], should meet the following criteria:

1. The distribution of energy imparted should be measured for the material of interest, usually tissue, which is regarded as a solid material.
2. It should be usable for determining the distribution over a sufficiently large range of volume sizes.
3. The entire range of energy imparted should be measurable.
4. The signal from the detector should be proportional to energy imparted.
5. The detector signal formed by the smallest energy imparted should be free from any fluctuations due to the detector itself.

A detector system which can fulfill all these requirements does not exist. A gas-filled detector, such as TEPC described in previous chapters, have been widely

used, however, there are several limitations with TEPCs. One of the well-known limitations of TEPC is the wall effect described in [80]. This effect causes distortion in the microdosimetric distribution due to the density difference between the cavity and the surrounding wall. This still occurs even when the gas inside the cavity and the wall composition are the same. The wall effect can be classified into four categories.

1. Delta ray effect: This is whereby a primary particle enters the cavity simultaneously with one of its delta rays. For a microscopic region, the distance between the two entry points are large enough that it is treated as separate signals (figure 4.1a). This effect is prominent for high energy, high LET particles that have a dense distribution of delta rays.

2. Re-entry effect: This is whereby an electron re-enters a cavity after it has traversed due to its curled track (figure 4.1b). This effect only applies to electrons and prominent for energies above 1 MeV.

3. V effect: This is whereby several charged particles are set in motion simultaneously from nonelastic nuclear interaction generated outside the cavity (figure 4.1c). For a microscopic region, the distance between the two entry points are large enough that it is treated as separate signals.

4. Scattering effect: This occurs when an uncharged particle interacts with the surrounding material and produces more than one charged particle which traverses through the cavity (figure 4.1d). In a real case, the two charged particle tracks may be far enough apart that only one of them would enter the cavity.

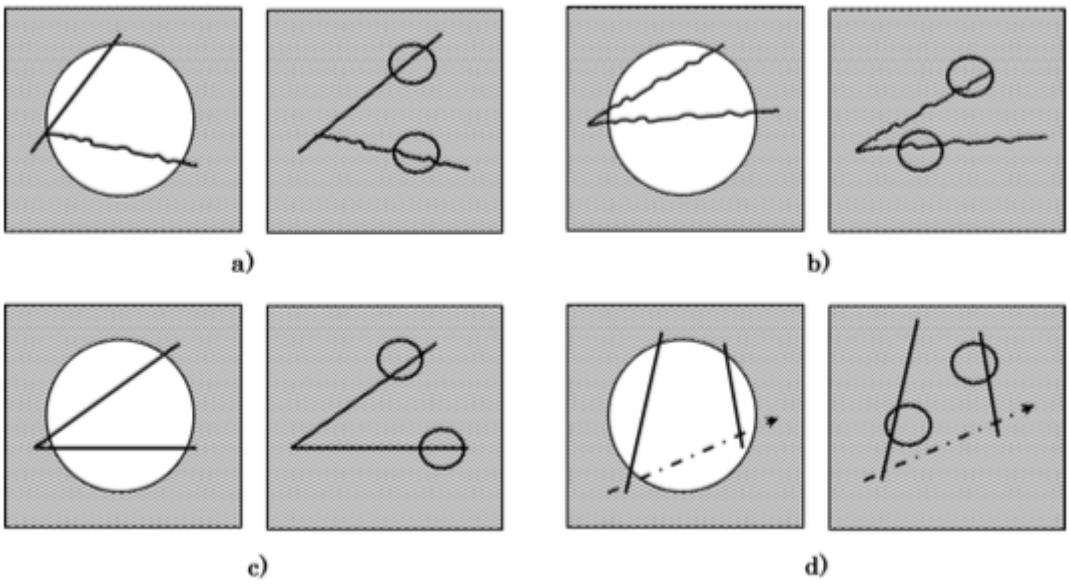

Figure 4.1: Diagram of the four types of wall effects for a proportional counter: a) delta ray effect, b) re-entry effect, c) V effect, and d) scattering effect.

The error caused by wall effects has been estimated on a theoretical basis by Kellerer [125, 126]. Kellerer found that delta-ray effect is important for heavy charged particles and high energy electrons. These delta-ray effects also cause distortions, where heavy charged particles produce one or more delta rays inside the cavity. For a 1 μm simulated diameter, these distortions are reported to be 3% to 8% for neutron energies between 10 and 30 MeV. The distortions add significant uncertainties in the frequency mean lineal energy. Other limitations include electronic noise, high voltage operation, large physical size and the ability to only mimic a single, isolated cell [4]. One of the interests in BNCT dosimetry is the determination of the dose delivered to the tumour cell by the boron component. To achieve this, a radiation detector capable of simulating a tissue cell size and the ability to deposit boron concentration in various regions in a cell is required. The TEPC can simulate a tissue cell, however, it is difficult to implant localised boron concentration into the detector.

4.1.1 3D bridge silicon on insulator microdosimeter

To overcome the drawbacks of the TEPC, the CMRP at the UOW developed a 3D bridge silicon on insulator microdosimeter. The bridge microdosimeter has a large sensitive area of 4.1×3.6 mm^2 having a total of 4248 individual SVs. The device is segmented into three sections to reduce the capacitance and reverse current. It is based on an array of planar 30×30×10 μm^3 SVs fabricated on a high resistivity 3 kΩ cm n-SOI active layer of thickness 10 μm and low resistivity supporting wafer. Each SV was fabricated using ion implantation to produce a square p-i-n diode structure. The SV rows were sectioned into even and odds rows with independent read out to avoid events in adjacent sensitive volumes being read as a single event. The P+ silicon layer has a depth of 0.2 μm constructed by ion implantation at 30 keV with an impurity concentration of 1.5×10^{15} cm^{-3}. In the case of silicon detectors, the ion implantation technique allows boron to be directly implanted to the chip. By changing the doping concentration or P+ layout, the boron distribution through the cell may be varied. Separate to direct boron implantation, a detachable boron converter can be used to model the biological situation where boron accumulates on the cell surface. Previous study by Bradley and Rosenfeld [127] used a thin film of aluminum backed Uranium-235. A boron carbide (B4C) nanoparticle has been recently used for advanced head and neck cancer treatment for BNCT [27, 128, 129]. Also, a thin B4C converter has been effective for neutron detection to determine thin film quality [130].

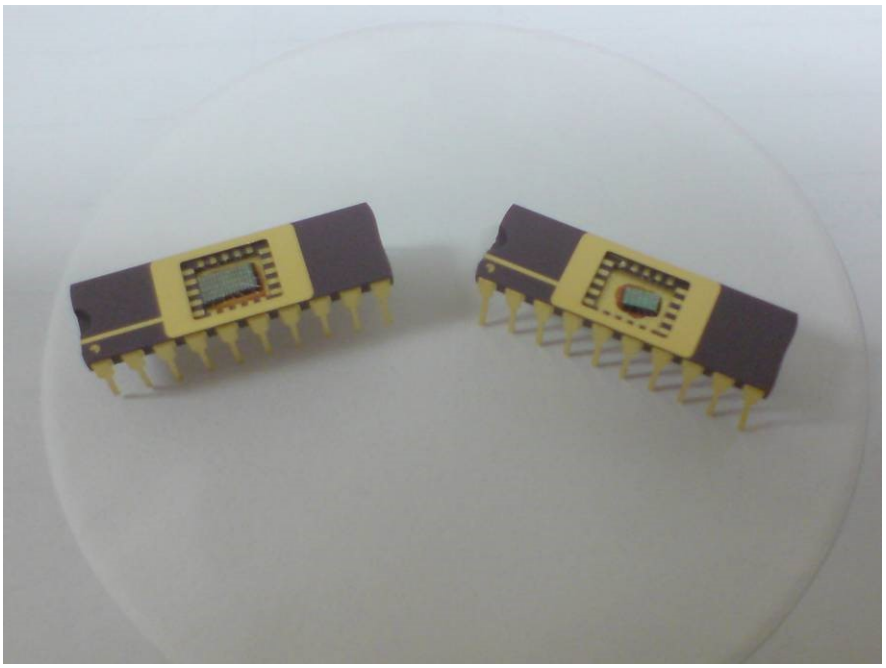

Figure 4.2: SOI microdosimeter chip.

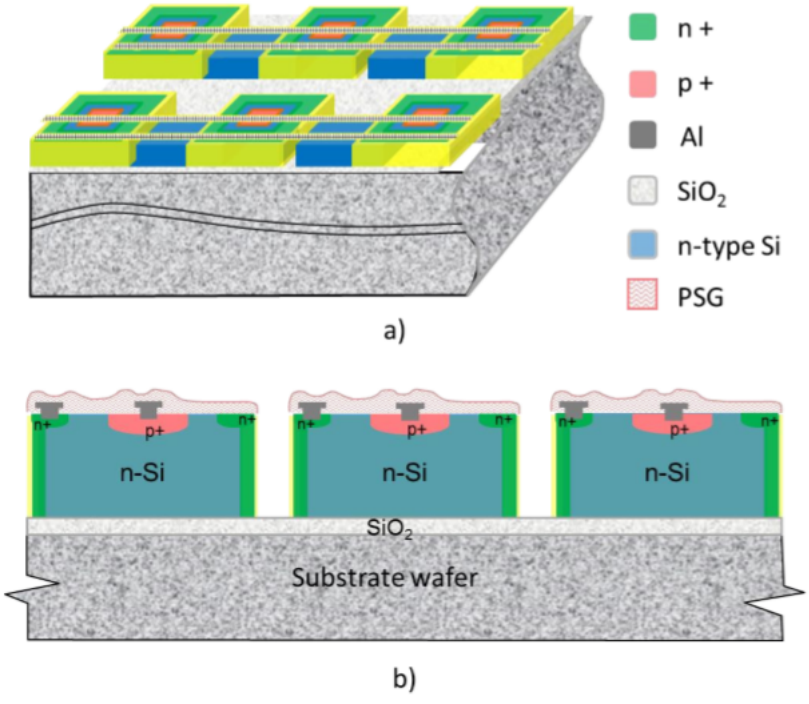

Figure 4.3: A schematic of the design of SOI bridge microdosimeter. a) 3D view; b) Cross-sectional view.

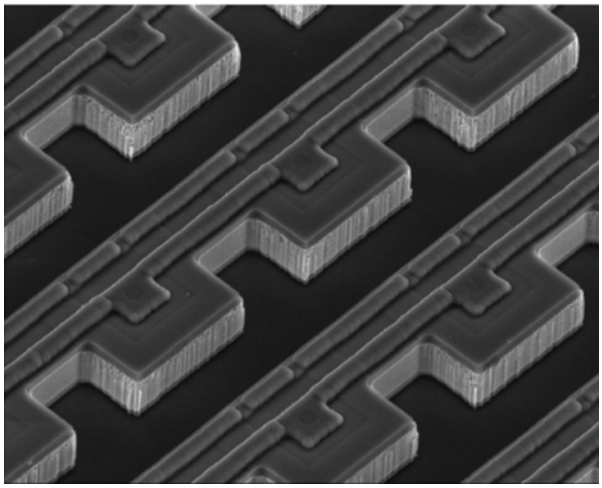

Figure 4.4: Scanned electron micrograph of the SOI bridge microdosimeter.

4.1.2 Modified 2 μm thick sensitive volume detector

For calculation of energy imparted, it is important to understand the five classes of track interactions within a target volume.

1. Insiders: Particles originating in the volume may lose their entire energy in the volume.

2. Starters: Particles originating in the volume may leave the volume before losing all their energy.

3. Stoppers: Particles originating outside the volume may enter the volume and stop within the volume.

4. Crossers: Particles originating outside the volume may cross the volume, depositing only part of their energy in the volume.

5. Touchers: Delta rays may enter the volume from the outside as particles pass by.

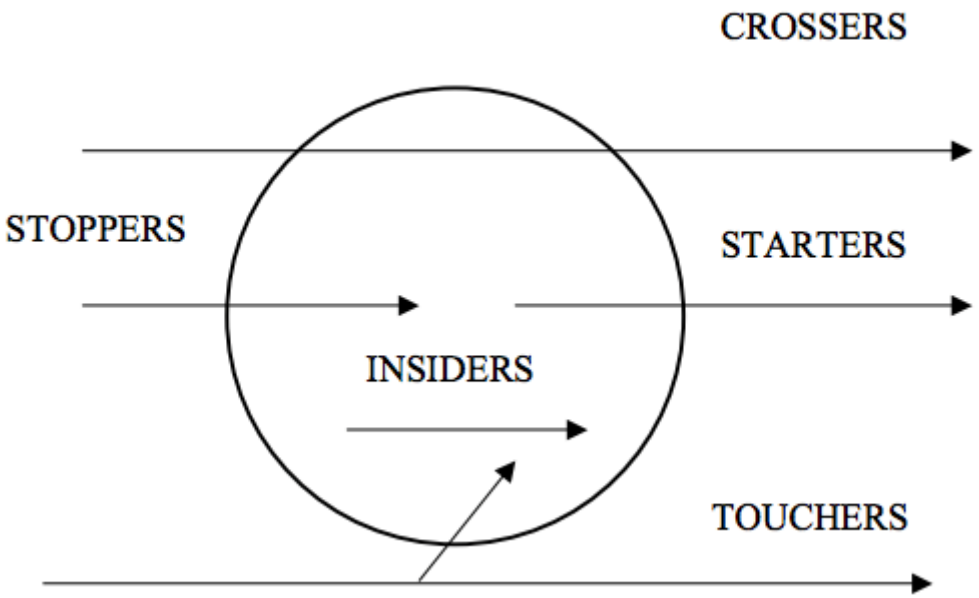

Figure 4.5: Diagram showing the five classes of tracks: crossers, insiders, starters, stoppers and touchers [11].

If the cavity size is large compared to the particle range, insiders are the dominant events. If the cavity is small, crossers are the dominant tracks (Bragg-Gray condition). In general, silicon detectors will only be appropriate in radiation environments where secondary charged particles produced in tissue have a range that is much longer than the mean chord length of the detector volume. The detector requirement is dependent upon the application in which they are intended to be used. For radiation protection, microdosimetric spectra may be used to determine the effective dose equivalent. Large uncertainties exist in the calculation method and measurement uncertainties of less than 30% are acceptable for radiation protection purposes [131]. On the contrary, dose determination in radiotherapy has a much stringent requirement of 5% accuracy due to the proximity of the curves relating to tumour control and normal tissue complications to absorbed dose [132]. The typical recoil products of BNCT and their ranges inside ICRU striated muscle obtained from SRIM are shown in table 4.1.

Table 4.1: Typical ranges of recoil products present in BNCT radiation field.

Typical products	Range (μm)
1.47 MeV alpha	7.7
0.84 MeV lithium	4.1
0.59 MeV nitrogen	10.5
0.04 MeV carbon	0.2

The lineal energy, defined as the ratio of the energy deposition by a particle in the biological target and the mean chord length of this target, is adopted to characterise the radiation quality. This definition is based on the approximation that the particle mean path length is equal to the target mean chord length. This approximation is valid for radiation that cross the target from outside (i.e. crossers). In the case of starters, insiders and stoppers, particle path lengths are always shorter than the target chord length. This give rise to the lineal energy not reflecting the specific energy deposition along the particle path. The sensitive volume thickness of the current detector is 10 μm. The alpha particle (1.47 MeV) and ^{7}Li ion (840 keV) generated from the nuclear reaction when ^{10}B captures a thermal neutron has a range of approximately 5 μm and 2.4 μm inside silicon, respectively. Therefore, for the 10 μm thick microdosimeter, many detected events will be stoppers. To measure the true specific energy deposition, a thinner, 2 μm thick sensitive volume detector was designed and tested using Monte Carlo simulation.

4.2 Material and method

4.2.1 3D bridge microdosimeter detector characterisation

4.2.1.1 Current-Voltage characteristic

Current-Voltage (IV) characteristic measurements were performed on each pin (row of parallel connected single detectors) to ascertain the electrical properties of the detector. A Keithley model 237 high-voltage source measure unit controlled using a Metrics ICS software was used to measure the IV. Parameters set on the Keithley model 237 are shown in table 4.2. A compliance level of 0.5 μA was set to prevent any damage to the detector from high current being drawn through the sensitive volume. When the current reached compliance, the Metrics ICS software was programmed to prevent further increases in voltage applied across the detector.

Table 4.2: Parameters set on the Keithley model 237 for IV measurements

Parameters	
Mode	Sweep
Type	Linear
Compliance	0.5 μA
Step size	1 V
Start - stop	0 - 15 V (negative bias)

4.2.1.2 Alpha particle spectroscopy

Alpha particle spectroscopy was performed to analyse the detectors response to alpha radiation. Alpha particle spectroscopy can provide detailed information about the energy loss in the over layers to determine their effective thickness and energy resolution of the silicon detectors. The spectral characterisation was performed using an ^{241}Am alpha emitting source. The detector and an Amptek A250 charge sensitive preamplifier were placed into a vacuum chamber to eliminate the absorption of alpha

particles by air. The preamplifier output was connected to an Ortec 571 shaping amplifier with a shaping time of 1 μs. The signal was recorded with an Amptek MCA 8000A Multi Channel Analyzer (MCA). The energy calibration was performed with an Ortec 419 precision pulse generator. The pulse generator was energy-calibrated with a fully depleted Hamamatsu S3590-09 300 μm thick windowless planar silicon PIN diode with 100% charge collection efficiency (CCE).

4.2.1.3 Ion Beam Induced Charge Collection study

The charge collection study was carried out using the Ion Beam Induced Charged Collection (IBICC) technique at the Australian Nuclear Science and Technology Organisation (ANSTO). The ANSTO heavy ion microprobe is located on a 10 MV ANTARES tandem accelerator with a beam size of a micrometre with a maximum mass energy product of 100 MeV/amu. The data acquisition (DAQ) system consisted of a software installed in Windows, a scanning amplifier, four 8192 channel Analogue to Digital Converters (ADCs), and a current integrator connected to the sample holder. The detector was mounted on an aluminium stick inside a vacuum chamber. The energy deposited in the detector was measured using an Amptek A250 charge sensitive preamplifier and Canberra 2025 shaping amplifier with a 1 μs shaping time. The signal was fed into a Canberra 8701 ADC of the DAQ. System. The microbeam position (x and y) and the energy deposited (ΔE) were saved for each event in a list mode file. This allowed for reconstruction of interaction maps, which display the median charge collected at different points in the device and show the variance with position of the number of interactions counted within a certain energy window. The images allow observation of the physical boundaries of charge collection with the array of diodes and illustrate the response uniformity of the devices and any charge collection characteristics that may affect its use as a microdosimeter. The energy was calibrated using a calibrated pulse generator, previously calibrated to a 300 μm thick planar silicon PIN diode.

4.2.2 Monte Carlo simulation

The detectors response under a neutron field used for BNCT was simulated using the Monte Carlo simulation code PHITS. Firstly, an optimal boron converter thickness was investigated for both the clinical BNCT beam (epithermal irradiation mode) and a non-clinical BNCT beam (mixed irradiation mode). Once this was determined, the energy deposition inside the sensitive volume of the detector when irradiated by neutrons were calculated with and without a boron converter in place. The microdosimetric spectrum, $yd(y)$, was calculated from the energy deposition by dividing the deposited energy by the average chord length of the sensitive volume. The average chord length of the sensitive volume was calculated to be 12 µm for the 10 µm thick detector and 3.5 µm for the 2 µm thick detector, using the following expression:

$$\bar{l} = \frac{4V}{S} \tag{4.1}$$

where V is the the volume and S is the surface area of the sensitive volume. However, this expression strictly only applies for a fully isotropic source. The source geometry used for the calculation was a 2pi geometry. To validate the use of this expression, the T-Track tally of PHITS, which calculates the fluence of a particle in any specified region, was used to directly calculate the chord length.

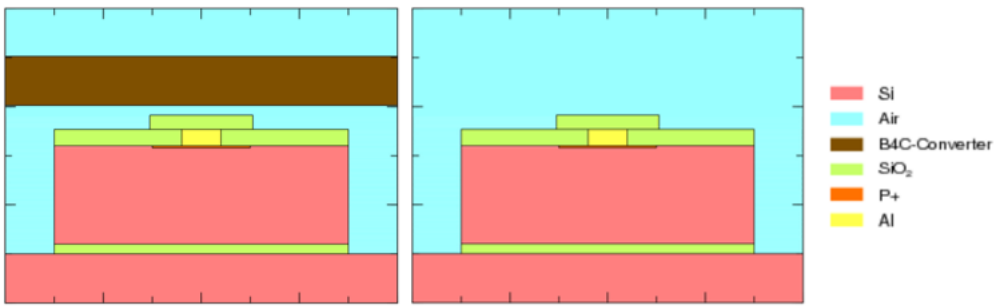

Figure 4.6: Cross section of an individual sensitive volume of the SOI bridge detector with (left) and without (right) the B4C converter modelled using PHITS.

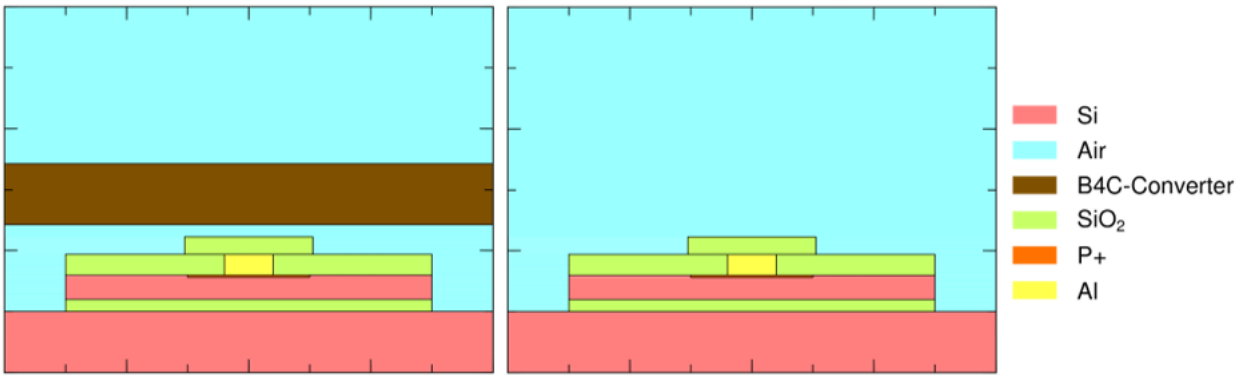

Figure 4.7: Cross section of an individual sensitive volume of the 2 µm thick SOI bridge detector (left) with B4C converter (right) without converter.

4.3 Results

4.3.1 3D bridge microdosimeter detector characterisation

4.3.1.1 Current-Voltage characteristic

The IV characteristics of the 3D bridge microdosimeter for segments 1 and 2 are shown in figure 4.8. At an operating voltage of 10 V, all pins (i.e. detector rows) had low leakage current ($<$ -3 nA). The IV characteristic of segment 3 is shown in figure 4.9. These rows of detectors were found to have high leakage current ($>$ -100 nA), which indicated a short in the circuit. Segment 3 was not used for further characterisation tests.

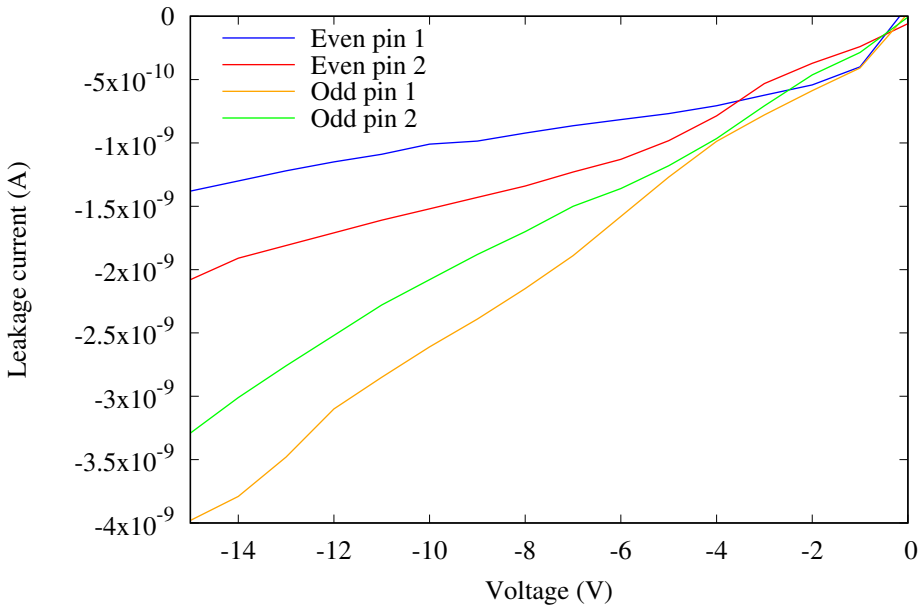

Figure 4.8: IV characteristics of odd and evens rows of segment one and two (pin 1 and 2) of the 3D bridge microdosimeter.

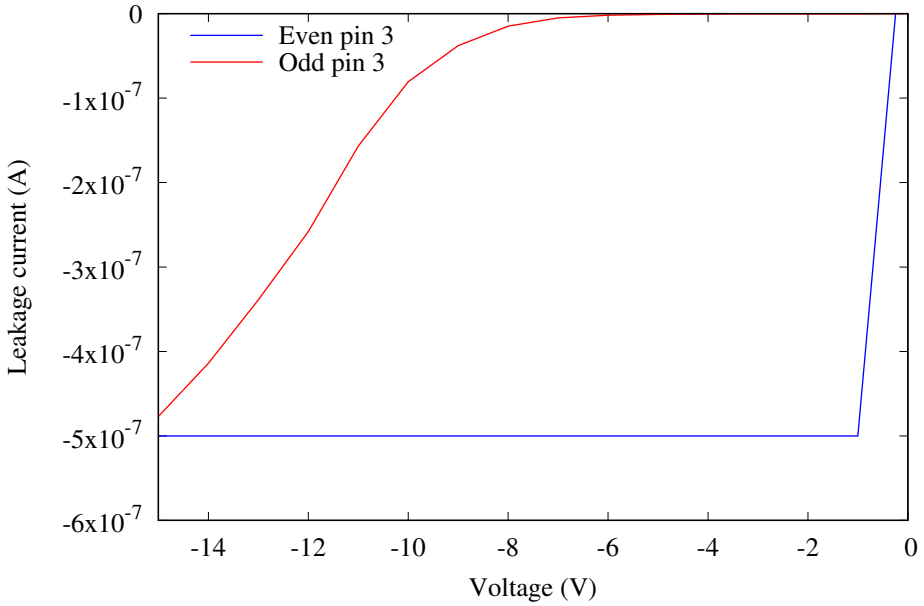

Figure 4.9: IV characteristics of off and even rows of segment three (pin 3) of the 3D microdosimeter.

4.3.1.2 Alpha particle spectroscopy

The energy of the alpha particles from the ^{241}Am source deposited in the sensitive volume of the detector is shown in figure 4.10. An alpha particle with an energy of

5.486 MeV has a stopping power of 133.4 keV/μm in silicon, calculated using SRIM [133]. Alpha particles traversing through 10 μm of silicon will deposit a total energy of 1334 keV. However, due to the over layer material (SiO_2, and aluminium contact layers) the alpha particles lost some of its energy before entering the sensitive volume. Using PHITS Monte Carlo simulation, the energy deposited inside the sensitive volume was calculated to be 1536.2 keV, shown in figure 4.11. The experimental result was 1566 keV which agreed with the simulation results within 2% uncertainty.

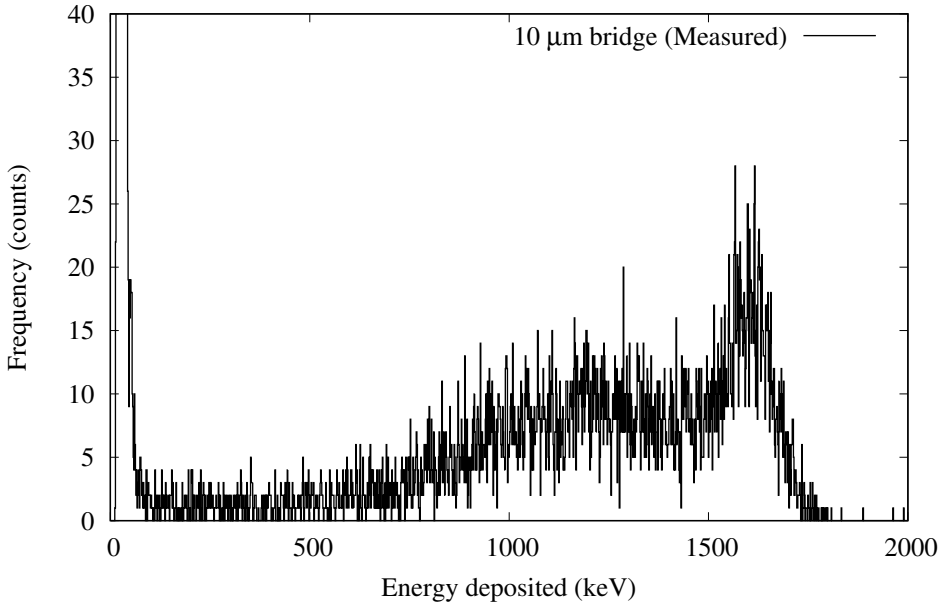

Figure 4.10: Alpha particle spectrum of ^{241}Am measured using the 3D bridge microdosimeter.

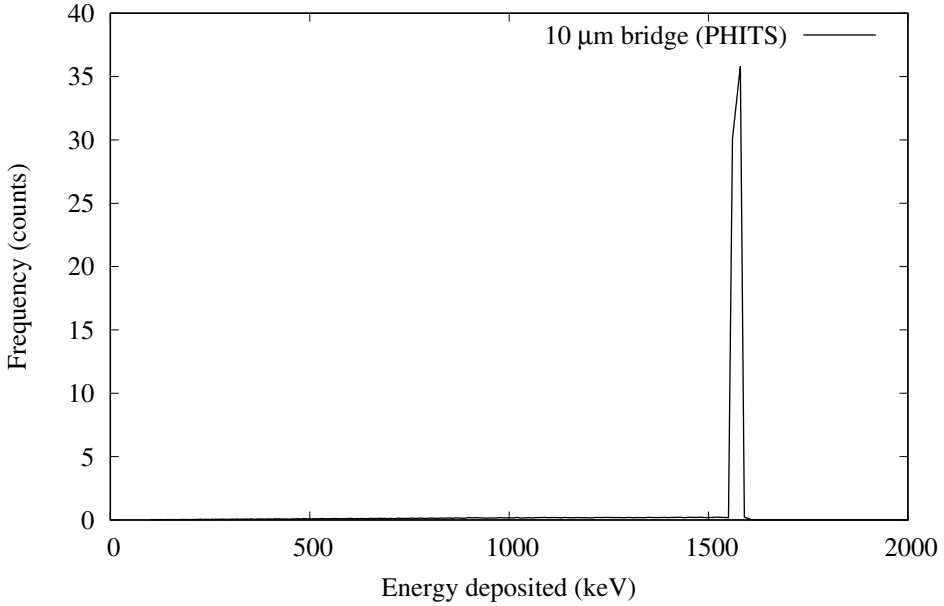

Figure 4.11: Simulated spectrum of 5.486 MeV alpha particles deposited inside the sensitive volume of the 3D bridge microdosimeter.

4.3.1.3 Ion Beam Induced Charge Collection

The MCA spectra and median energy map obtained with the 3D bridge microdosimeter at a bias of 0 V is shown in figure 4.12. The energy peak deposited in the 10 µm thick bridge microdosimeter was approximately 1350 keV, which was relatively close to the expected energy deposition of 1585 keV from 5.5 MeV He^{2+} ions traversing through the over layers and 10 µm layer of silicon, calculated with PHITS. The second peak on the left (approximately 900 keV) corresponded to the lower charge collection outside the active area of the p+ and n+ electrodes, when the alpha particles were incident onto the aluminium tracks across the bridge. The red region in the median energy map shows incomplete charge collection around the edges of the detector and across the bridge. The MCA spectra and median energy map obtained at a bias of 10 V applied to the detector is shown in figure 4.13. Compared to the 0 V results, a more uniform charge collection was obtained inside the sensitive volume of the detector, which resulted in a single Gaussian shaped curve. However, with a stronger electric field applied across the detector, the low energy events across the bridge region of the detector were being collected. This caused

broadening of the spectrum and shifting the peak to the lower end, approximately 1250 keV.

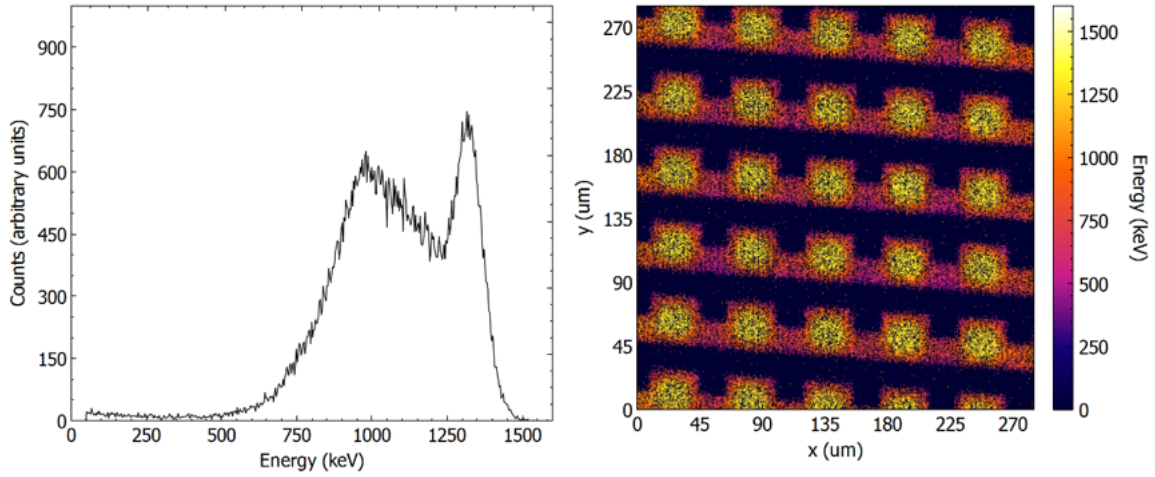

Figure 4.12: IBICC results for 3D bridge microdosimeter in response to 5.5 MeV He^{2+} ions. Left: MCA spectrum of the bridge microdosimeter at 0 V. Right: Median energy map of the bridge microdosimeter at 0 V.

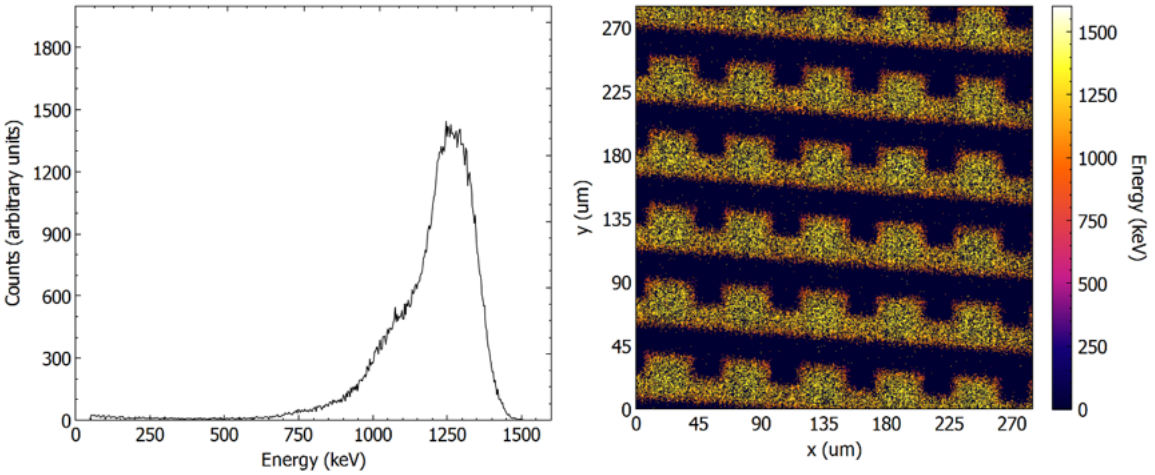

Figure 4.13: IBICC results for 3D bridge microdosimeter in response to 5.5 MeV He^{2+} ions. Left: MCA spectrum of the bridge microdosimeter at 10 V. Right: Median energy map of the bridge microdosimeter at 10 V.

4.3.2 Monte Carlo simulation under neutron field

4.3.2.1 Optimal converter thickness

The effect of converter thickness on the neutron spectrum is shown in figure 4.14. As the B4C converter thickness increased, the thermal neutron component (< 0.025 eV)

of the mix irradiation mode spectrum was attenuated and the thermal neutron flux dramatically decreased. The epithermal neutrons (0.025 – 0.4 eV) were less prone to attenuation and no significant change in the spectrum were observed up to 100 μm thickness of B4C converter. The alpha particle spectrum detected inside the sensitive volume of the detector is shown in figure 4.15. For the mix irradiation mode, the alpha particle flux was the largest at a converter thickness of 1 μm and reduced as the converter thickness increased. For the epithermal irradiation mode, the highest alpha particle flux was calculated at a converter thickness of 5 μm. The absorbed dose delivered by alpha particle and electrons inside the sensitive volume of the detector was calculated for each converter thickness, shown in figure 4.16. For the mix irradiation mode, as the thickness of the converter increased, the alpha particle dose decreased while the electron dose increased. For the epithermal irradiation mode, as the converter thickness increased the dose from the alpha particle also increased and reach a peak at 5 μm, then decreased from there on. The electron dose was similar to the mix irradiation mode. The overall dose delivered to the sensitive volume was higher for the mix irradiation mode, due to larger number of alpha particles produced from the high thermal neutron component.

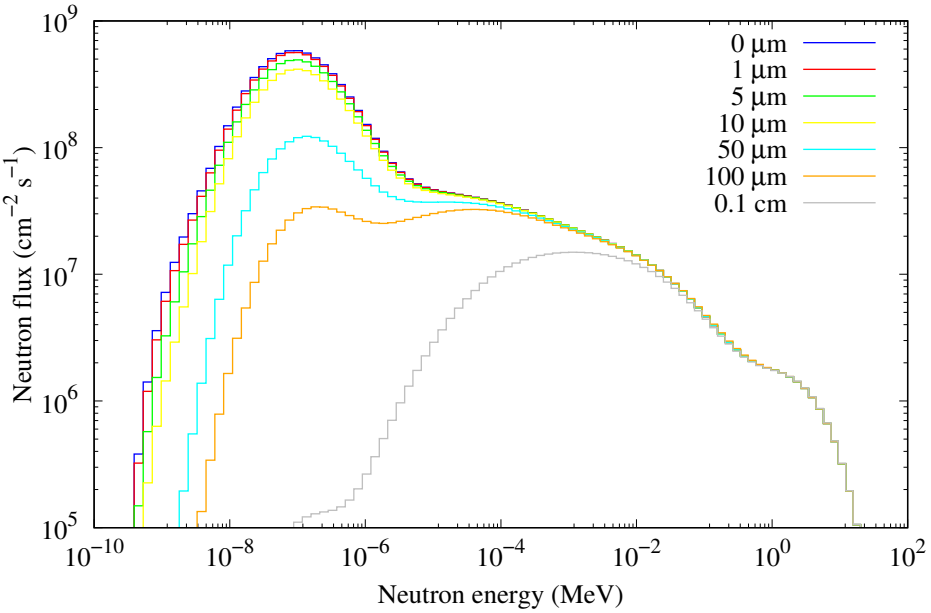

(a)

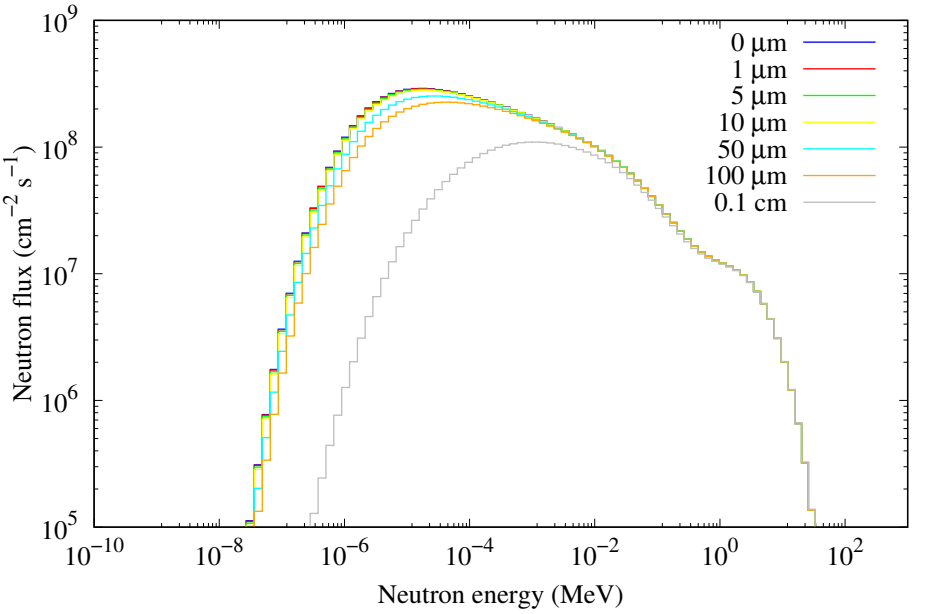

(b)

Figure 4.14: Neutron spectrum calculated inside the sensitive volume of the SOI bridge with various thickness of B4C converter for (a) KUR mix mode and (b) KUR epithermal mode.

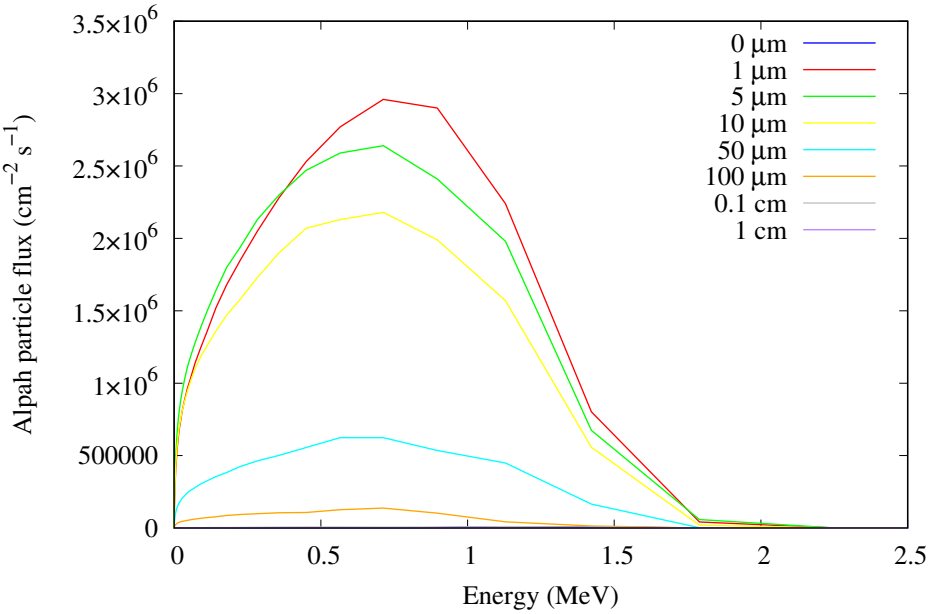

(a)

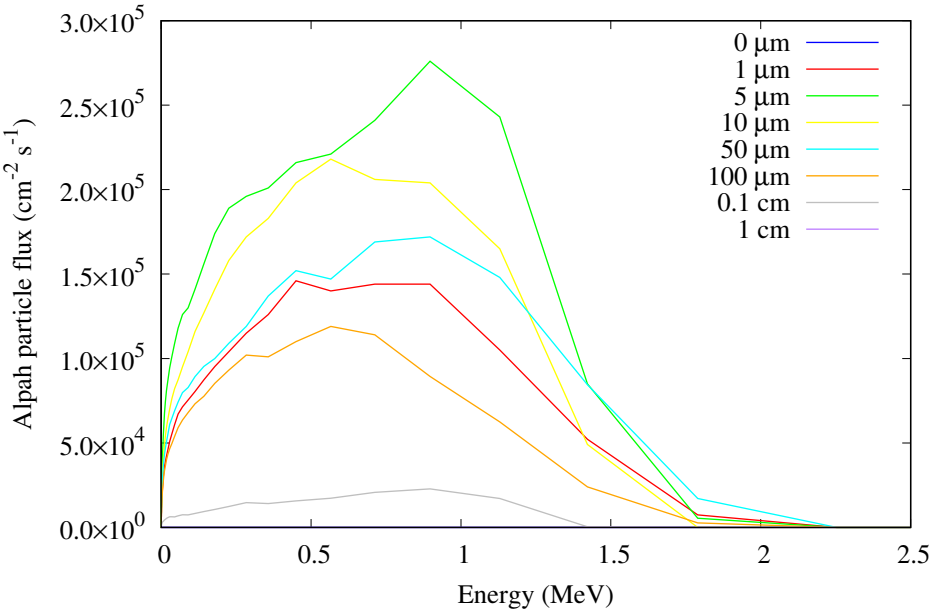

(b)

Figure 4.15: The alpha particle flux calculated inside the sensitive volume of the detector at various thickness of B4C converter for (a) KUR mix mode and (b) KUR epithermal mode.

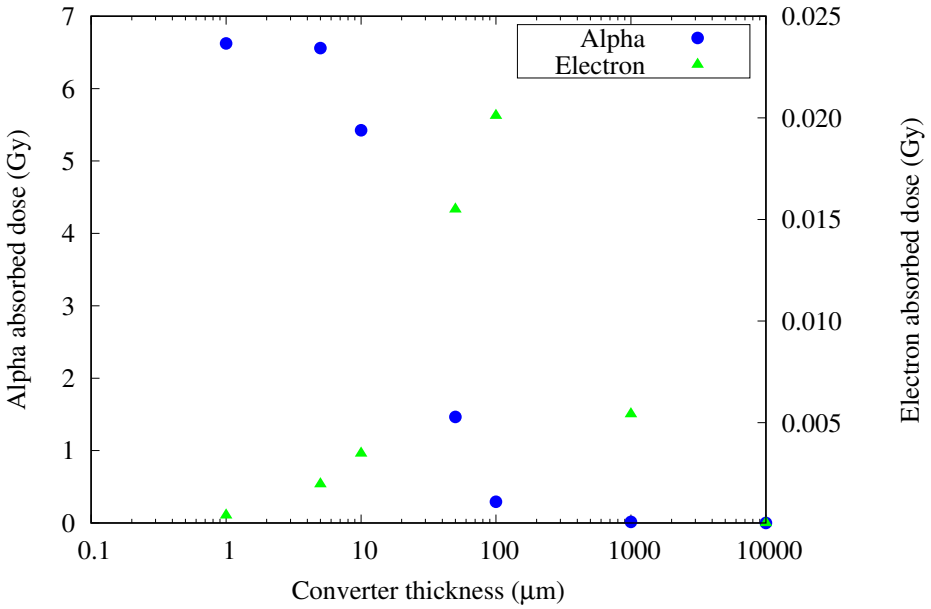

(a)

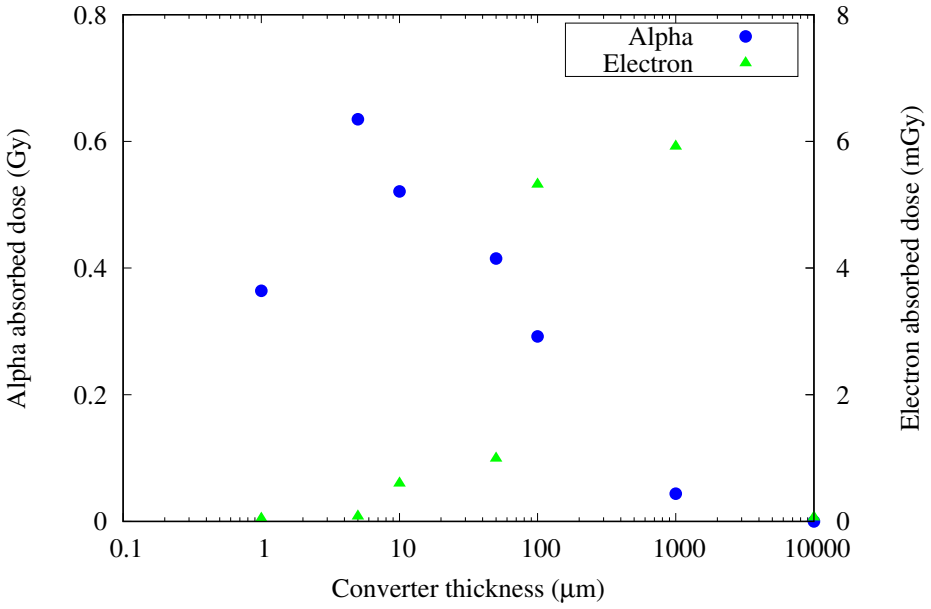

(b)

Figure 4.16: Alpha and electron absorbed dose calculated inside the sensitive volume at various converter thickness for (a) KUR mix mode and (b) KUR epithermal mode.

4.3.2.2 Energy deposition

The energy deposition inside the sensitive volume of the SOI bridge microdosimeter under neutron irradiation was calculated with and without the B4C converter. A 5 µm thick converter was used. The energy deposition spectrum when the bridge

detector was irradiated with the mix irradiation mode with the B4C converter is shown in figure 4.17. A large portion of events traversing the sensitive volume were found to be the alpha and ^{7}Li ions. A double peak feature was observed for the alpha particle deposited inside the sensitive volume. The peak at approximately 700 keV are events from the alpha particle generated in the boron converter that traversed through the silicon dioxide and aluminium over layers. The peak at approximately 1200 keV are also events from the alpha particle generated in the boron converter, but those that enter the sensitive volume laterally. These alpha particles are not attenuated and thus deposit a higher energy. The range and stopping power of 1.47 MeV alpha particle and 840 keV^{7}Li ion inside silicon, taken from SRIM (Stopping and Range of Ions in Matter) 2013 [133] is shown in table 4.3. To calculate the energy of the alpha and ^{7}Li ions that have traversed through the silicon dioxide and aluminium over layers, TRIM (Transport of Ions in Matter) was used to and the results are shown in table 4.4. The energy deposition spectrum for the non-converter spectrum is shown in figure 4.18. Due to the small area of the P+ region, only a small number of alpha and ^{7}Li ions traversed the sensitive volume. The low energy events were from the recoil Si ions. A similar spectrum was obtained with the epithermal irradiation mode, however, with much lower alpha and ^{7}Li events detected inside the sensitive volume.

Table 4.3: Range and stopping power of each particle inside silicon.

Particle	Energy (keV)	Range in silicon (μm)	Stopping power (keV/μm)
Alpha	1470	5.0	269.2
^{7}Li	840	2.5	486.9

Table 4.4: Range and stopping power of each particle after traversing through the over layers.

Particle	Over layer material	Energy (keV)	Range in silicon (μm)	Stopping power (keV/μm)
Alpha	SiO_2	914	3.2	311.9
	Al + SiO_2	405	1.70	333.7
^7Li	SiO_2	162	0.8	258.9
	Al + SiO_2	-	-	-

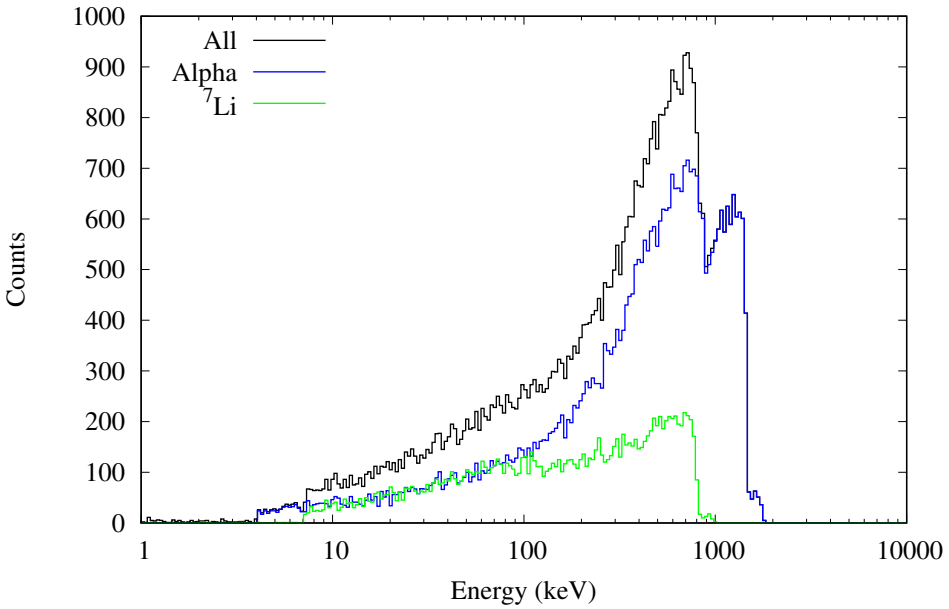

(a)

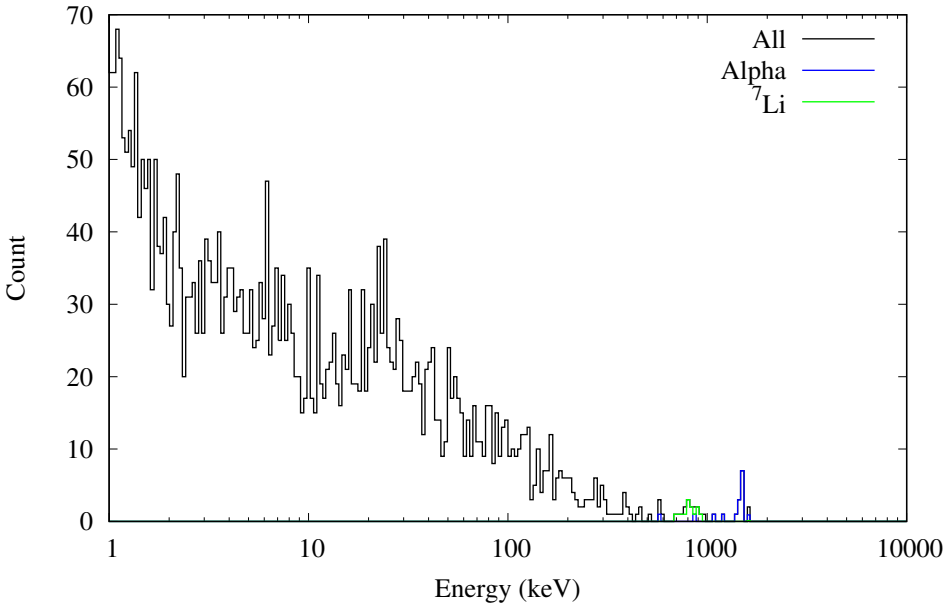

(b)

Figure 4.18: Energy deposit inside the sensitive volume of the SOI bridge using KUR epithermal mode (a) with B4C converter and (b) without converter.

The T-Track tally calculated the average chord length of the SOI bridge microdosimeter to be 12.21±0.05 μm. This showed the $4V/S$ formula expressed the average chord length of the SOI bridge reasonably well. By dividing the energy by the average chord length, 12 μm, the lineal energy was calculated and the $yd(y)$

spectrum was generated, shown in figure 4.19. For both converter and non-converter set up, the peak was observed around 100 keV/μm and a maximum at 130 keV/μm. An alpha particle with an energy of 1.47 MeV will deposit a maximum energy of approximately 260 keV/μm inside silicon. The discrepancy is due to the average chord length of 12 μm being longer than the range of the 1.47 MeV alpha particle in silicon. This shifts the $yd(y)$ spectrum to a lower lineal energy region. This is graphically represented by figure 4.20 and figure 4.21 which show ion tracks of 1.47 MeV alpha particle and 840 keV ^{7}Li ions travelling through the sensitive volume of the bridge detector, respectively. The image on the left represents the particles generated inside the converter layer only. The image on the right represents the non-converter set up, with alpha and ^{7}Li particles generated only from the P+ region of the sensitive volume. The alpha and ^{7}Li ions that are produced in the P+ region come to a full stop inside the sensitive volume.

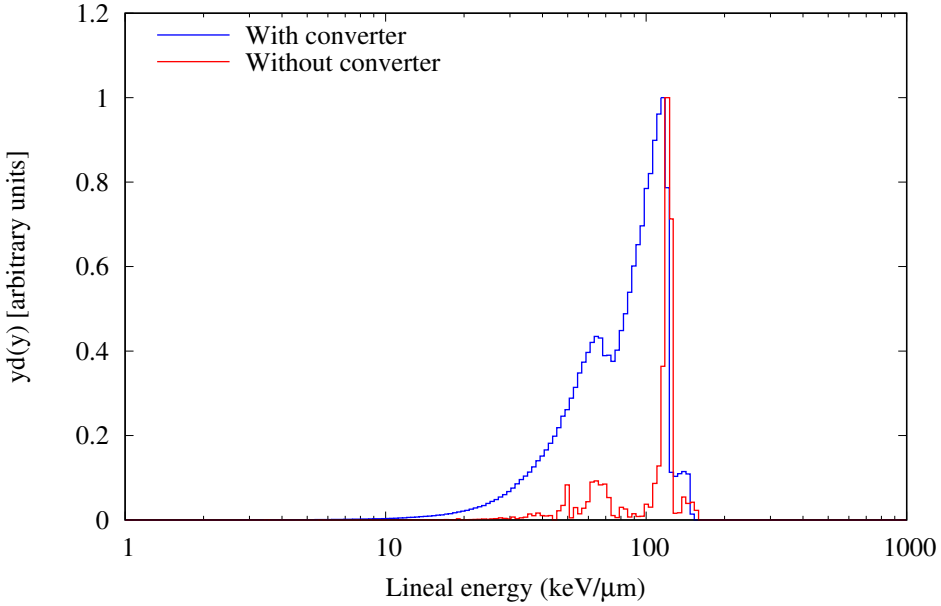

(a)

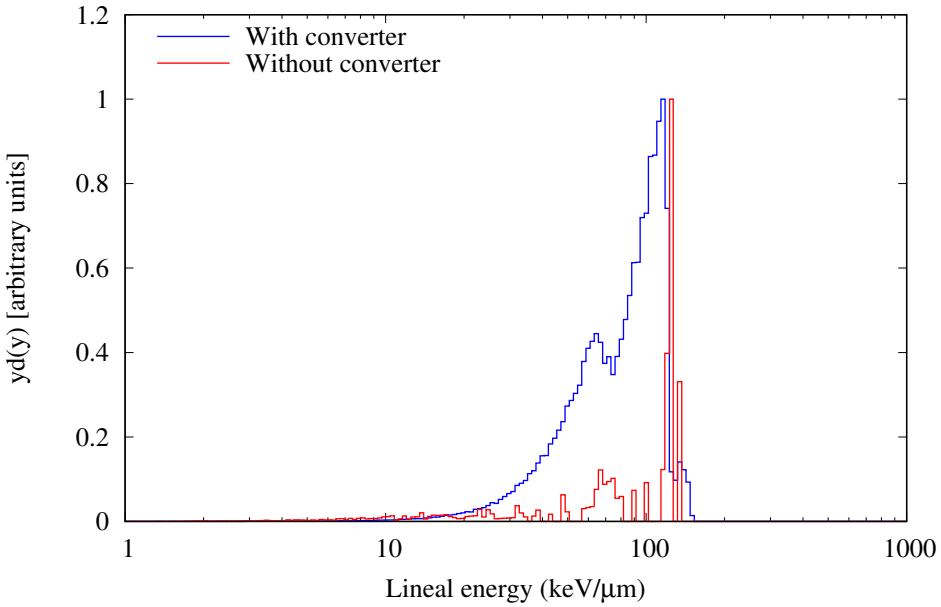

(b)

Figure 4.19: $yd(y)$microdosimetric distribution with and without converter for the (a) KUR mix mode and (b) epithermal irradiation mode.

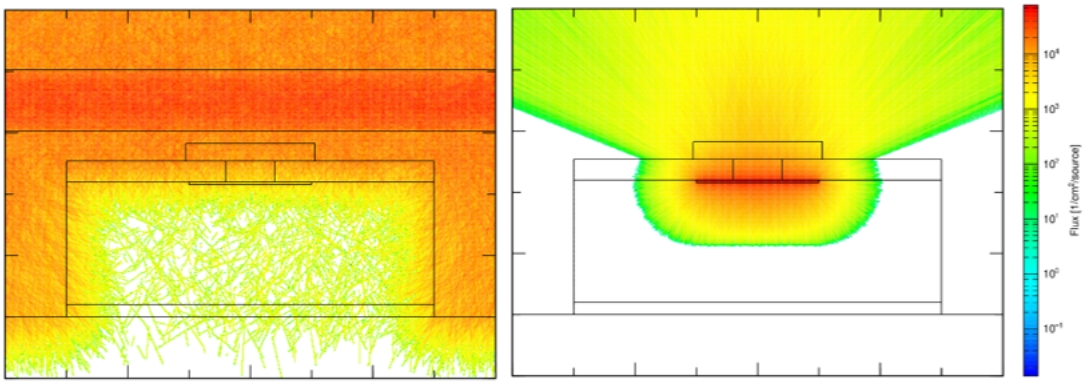

Figure 4.20: 2D ion track of 1.47 MeV alpha particles generated in the B4C converter (left) and in the P+ region (right).

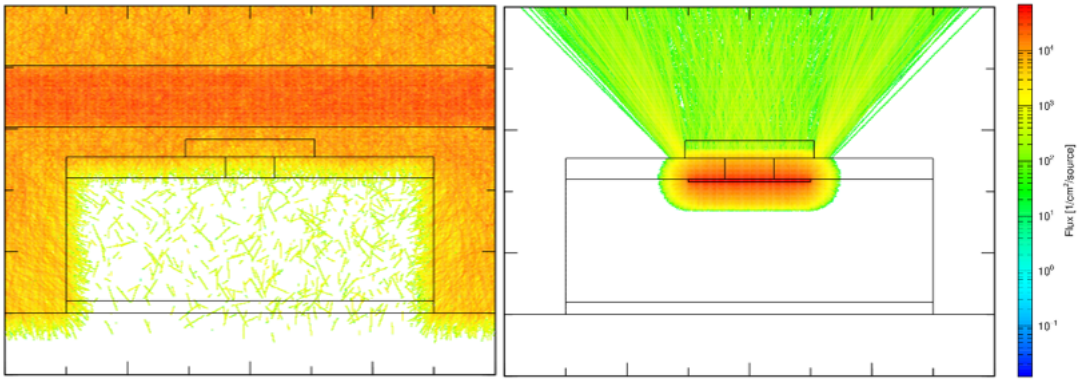

Figure 4.21: 2D ion track of 840 keV ^{7}Li ions generated in the B4C converter (left) and in the P+ region (right).

The energy deposition spectrum of the 2 μm bridge detector when irradiated with KUR mix mode is shown in figure 4.22. A single sharp peak at approximately 700 keV was observed, which correlated to the alpha particles traversing through the sensitive volume. The number of reaction particles entering from the side of the detector was reduced. Without the converter, only a few events were detected due to the small volume of the detector. The energy deposition inside the 2 μm detector when irradiated using the epithermal mode is shown in figure 4.23. Similar results were obtained, but with an even lower count than the mix mode results.

Table 4.5: Total number of stoppers and crossers inside the sensitive volume of the SOI bridge microdosimeter.

Particle	Without converter		With converter	
	Number of stoppers (%)	Number of crossers (%)	Number of stoppers (%)	Number of crossers (%)
Alpha	100	0	81	19
^{7}Li	100	0	94	6

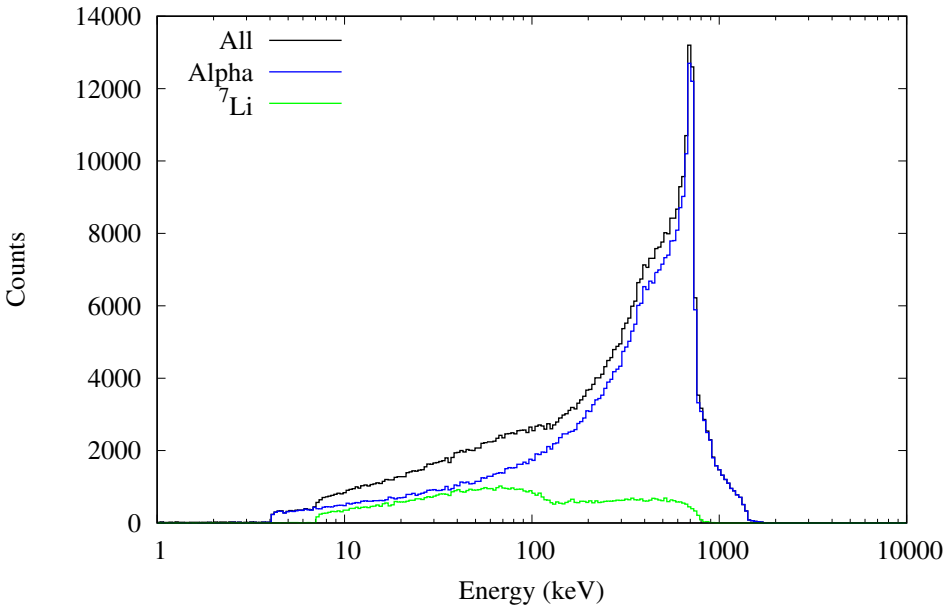

(a)

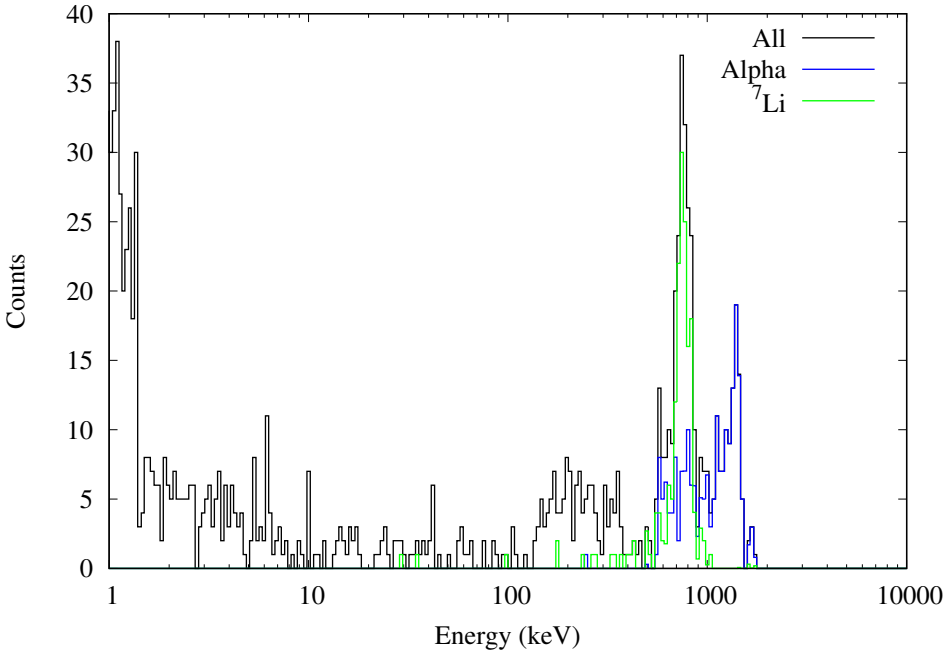

(b)

Figure 4.22: Energy deposition inside the sensitive volume of the 2 μm thick SOI bridge detector using KUR mix mode (a) with B4C converter (b) without converter.

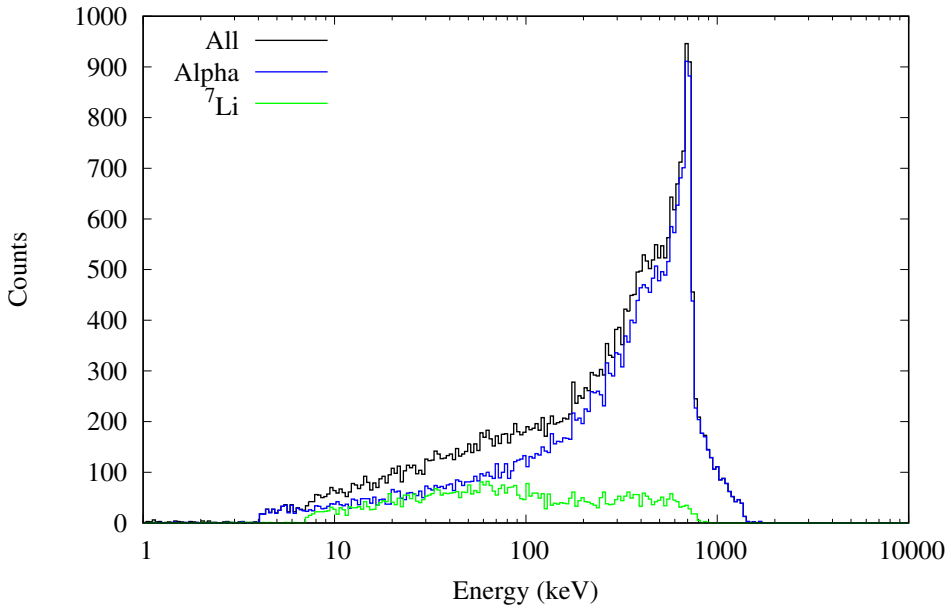

(a)

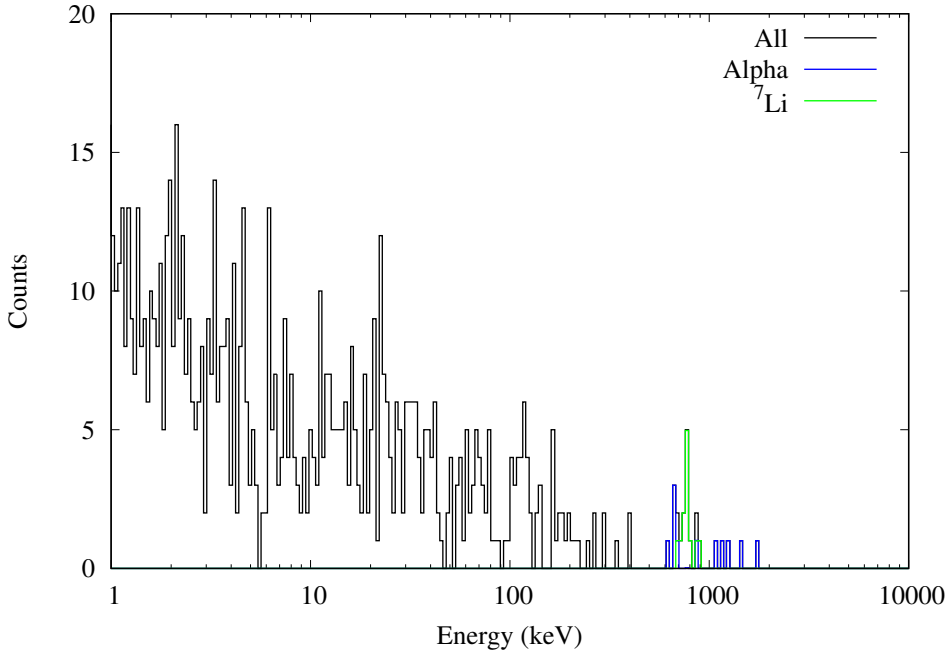

(b)

Figure 4.23: Energy deposition inside the sensitive volume of the 2 μm thick SOI bridge detector using KUR epithermal mode (a) with B4C converter (b) without converter.

The *yd(y)* versus lineal energy spectrum was generated and shown in figure 4.24. The left graph represents the KUR mix mode irradiation and the right graph represents the epithermal irradiation mode. With the converter, a peak in *yd(y)* at approximately 200 keV/μm was observed with a maximum at a lineal energy of ap-

proximately 400 keV/μm. This peak value at 200 keV/μm was close to the expected value of 260 keV/μm. The events greater than 260 keV/μm, observed for both converter and non-converter setup, were primarily the alpha particles traversing the sensitive volume in the lateral direction. The detector length in the lateral direction is 30 μm, so the alpha particle will come to a full stop inside the sensitive volume. The mean chord length was calculated to be 3.5 μm, which is shorter than the range of a 1.47 MeV alpha particle in silicon (approximately 5 μm). So, by dividing these events by the mean chord length, the *yd(y)* spectrum shifted toward a larger lineal energy.

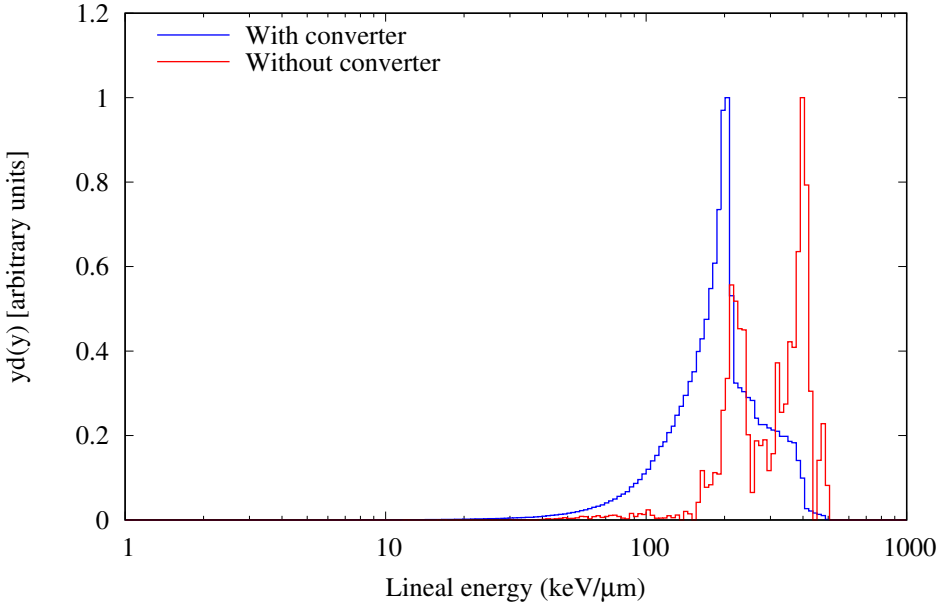

(a)

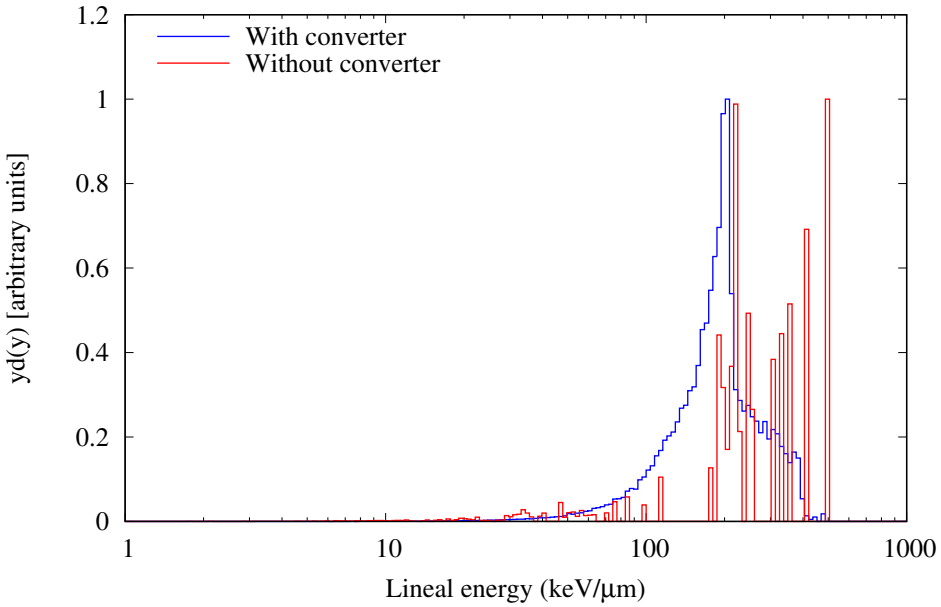

(b)

Figure 4.24: *yd(y)* microdosimetric distribution with and without converter for the KUR (a) mix mode (b) epithermal irradiation mode.

The 2D ion tracks of 1.47 MeV alpha particles and 840 keV ^{7}Li ions inside the detector are shown in figure 4.25 and figure 4.26, respectively. The ion track indicates that a proportion of the alpha and ^{7}Li ions generated in the P+ region and B4C converter traverse through the whole length of the sensitive volume. Those that

travelled laterally stopped inside the sensitive volume. The total number of crossers and stoppers inside the sensitive volume are shown in table 4.6. Compared to the 10 μm thick bridge detector, the number of crossers has increased.

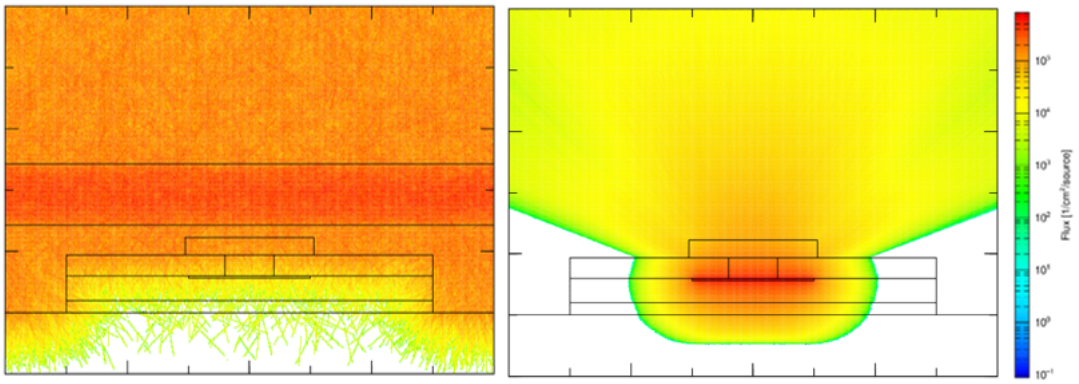

Figure 4.25: 2D ion track of 1.47 MeV alpha particle generated in the B4C converter (left) and in the P+ region (right).

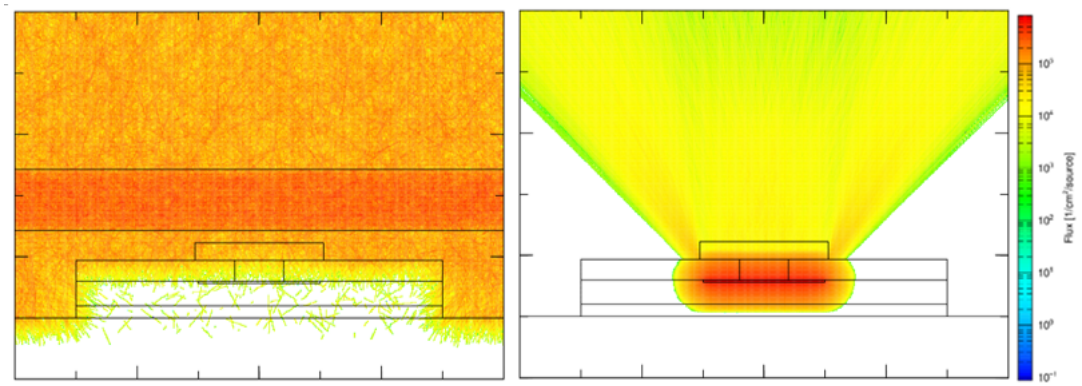

Figure 4.26: 2D ion track of 840 keV ^{7}Li ions generated in the B4C converter (left) and in the P+ region (right).

The *yd(y)* dose distribution spectrum of the alpha particle and ^{7}Li ion calculated for the two different detectors are shown in figure 4.27 and figure 4.28, respectively. The thinner sensitive volume detector (i.e. 2 μm) spectrum was shifted toward the higher lineal energy region, primarily due to more crossers as oppose to stoppers.

Table 4.6: Total number of stoppers and crossers inside the sensitive volume of the 2 μm thick SOI bridge microdosimeter.

Particle	Without converter		With converter	
	Number of stoppers (%)	Number of crossers (%)	Number of stoppers (%)	Number of crossers (%)
Alpha	73	27	71	29
^{7}Li	94	6	93	7

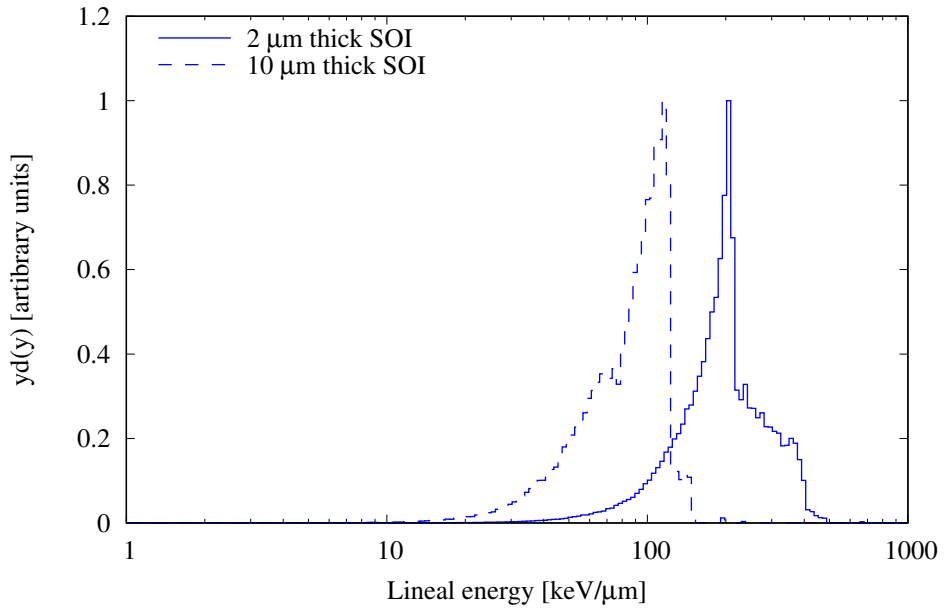

Figure 4.27: *yd(y)* microdosimetric spectrum of alpha particles inside the sensitive volume of the SOI bridge detector.

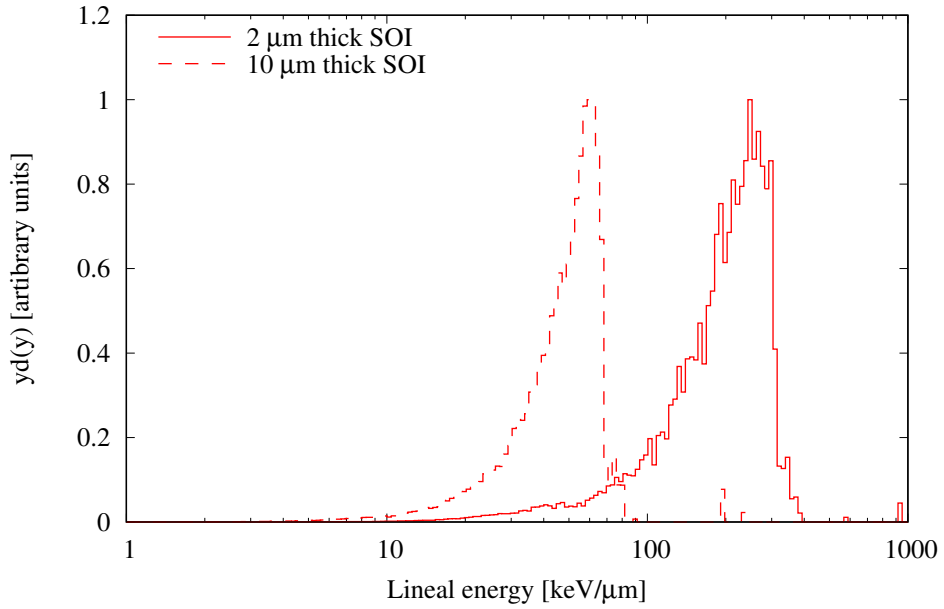

Figure 4.28: *yd(y)* microdosimetric spectrum of ^{7}Li particles inside the sensitive volume of the SOI bridge detector.

4.4 Discussion and conclusion

The characterisation of the SOI bridge microdosimeter was performed at the detector lab in ANSTO. The electrical characterisation (I-V measurements) indicated which segment was functioning (i.e. low reverse current). Following the I-V measurement, alpha particle spectroscopy was performed using the functioning rows of the detector. The results showed excellent response to alpha particles. Once the response to alpha particles were evaluated, the charge collection study was performed using IBICC. The charge collection inside the sensitive volume of the detector was measured and results showed a near 100% charge collection inside the sensitive volume.

The feasibility of the SOI bridge microdosimeter for BNCT dosimetry was performed using PHITS Monte Carlo simulation. For in air measurements, a 1 μm thick boron converter was optimal for mix neutron irradiation mode as it produced the greatest number of reaction particles and had the least effect perturbation effect. For the epithermal irradiation, due to the buildup effect, a slightly thicker 5 μm converter was found to be the optimal thickness in generating high number of reaction particles. A 5 μm B4C converter was found at have little effect on the neutron beam perturbation for both mix and epithermal irradiation mode, it produced high number of alpha and ^{7}Li ions and low number of secondary electrons, so this thickness was used for calculation for both irradiation modes. The energy deposition spectrum showed with the B4C converter present, many alphas and ^{7}Li ions were detected inside the sensitive volume. Without the converter, a few alpha and ^{7}Li ions generated inside the P+ region were deposited inside the sensitive volume, but many events were predominantly recoil silicon ions. The energy deposition spectrum was converted to the $yd(y)$ microdosimetric spectrum and it was found that the 10 μm thick sensitive volume was too large to accurately calculate the $yd(y)$ versus lineal energy distribution. To accurately calculate the microdosimetric distribution, a smaller detector geometry was found to be necessary.

A 2 μm thick SOI microdosimeter has been fabricated and tested previously [134]. The result indicated that a 2 μm thick SOI bridge detector with functioning

detector rows was possible to fabricate. For accurate determination of microdosimetric measurements, the radiation passing the sensitive volume of the detector should ideally be crossers. With the 2 μm thick bridge detector, the number of crossers had increased in comparison to the 10 μm thick detector. This was reflected on the *yd(y)* microdosimetric dose distribution spectrum of alpha and ^{7}Li ions. The dose distribution spectrum for the 2 μm thick detector shifted to the right, moving the peak closer to the expected lineal energy. The alpha particle and ^{7}Li ions generated in the B4C converter and P+ region travel in a 2pi direction. Those that travelled parallel to the neutron beam (i.e. sensitive volume thickness direction) were crossers, as the alpha particle and ^{7}Li ion ranges were greater than 2 μm inside silicon. Those that travelled perpendicular to the neutron beam (i.e. laterally across the sensitive volume) were stoppers, as the lateral dimension of the sensitive volume was 30 μm which was larger than the range of the particles inside silicon. To detect a higher number of crossers inside the sensitive volume, the lateral dimension of the sensitive volume also needs to be considered. Due to the fact the 2 μm thick SOI bridge detector has a smaller volume than the 10 μm thick detector, the number of particles entering the sensitive volume was low, therefore producing lower number of events. To obtain sufficient number of events to observe the alpha and ^{7}Li ions, a longer irradiation time than the 10 μm thick detector will be necessary.

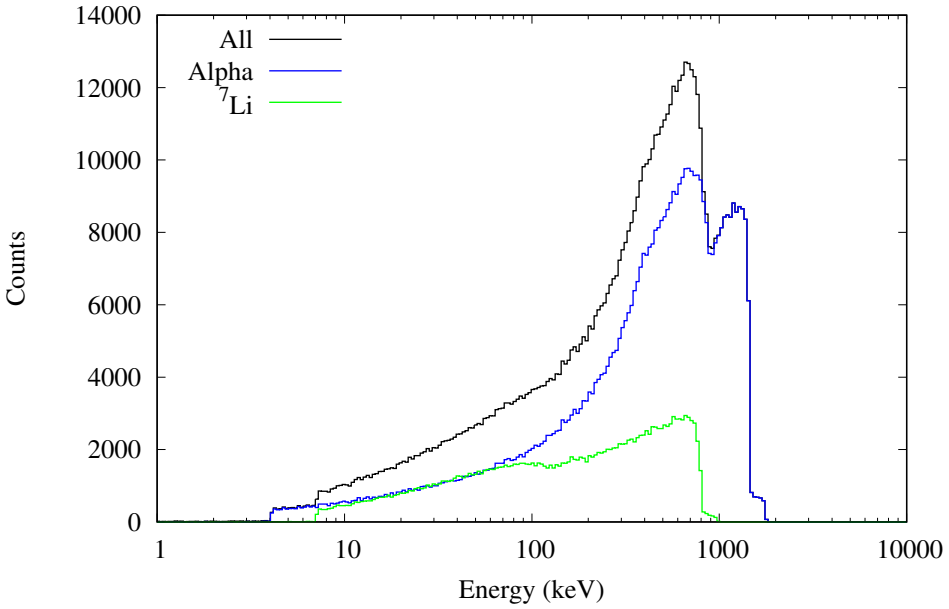

(a)

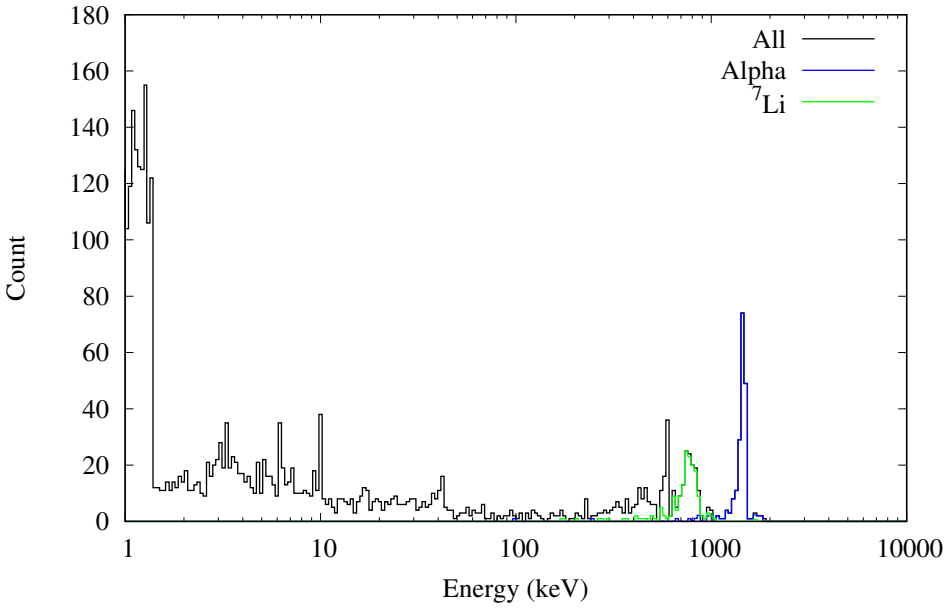

(b)

Figure 4.17: Energy deposit inside the sensitive volume of the SOI bridge using KUR mix mode (a) with B4C converter and (b) without converter.

Chapter 5

Investigation of the use of 3D mushroom microdosimeter for BNCT

5.1 Introduction

As mentioned in chapter 1, there are two main boron drugs used for BNCT, BSH and BPA. The main difference between the two drugs is how it is accumulated and distributed within a tumour cell. A graphical representation of the boron distribution inside a cell for boric acid, BSH and BPA are shown in figure 5.1. This shows that BSH compound has the tendency to accumulate around the cytoplasm of the cell, in contrast BPA accumulates inside the cytoplasm.

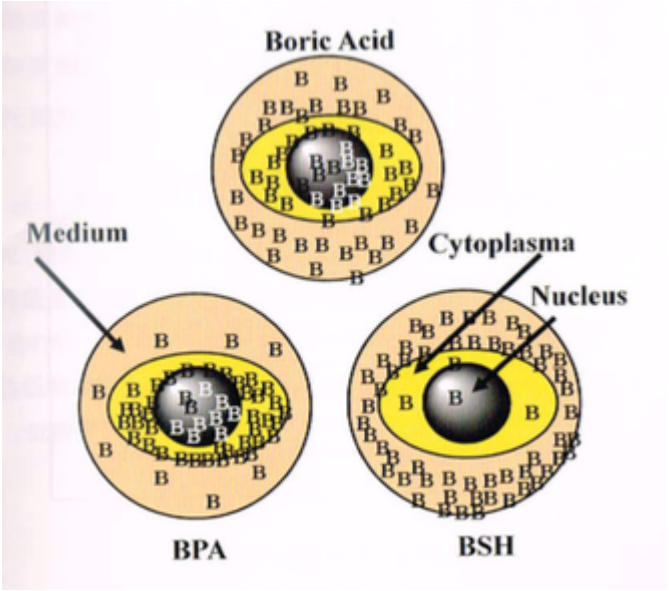

Figure 5.1: Graphical representation of the distribution of boron in a cell for different boron delivering compounds.

An area of interest is the determination of dose delivered to a cell from the boron dose (i.e. alpha and ^{7}Li ions). The previous chapters investigated the feasibility of the 3D bridge microdosimeter for BNCT dosimetry. The results showed that it can detect the particles generated from the boron capture reaction by using an external converter. There are few issues with an external converter, such as difficulty in manufacturing, but most importantly the reaction particles generated from the converter traverses through the over layers of the detector, losing energy and some particles come to a full stop inside the over layer material. The reaction particles generated from the p+ planar region located in the sensitive volume of the detector showed full energy deposition and more closely reflected the clinical situation in BNCT. However, the planar p+ region is only located superficially and across a small area. To closely simulate a cell with an uptake of boron, a larger p+ region that is directly in contact with the sensitive volume is desirable. The CMRP developed a new type of microdosimeter, called the 3D mushroom microdosimeter, which has these properties. Few authors have investigated the effect of different boron compounds for BNCT using Monte Carlo simulation [135, 136]. This chapter investigates the detector characterisation and its potential use for dose distribution inside a cell.

5.2 Material and method

5.2.1 Detector design

The 3D mushroom microdosimeter consisted of a 3D cylindrical sensitive volume with a n+ core produced by ion implantation. Each sensitive volume was surrounded with a complete p+ doped trench filled with polysilicon, shown in figure 5.2 and figure 5.3. The aluminium pads were used to increase the surface area to reduce metal line breakage which commonly occurred over the p+ trenches. PMMA material was placed on top of the oxide layer. Each individual sensitive volume was cylindrical in shape with a diameter and height of 10 μm. A total of 2500 individual sensitive volumes were connected in an array. The pitch between each individual sensitive volume was 40 μm to reduce cross talk between neighbouring row of detectors. For simplicity, the over layers and aluminium tracks were excluded from the image.

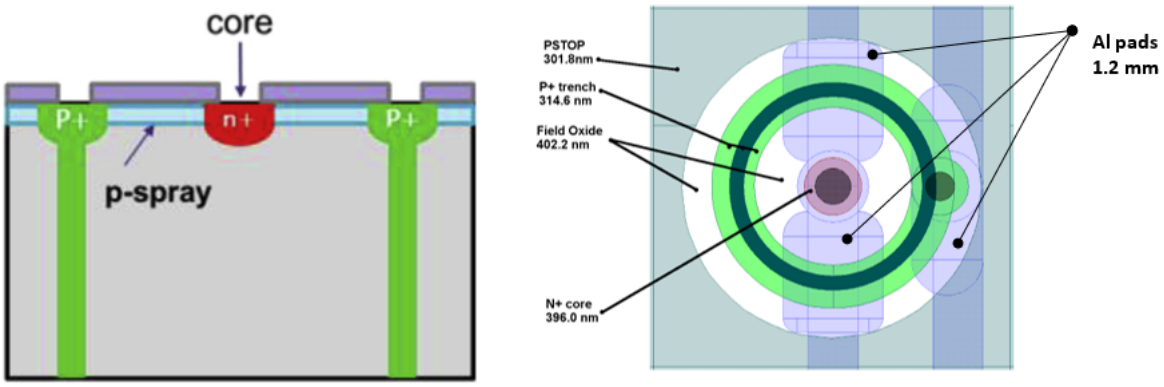

Figure 5.2: Cross sectional side and top view of the 3D mushroom microdosimeter configuration, indicating the Al pad thickness (1.2 mm) and thickness of the oxide layer over each region.

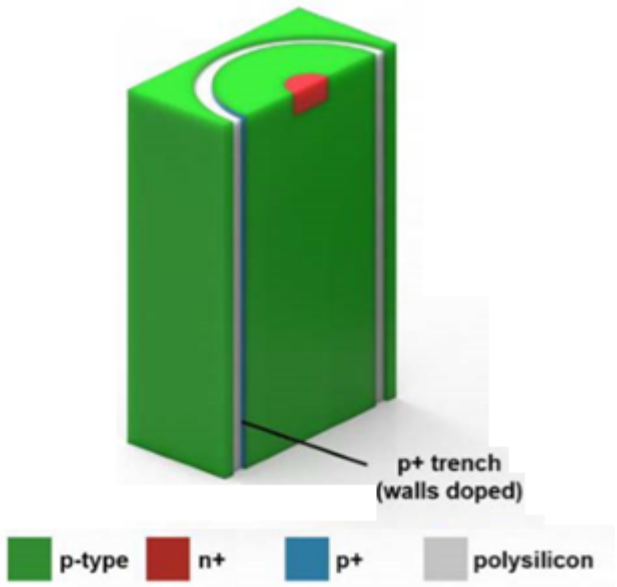

Figure 5.3: 3D schematic of the 3D mushroom microdosimeter.

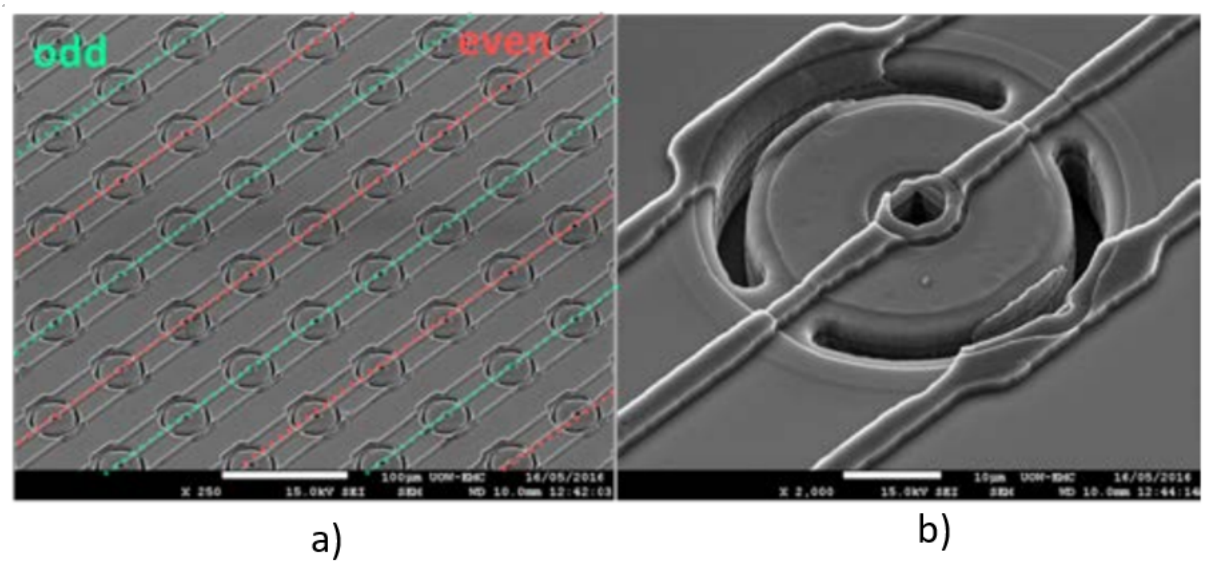

Figure 5.4: Scanning electron micrograph image of 3D mushroom microdosimeter a) Array of sensitive volume showing the odd and even rows. b) Single sensitive volume.

The literature review section of this thesis touched on various 3D detector manufactures and proposed approaches to 3D detector designs. The ability to create p+ columns going all the way through the sensitive volume of the detector has an interesting application in BNCT. A detector with a p+ column going through the centre of the sensitive volume crudely represents a cell with an uptake of BPA (fig-

ure 5.5). The current design of the p+ ring wrapped around the sensitive volume can be related to a cell with an uptake of BSH (figure 5.6).

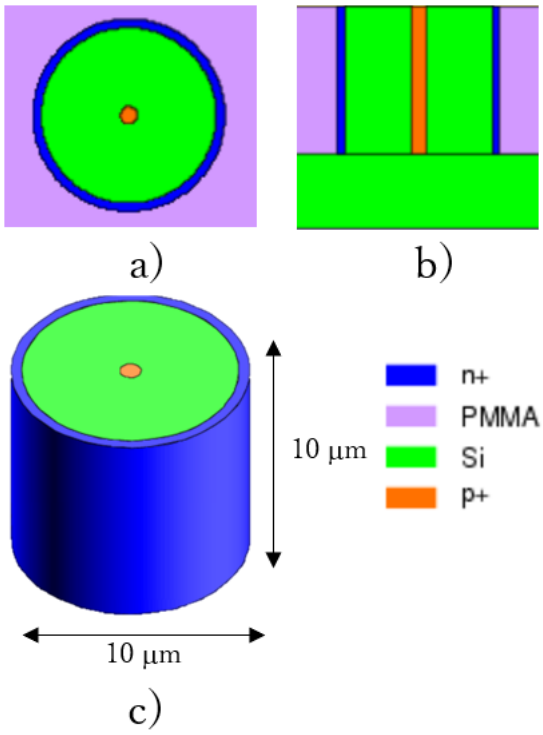

Figure 5.5: Modified 3D mushroom microdosimeter with p+ core through the centre of the sensitive volume. a) Cross sectional top view. b) Cross sectional side view. c) 3D geometry. The overlayers and aluminium tracks were excluded from the image for visual aid.

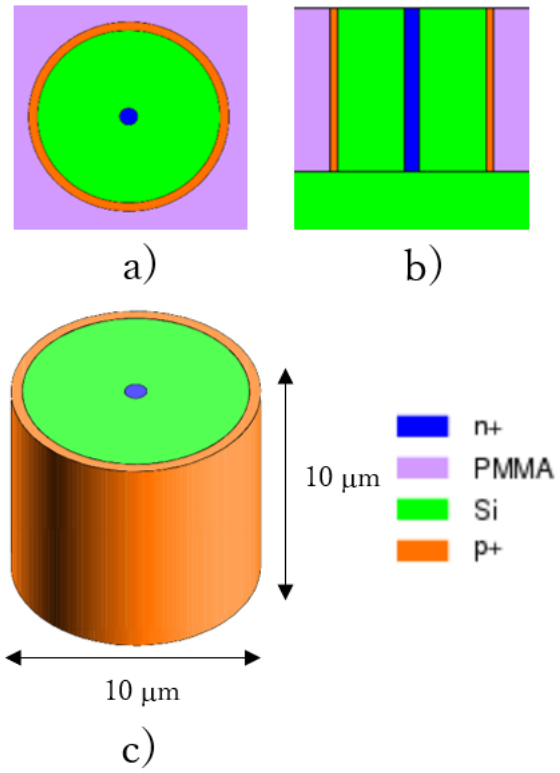

Figure 5.6: Modified 3D mushroom microdosimeter with p+ ring wrapped around the centre of the sensitive volume. a) Cross sectional top view. b) Cross sectional side view. c) 3D geometry. The over layers and aluminium tracks were excluded from the image for visual aid.

5.2.2 Alpha particle spectroscopy

Spectral characterisation was performed using an ^{241}Am source using the same experimental set up as described in chapter 4.

5.2.3 Charge collection study

The charge collection efficiency for the mushroom microdosimeter was measured using the IBICC technique with the ANTARES heavy ion microprobe at ANSTO, described earlier in chapter 4. A monoenergetic beam focused to a diameter of approximately 1 µm was raster scanned over the surface of the microdosimeter. A 24 MeV ^{12}C was used for this study.

5.2.4 Monte Carlo simulation

The detectors response under a neutron field used for BNCT was simulated using the Monte Carlo calculation code PHITS. The energy deposition inside the sensitive volume of the detector when irradiated by neutrons were calculated with and without a boron converter in place. The microdosimetric spectrum, *yd(y)*, was calculated from the energy deposition by dividing the deposited energy by the average chord length of the sensitive volume.

5.3 Results

5.3.1 Alpha particle spectroscopy

The energy of the ^{241}Am alpha particles deposited in the sensitive volume of the 3D mushroom microdosimeter is shown in figure 5.7. Using PHITS Monte Carlo simulation, the energy deposited inside the sensitive volume was calculated to be 1514 keV. The experimental result was 1481 keV which agreed with the simulation results within 3% uncertainty.

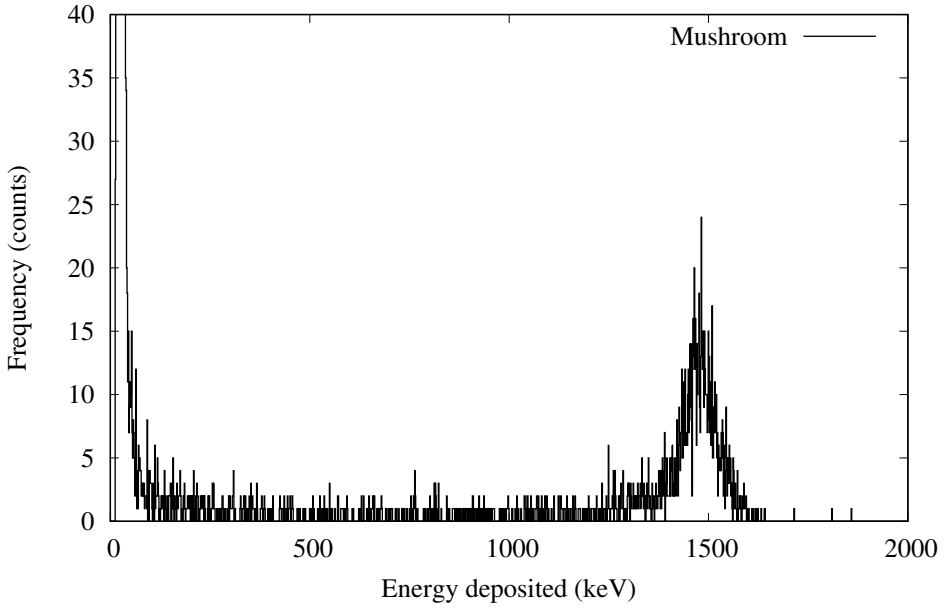

Figure 5.7: Alpha particle spectrum of ^{241}Am measured using the 3D mushroom microdosimeter.

5.3.2 Charge collection study

The energy spectrum of the 24 MeV ^{12}C ion measured using the 3D mushroom microdosimeter is shown in figure 5.8. The energy peak deposited in the 3D mushroom microdosimeter was approximately 9000 keV, which was very close to the expected energy deposition of 8872 keV from 24 MeV ^{12}C ions traversing through the over layers and 10 μm layer of silicon, calculated by PHITS, shown in figure 5.9. The median energy map at different bias applied to the detector are shown in figure 5.10.

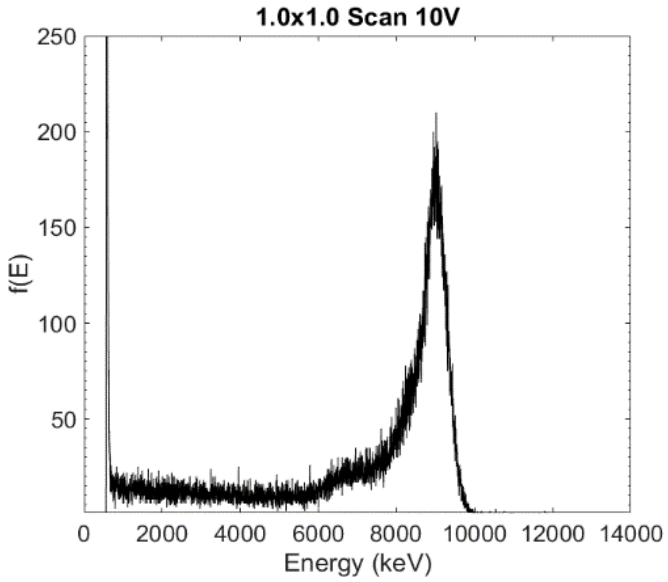

Figure 5.8: MCA spectrum a 24 MeV ^{12}C ion measured with the 3D mushroom microdosimeter at 10 V.

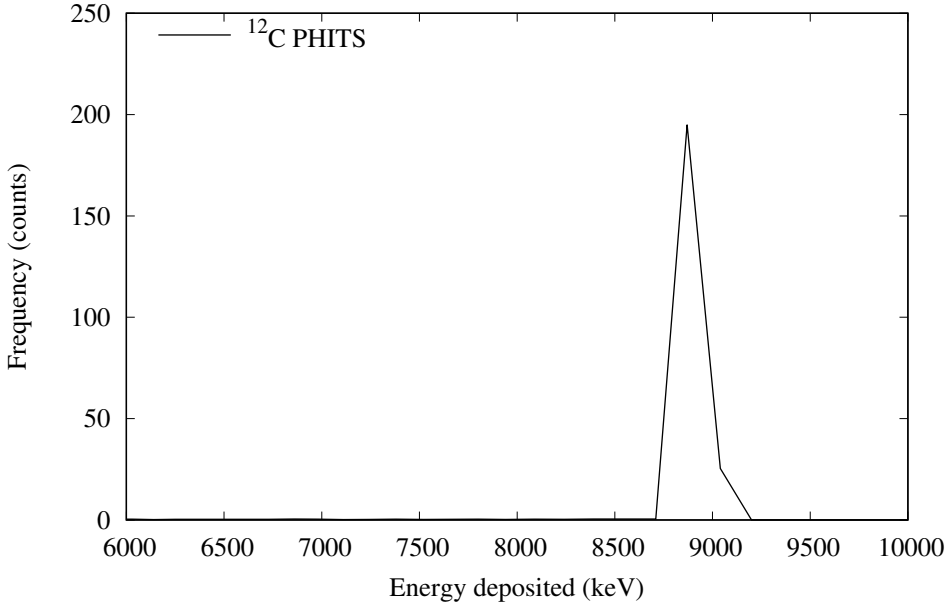

Figure 5.9: Simulated spectrum of 24 MeV ^{12}C ions deposited inside the sensitive volume of the 3D mushroom microdosimeter.

5.3.3 Monte Carlo simulation

5.3.3.1 Alpha particle

The ion track of 1.47 MeV alpha particles produced inside the p+ region is shown in figure 5.11. The left image show the tracks of alphas generated in the p+ core through the centre of the sensitive volume and the right shows the tracks of alphas generated in the p+ ring on the outside of the sensitive volume. It was found the total flux inside the sensitive volume was higher for the p+ core through the centre. This was because not all alphas entered the sensitive volume for the p+ ring design. The deposit energy inside the sensitive volume for both designs is shown in figure 5.12. The p+ core design was found to have higher number of counts compared to the p+ ring design.

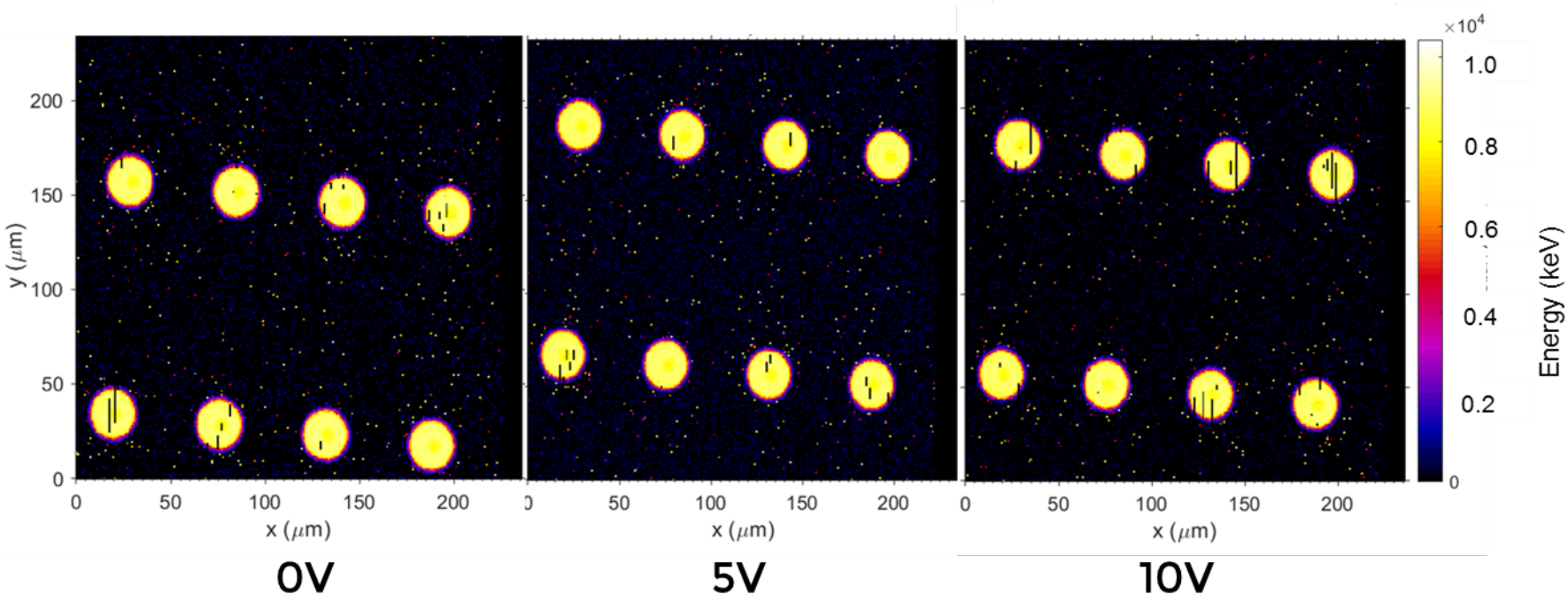

Figure 5.10: Median energy map of the 3D mushroom microdosimeter measured at 0, 5 and 10 V.

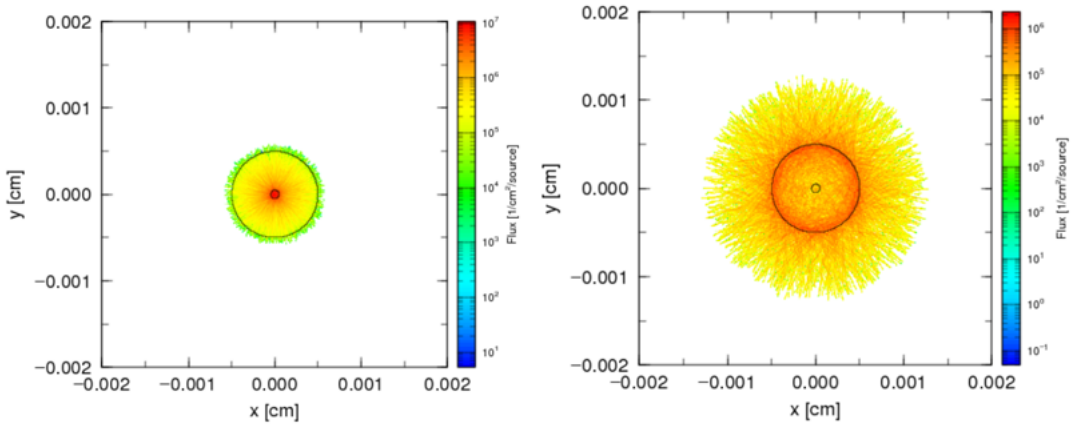

Figure 5.11: Ion track of 1.47 MeV alpha particles inside a single sensitive volume. Left) p+ core through the centre of the sensitive volume. Right) p+ ring on the outside of sensitive volume.

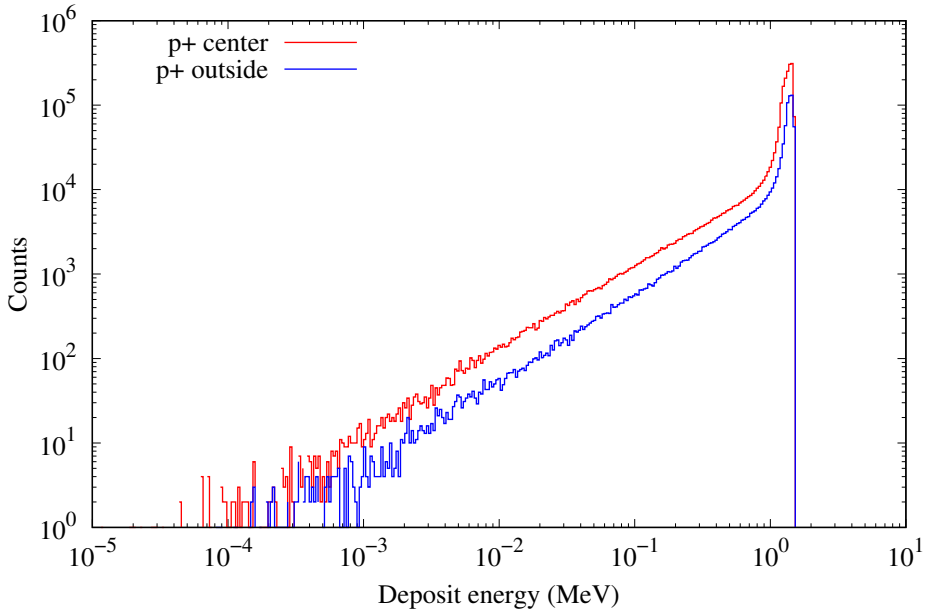

Figure 5.12: Deposit energy of 1.47 MeV alpha particles inside the sensitive volume for p+ core (red) and p+ ring (blue).

Table 5.1: Dose delivered from alpha particles to the sensitive volume and surrounding material for both detector type

	Dose delivered (Gy/n)	
Detector type	Sensitive volume	Surrounding PMMA
P+ core	9.8×10^{-2}	2.5×10^{-7}
P+ ring	3.9×10^{-2}	3.9×10^{-3}

5.3.3.2 Lithium ions

The ion track of 840 keV ^{7}Li particles produced inside the p+ region is shown in figure 5.13. The left image show the tracks of ^{7}Li ions generated in the p+ core through the centre of the sensitive volume and the right image shows the tracks of ^{7}Li ions generated in the p+ ring on the outside of the sensitive volume. Similarly, with the alpha particles, higher number of ^{7}Li ions were deposited inside the sensitive volume for the p+ core design. The range of 840 keV ^{7}Li ions inside silicon is 2.46 μm, so all the ^{7}Li ions generated stopped inside the sensitive volume. The deposit energy inside the sensitive volume for both detector design are shown in figure 5.14. The p+ core design was found to have higher number of counts compared to the p+ ring design.

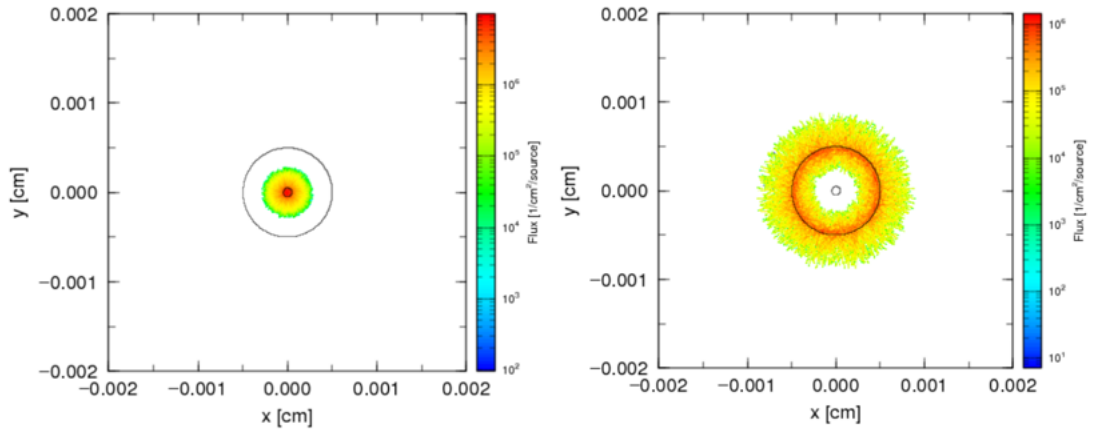

Figure 5.13: Ion track of 840 keV ^{7}Li particles inside a single sensitive volume. Left) p+ core through the centre of the sensitive volume. Right) p+ ring on the outside of sensitive volume.

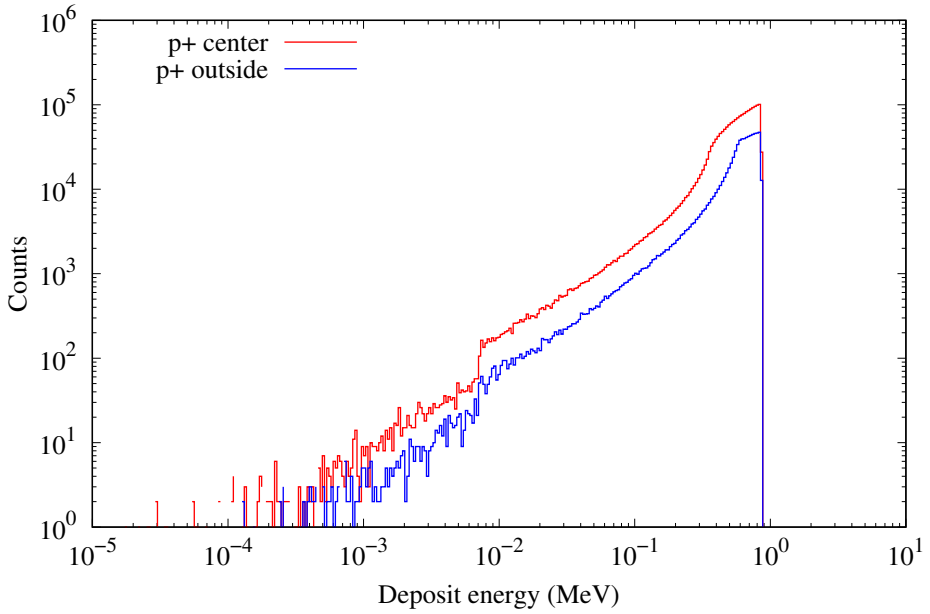

Figure 5.14: Deposit energy of 840 keV ^{7}Li particles inside the sensitive volume for p+ core (red) and p+ ring (blue).

Table 5.2: Dose delivered from ^{7}Li particles to the sensitive volume and surrounding material for both detector type

	Dose delivered (Gy/n)	
Detector type	Sensitive volume	Surrounding PMMA
P+ core	4.5×10^{-2}	0
P+ ring	1.9×10^{-2}	1.7×10^{-3}

5.3.4 Neutron irradiation

The deposit energy spectrum obtained with the p+ core and p+ ring detector when irradiated by KUR mix irradiation mode are shown in figure 5.15 and figure 5.16, respectively. Higher events were observed with the p+ ring detector, due to the larger surface area of the p+ region. The main component was the 1.47 MeV alpha particle, followed by the 840 keV ^{7}Li ion, red and blue line respectively. Small amount of recoil silicon was calculated, however, compared to the 3D bridge microdosimeter (chapter 4 and 5) the amount was much smaller due to the smaller volume of the detector and replacing the surrounding silicon with PMMA. The energy deposited of the p+ core detector with a 5 μm thick B4C converter placed on top on the detector (similar set up to chapter 4 and 5) is shown in figure 5.17. A broad spectrum was obtained with the B4C converter in place. This is because the reaction particles that are generated in the converter will travel through the over layers (aluminium tracks and silicon oxide) through various angles, thus creating a broad energy spectrum. The total number of events was the highest with the converter in place. The total deposit energy for each detector configuration, normalised to the max (i.e. alpha peak) is shown in figure 5.18. The low energy events below 10 keV were primarily recoil silicon events. These events were prominent for p+ core calculation, purely because the number of alpha events were low. As the number of alpha events increased, the ratio of alpha events to recoil silicon increased and the recoil silicon

events become small in comparison. The microdosimetric *yd(y)* distribution of each detector configuration is shown in figure 5.19 The p+ core without the converter was found to have the highest lineal energy distribution, with a peak at approximately 290 keV/μm. This value is close to the expected value of 270 keV/μm. The p+ ring detector and p+ core with converter configuration showed a similar distribution with a peak at approximately 210 keV/μm.

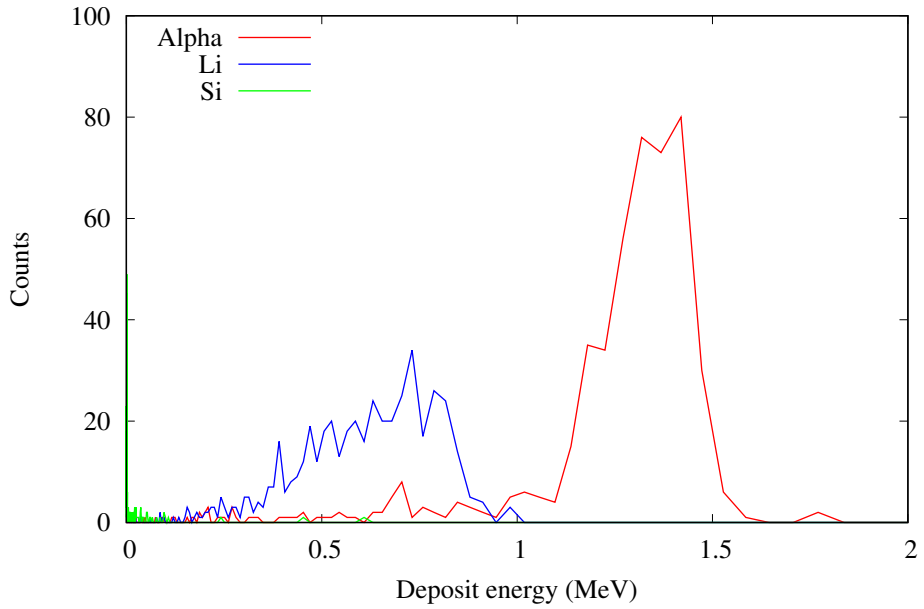

Figure 5.15: Deposit energy spectrum obtained from the p+ core detector when irradiated with KUR mix irradiation mode.

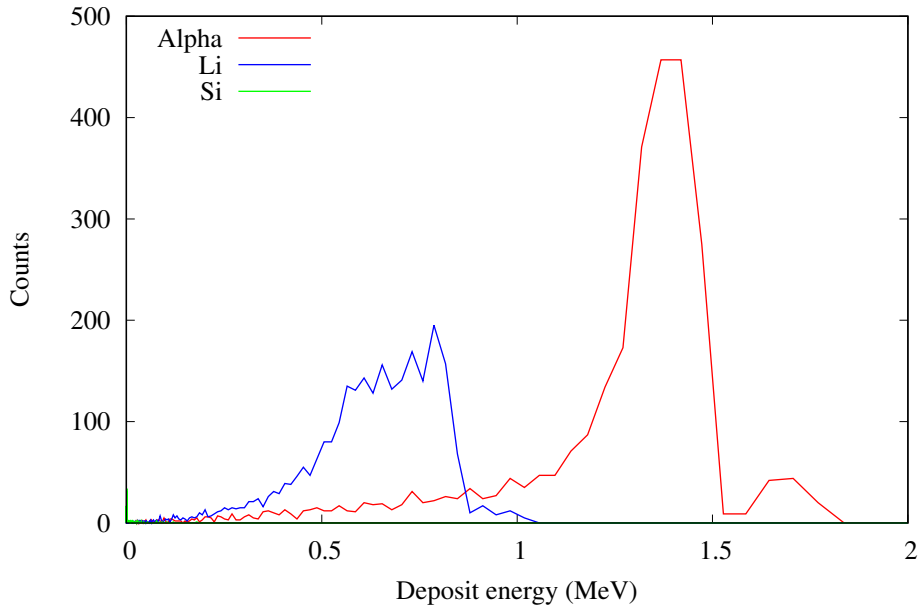

Figure 5.16: Deposit energy spectrum obtained from the p+ ring detector when irradiated with KUR mix irradiation mode.

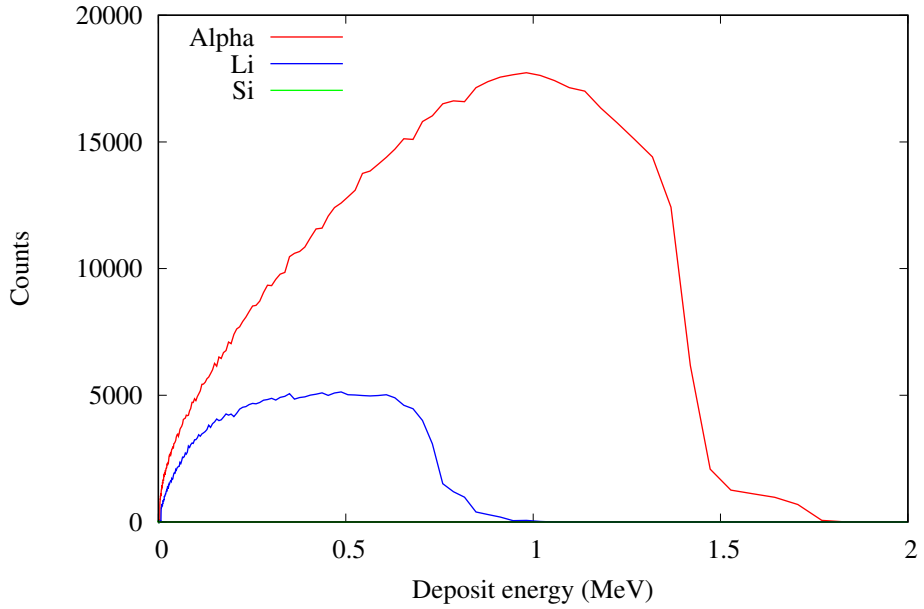

Figure 5.17: Deposit energy spectrum obtained from the p+ core detector with 5 μm thick B4C converter placed above when irradiated with KUR mix irradiation mode.

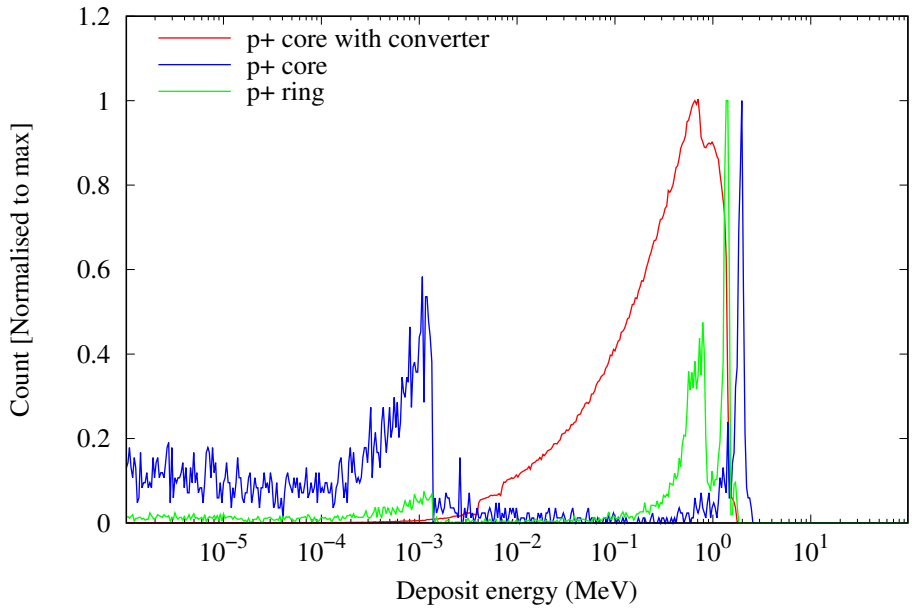

Figure 5.18: Total deposit energy of each detector configuration. Each spectrum was normalised to peak for visual comparison.

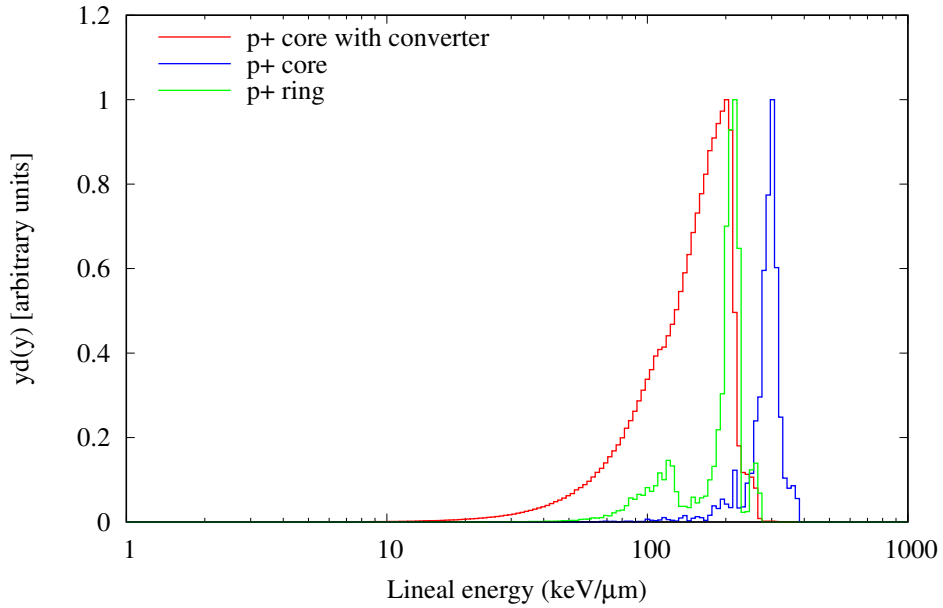

Figure 5.19: Microdosimetric *yd(y)* spectrum of each detector configuration. Each spectrum was normalised to peak for visual comparison.

5.4 Discussion and conclusion

Monte Carlo simulation was performed using PHITS to investigate the feasibility of a concept design detector, based on the 3D mushroom microdosimeter, for BNCT application. Two designs were investigated, a p+ core running through the centre of the sensitive volume (simulating a cell with BPA uptake) and a p+ ring wrapped around the sensitive volume of the detector (simulating a cell with BSH uptake). The distribution inside the sensitive volume was calculated by simulating a single detector and setting the source to the BNCT reaction particles, 1.47 MeV alpha particle and 840 keV ^{7}Li ions. In both cases, for the same number of particles, the p+ core detector measured a higher number of events, which led to higher dose inside the sensitive volume. The dose to the surrounding material (PMMA) was higher with the p+ ring detector. This is an important to result, since the aim of radiotherapy is to deliver dose to the tumour region and spare dose to the normal tissue. A boron compound which accumulates to the cytoplasm (or to the nucleus itself) will deliver high dose to the nucleus and minimal dose to the surrounding cells. The idea is for this detector to simulate this situation and can measure the effect of change in boron concentration and distribution it has on the delivered dose. The *yd(y)* microdosimetric distribution also indicated the p+ core design detector had the highest lineal energy distribution. This is because almost all alpha particles generated in the p+ core were crossers and deposited the largest amount of energy inside the sensitive volume, compared to the other two configurations. The PHITS Monte Carlo simulation showed the p+ core detector would be suitable for BNCT dosimetry application. By using the p+ ring detector in conjunction, a comparison between the dose delivered to the sensitive volume with differing boron distributions can be made. Also, by changing the boron doping concentration in the p+ region, the effect of dose on boron concentration can be measured.

Chapter 6

Summary and conclusion

This thesis investigated the use of two types of radiation detectors; a tissue equivalent proportional counter and a silicon semiconductor detector for use in BNCT field to measure and determine the beam quality of a neutron field and its potential use for quality assurance of BNCT. These detectors are capable of measuring microdosimetric quantities, which is important in determining the biological effect of radiation. particularly useful in a mixed radiation environment. A summary of the conclusion of chapter 3 through to 5 are shown below.

Chapter 3: Investigation of the use of tissue equivalent proportional counters for microdosimetry in BNCT Two types of proportional counter were used in this chapter; a tissue equivalent proportional counter and a graphite walled proportional counter. The response of the proportional counters in a neutron field was examined using a ^{252}Cf source. The proton edge and high LET components were detected using the ^{252}Cf source. However, the electronic noise in the system was high and the electron events from the gamma rays could not be accurately identified. The graphite walled proportional counter was able to detect events down to approximately 1 keV/μm. The graphite walled proportional counter was used to measure the gamma ray component of the ^{252}Cf source. A good agreement between experimental and simulated results were found. A longer irradiation time for the graphite walled proportional counter was required to increase the statistics. Once the TEPC detector system was tested with the ^{252}Cf source, the beam quality of various neutron

sources that are utilised for BNCT was measured.

The three neutron sources used were (i) KUR epithermal irradiation mode, (ii) KUR mixed irradiation mode, and (iii) QSC accelerator-based neutron source. The mixed irradiation mode has a larger component of thermal neutrons compared to the epithermal irradiation mode. This resulted in a higher number of proton events detected with the mixed irradiation mode, due to the $^{14}N(n,p)^{14}C$ reaction. The accelerator-based neutron source has a similar spectrum to the KUR mixed irradiation mode. The measured microdosimetric distribution were similar in shape, however, the *yd(y)* distribution of the accelerator-based neutron source had a larger proton event. This was due to the higher number of fast neutrons present in the accelerator-based neutron source. Similar RBE values between the three neutron sources (KUR mixed, KUR epithermal mode and accelerator-based neutron source) were obtained. The results showed that the TEPC can be used to measure single event microdosimetric quantities and the RBE can be derived from the *yd(y)* distribution.

Chapter 4: Investigation of the use of 3D bridge silicon on insulator microdosimeter for BNCT. The previous chapter demonstrated the TEPC was capable of measuring microdosimetric single event spectra and the RBE of the neutron field was successfully measured. However, the TEPC can only mimic a single cell and adding boron inside the TEPC cavity is difficult. These limitations motivated the CMRP at the UOW to develop the 3D bridge SOI microdosimeter. It consists of an array of micron sized sensitive volumes that mimic an array of biological cells. The detector characterisation was performed at the detector lab in ANSTO. Alpha particle spectroscopy and charge collection studies were performed to measure the response of the detector to alpha radiation. Following the detector characterisation, the detectors response to BNCT irradiation field, with and without a boron converter, was simulated using PHITS. The optimal B4C converter thickness was found to be 5 μm. To accurately measure the lineal energy distribution, the particles must traverse all the way through the sensitive volume of the detector (i.e. crossers).

The current design of 10 μm thick sensitive volume was found to be too thick for the alpha and ^{7}Li ions. A detector with a thinner sensitive volume was found to be necessary to accurately measure the lineal energy distribution. To increase the number of crossers going through the sensitive volume of the detector, a thinner 2 μm thick 3D bridge SOI microdosimeter was designed and tested using PHITS. It was found that the number of crossers increased and lineal energy distribution shifted closer to the expected value. However, the number of particles that came to a full stop inside the sensitive volume was still high. This was because the lateral dimension of the detector was still larger than the range of the particles of interest. An ideal detector to measure accurate lineal energy distribution was found to have small dimensions in all directions.

Chapter 5: Investigation of the use of 3D mushroom microdosimeter for microdosimetry in BNCT. The 3D bridge SOI microdosimeter had the limitation of only being able to pattern the silicon 1 – 2 μm below the surface. This created a non-uniform charge collection inside the sensitive volume. To overcome this issue, the CMRP developed an optimal SOI microdosimeter called the mushroom with 3D sensitive volumes embedded in PMMA using 3D active edge detector technology. The charge collection characterisation of this new detector was performed using the IBICC system at ANSTO. The results showed an excellent response of the mushroom detector and full charge collection within the sensitive volume of the detector was observed. Following on from this result, two configurations of the mushroom microdosimeter was designed and tested using PHITS. The detector configuration simulated the two main boron compounds used in BNCT, BSH and BPA. A p+ ring wrapped around the sensitive volume of the detector simulated a cell with BSH uptake and a p+ core through the middle of the sensitive volume simulated a cell with BPA uptake. The response of both detector types under a BNCT field was evaluated. It was found that the lineal energy distribution of the alpha particle was very close to the expected value. Calculation showed a higher dose detected inside the sensitive volume for the BPA type detector. By adjusting the boron concentration

inside the p+ region to clinically utilised values, the dose from the boron component can be measured and it may be possible to calculate the CBE factors. The beam quality of various neutron sources for BNCT were measured using the proportional counter and verified against Monte Carlo simulation. The RBE was calculated and similar values were obtained compared to clinically utilised values and other reported work. Silicon microdosimeter characterisation work showed fully functioning arrays of individual micron sized sensitive volumes and Monte Carlo simulation showed its potential use for BNCT dosimetry. The PHITS Monte Carlo simulation was compared against measured data across various conditions and showed good results.

Future work

To perform measurements using the 3D bridge SOI microdosimeter and mushroom microdosimeter using a BNCT neutron source to validate the simulation results. Using the current fabrication technology, the SOI microdosimeters have the advantage of being able to implant boron into the sensitive volume of the detector, as well as adjusting the doping concentration. This would allow a detector, having a similar dimension to a human cell, the capability of measuring the effect of boron distribution inside a cell. This would provide new information to the clinicians and ultimately benefit the patients receiving BNCT.

Bibliography

[1] D. Brown, M. Chadwick, R. Capote, A. Kahler, A. Trkov, M. Herman, A. Sonzogni, Y. Danon, A. Carlson, M. Dunn, D. Smith, G. Hale, G. Arbanas, R. Arcilla, C. Bates, B. Beck, B. Becker, F. Brown, R. Casperson, J. Conlin, D. Cullen, M.-A. Descalle, R. Firestone, T. Gaines, K. Guber, A. Hawari, J. Holmes, T. Johnson, T. Kawano, B. Kiedrowski, A. Koning, S. Kopecky, L. Leal, J. Lestone, C. Lubitz, J. Márquez Damián, C. Mattoon, E. McCutchan, S. Mughabghab, P. Navratil, D. Neudecker, G. Nobre, G. Noguere, M. Paris, M. Pigni, A. Plompen, B. Pritychenko, V. Pronyaev, D. Roubtsov, D. Rochman, P. Romano, P. Schillebeeckx, S. Simakov, M. Sin, I. Sirakov, B. Sleaford, V. Sobes, E. Soukhovitskii, I. Stetcu, P. Talou, I. Thompson, S. van der Marck, L. Welser-Sherrill, D. Wiarda, M. White, J. Wormald, R. Wright, M. Zerkle, G. Žerovnik, and Y. Zhu, "ENDF/B-VIII.0: The 8 th Major Release of the Nuclear Reaction Data Library with CIELO-project Cross Sections, New Standards and Thermal Scattering Data," *Nuclear Data Sheets*, vol. 148, pp. 1–142, feb 2018. [Online]. Available: https://linkinghub.elsevier.com/retrieve/pii/S0090375218300206

[2] JSNCT, "A neutron source for BNCT." [Online]. Available: http://www.jsnct.jp/e/about{_}nct/gen.html

[3] P. D. Bradley and a. B. Rosenfeld, "Tissue equivalence correction for silicon microdosimetry detectors in boron neutron capture therapy." *Medical physics*, vol. 25, no. 11, pp. 2220–5, 1998. [Online]. Available: http://www.ncbi.nlm.nih.gov/pubmed/9829249

[4] P. Bradley, A. Rosenfeld, and M. Zaider, "Solid state microdosimetry," *Nuclear Instruments and Methods in Physics Research Section B: Beam Interactions with Materials and Atoms*, vol. 184, no. 1-2, pp. 135–157, sep 2001. [Online]. Available: http://linkinghub.elsevier.com/retrieve/pii/S0168583X01007157

[5] W. H. Lim, A. L. Ziebell, I. Cornelius, M. I. Reinhard, D. A. Prokopovich, A. S. Dzurak, and A. B. Rosenfeld, "Cylindrical silicon-on-insulator microdosimeter: Design, fabrication and TCAD modeling," *IEEE Transactions on Nuclear Science*, vol. 56, no. 2, pp. 424–428, 2009.

[6] J. Livingstone, D. A. Prokopovich, M. L. F. Lerch, M. Petasecca, M. I. Reinhard, H. Yasuda, M. Zaider, J. F. Ziegler, V. L. Pisacane, J. F. Dicello, V. L. Perevertaylo, and A. B. Rosenfeld, "Large area silicon microdosimeter for dosimetry in high LET space radiation fields: Charge collection study," *IEEE Transactions on Nuclear Science*, vol. 59, no. 6, pp. 3126–3132, 2012.

[7] A. B. Rosenfeld, "Novel detectors for silicon based microdosimetry, their concepts and applications," *Nuclear Instruments and Methods in Physics Research, Section A: Accelerators, Spectrometers, Detectors and Associated Equipment*, vol. 809, pp. 156–170, 2016. [Online]. Available: http://dx.doi.org/10.1016/j.nima.2015.08.059

[8] C. Da Via, M. Boscardin, G. F. Dalla Betta, G. Darbo, C. Fleta, C. Gemme, P. Grenier, S. Grinstein, T. E. Hansen, J. Hasi, C. Kenney, A. Kok, S. Parker, G. Pellegrini, E. Vianello, and N. Zorzi, "3D silicon sensors: Design, large area production and quality assurance for the ATLAS IBL pixel detector upgrade," *Nuclear Instruments and Methods in Physics Research, Section A: Accelerators, Spectrometers, Detectors and Associated Equipment*, vol. 694, pp. 321–330, 2012. [Online]. Available: http://dx.doi.org/10.1016/j.nima.2012.07.058

[9] E. D. Podgorsak and International Atomic Energy Agency., *Radiation oncology physics : a handbook for teachers and students.* International

Atomic Energy Agency, 2005. [Online]. Available: https://inis.iaea.org/search/search.aspx?orig{_}q=RN:36071456

[10] E. &. Ziegler, "Product Information," in *Industrial Radiation Sources*. Valencia, CA: Isotope Products, 2008, p. 18.

[11] R. S. Caswell, "Deposition of Energy by Neutrons in Spherical Cavities," *Radiation Research*, vol. 27, no. 1, pp. 92–107, jan 1966. [Online]. Available: https://www.jstor.org/stable/3571818?origin=crossref

[12] A. J. Kreiner, J. Bergueiro, D. Cartelli, M. Baldo, W. Castell, J. G. Asoia, J. Padulo, J. C. Suárez Sandín, M. Igarzabal, J. Erhardt, D. Mercuri, A. A. Valda, D. M. Minsky, M. E. Debray, H. R. Somacal, M. E. Capoulat, M. S. Herrera, M. F. del Grosso, L. Gagetti, M. S. Anzorena, N. Canepa, N. Real, M. Gun, and H. Tacca, "Present status of Accelerator-Based BNCT," *Reports of Practical Oncology & Radiotherapy*, vol. 21, no. 2, pp. 95–101, mar 2016.

[13] B. W. Stewart and C. P. Wild, "World cancer report 2014," *World Health Organization*, pp. 1–2, 2014. [Online]. Available: http://www.videnza.org/wp-content/uploads/World-Cancer-Report-2014.pdf

[14] The Editorial Board of the Cancer Statistics in Japan, "Cancer Statistics in Japan 2017," 2017.

[15] National Institutes of Health, "Types of Cancer Treatment," 2017. [Online]. Available: https://www.cancer.gov/about-cancer/treatment/types

[16] M. B. Barton, M. Frommer, and J. Shafiq, "Role of radiotherapy in cancer control in low-income and middle-income countries," *The Lancet Oncology*, vol. 7, no. 7, pp. 584–595, jul 2006. [Online]. Available: http://linkinghub.elsevier.com/retrieve/pii/S1470204506707598

[17] S. Tyldesley, G. Delaney, F. Foroudi, L. Barbera, M. Kerba, and W. Mackillop, "Estimating the Need for Radiotherapy for Patients

With Prostate, Breast, and Lung Cancers: Verification of Model Estimates of Need With Radiotherapy Utilization Data From British Columbia," *International Journal of Radiation Oncology*Biology*Physics*, vol. 79, no. 5, pp. 1507–1515, apr 2011. [Online]. Available: http://linkinghub.elsevier.com/retrieve/pii/S036030161000026X

[18] M. B. Barton, S. Jacob, J. Shafiq, K. Wong, S. R. Thompson, T. P. Hanna, and G. P. Delaney, "Estimating the demand for radiotherapy from the evidence: A review of changes from 2003 to 2012," *Radiotherapy and Oncology*, vol. 112, no. 1, pp. 140–144, jul 2014. [Online]. Available: http://linkinghub.elsevier.com/retrieve/pii/S0167814014001698

[19] G. Locher, "Biological effects and therapeutic possibilities of neutrons." *American Journal of Roentgenology, Radium Therapy*, vol. 36, pp. 1–13, 1936.

[20] W. A. G. Sauerwein, P. M. Bet, and A. Wittig, "Drugs for BNCT: BSH and BPA," in *Neutron Capture Therapy*. Berlin, Heidelberg: Springer Berlin Heidelberg, 2012, pp. 117–160. [Online]. Available: http://link.springer.com/10.1007/978-3-642-31334-9{_}8

[21] K. Hanaoka, T. Watabe, S. Naka, Y. Kanai, H. Ikeda, G. Horitsugi, H. Kato, K. Isohashi, E. Shimosegawa, and J. Hatazawa, "FBPA PET in boron neutron capture therapy for cancer: prediction of 10B concentration in the tumor and normal tissue in a rat xenograft model," *EJNMMI Research*, vol. 4, no. 1, p. 70, dec 2014. [Online]. Available: http://www.ejnmmires.com/content/4/1/70

[22] L. E. FARR, W. H. SWEET, J. S. ROBERTSON, C. G. FOSTER, H. B. LOCKSLEY, D. L. SUTHERLAND, M. L. MENDELSOHN, and E. E. STICKLEY, "Neutron capture therapy with boron in the treatment of glioblastoma multiforme." *The American journal of roentgenology, radium therapy, and nuclear medicine*, vol. 71, no. 2, pp. 279–93, feb 1954. [Online]. Available: http://www.ncbi.nlm.nih.gov/pubmed/13124616

[23] D. N. Slatkin, "A history of boron neutron capture therapy of brain tumours. Postulation of a brain radiation dose tolerance limit." *Brain : a journal of neurology*, vol. 114, pp. 1609–29, aug 1991. [Online]. Available: http://www.ncbi.nlm.nih.gov/pubmed/1884169

[24] H. Hatanaka and K. Sano, "A revised boron-neutron capture therapy for malignant brain tumours," *Zeitschrift fur Neurologie*, vol. 204, no. 4, pp. 309–332, 1973. [Online]. Available: http://link.springer.com/10.1007/BF00316011

[25] H. Hatanaka, "Boron-Neutron Capture Therapy for Tumors," in *Glioma*. Berlin, Heidelberg: Springer Berlin Heidelberg, 1991, pp. 233–249. [Online]. Available: http://www.springerlink.com/index/10.1007/978-3-642-84127-9{_}18

[26] H. Hatanaka, K. Amano, S. Kamano, H. Fankhauser, T. Hanamura, and K. Sano, "Boron-neutron capture therapy in relation to immunotherapy," *Acta Neurochirurgica*, vol. 42, no. 1-2, pp. 57–72, mar 1978. [Online]. Available: http://link.springer.com/10.1007/BF01406631

[27] K. Kanda, T. Kobayashi, K. Akuta, and K. Ono, "Experiences of BNCT Using the KUR," in *Advances in Neutron Capture Therapy*. Boston, MA: Springer US, 1993, pp. 683–687. [Online]. Available: http://link.springer.com/10.1007/978-1-4615-2978-1{_}136

[28] O. AIZAWA, K. KANDA, T. NOZAKI, and T. MATSUMOTO, "Remodeling and Dosimetry on the Neutron-Irradiation Facility of the Musashi-Institute-Of-Technology Reactor for Boron Neutron-Capture Therapy," *Nuclear Technology*, vol. 48, no. 2, pp. 150–163, 1980.

[29] K. Yokoo, Y. Torii, and K. Koibuchi, "Measurement of thermal neutron flux for BNCT in JRR-2," 1994. [Online]. Available: https://inis.iaea.org/search/search.aspx?orig{_}q=RN:25073353

[30] A. Brahme, *Comprehensive Biomedical Physics*. Newnes, 2014. [Online]. Available: https://books.google.co.jp/books?id=9RR0AwAAQBAJ

[31] R. M. Brugger and W. H. Herleth, "Intermediate energy neutron beams from the MURR." *Basic life sciences*, vol. 54, pp. 153–66, 1990. [Online]. Available: http://www.ncbi.nlm.nih.gov/pubmed/2268237

[32] H. B. Liu, R. M. Brugger, and D. C. Rorer, "Enhancement of the Epithermal Neutron Beam at the Brookhaven Medical Research Reactor," in *Advances in Neutron Capture Therapy*. Boston, MA: Springer US, 1993, pp. 75–79. [Online]. Available: http://link.springer.com/10.1007/978-1-4615-2978-1{_}15

[33] R. D. Rogus, O. K. Harling, and J. C. Yanch, "Mixed field dosimetry of epithermal neutron beams for boron neutron capture therapy at the MITR-II research reactor," *Medical Physics*, vol. 21, no. 10, pp. 1611–1625, oct 1994. [Online]. Available: http://doi.wiley.com/10.1118/1.597267

[34] T. Kobayashi, Y. Kanda, Y. Fujita, Y. Sakurai, and K. Ono, "The Upgrade of the Heavy Water Facility of Kyoto University Reactor for Neutron Capture Therapy," in *Advances in Neutron Capture Therapy*, B. Larsson, J. Crawford, and R. Weinreich, Eds., Amsterdam, 1997, pp. 321–325.

[35] K. Yokoo, T. Yamada, F. Sakurai, T. Nakajima, N. Ohhashi, and H. Izumo, "A new medical irradiation facility at JRR-4," *Advances in Neutron Capture Therapy*, vol. 1, pp. 326–330, 1997.

[36] A. Matsumura, Y. Shibata, T. Yamamoto, S. Takano, Y. Hayakawa, K. Nakai, Y. Nakagawa, F. Sakurai, Y. Torii, K. Yokoo, H. Kumada, T. Kishi, K. Yamamoto, Y. Akine, and T. Nose, "Clinical Protocol Using New Neutron Irradiation Facility (JRR4) at JAERI," in *Frontiers in Neutron Capture Therapy*. Boston, MA: Springer US, 2001, pp. 283–287. [Online]. Available: http://link.springer.com/10.1007/978-1-4615-1285-1{_}38

[37] Y. Nakagawa, "Boron Neutron Capture Therapy," in *Frontiers in Neutron Capture Therapy*. Boston, MA: Springer US, 2001, pp. 73–79. [Online]. Available: http://link.springer.com/10.1007/978-1-4615-1285-1{_}6

[38] S. Kawabata, S.-I. Miyatake, Y. Kajimoto, Y. Kuroda, T. Kuroiwa, Y. Imahori, M. Kirihata, Y. Sakurai, T. Kobayashi, and K. Ono, "The early successful treatment of glioblastoma patients with modified boron neutron capture therapy. Report of two cases." *Journal of neuro-oncology*, vol. 65, no. 2, pp. 159–65, nov 2003. [Online]. Available: http://www.ncbi.nlm.nih.gov/pubmed/14686736

[39] I. Kato, K. Ono, Y. Sakurai, M. Ohmae, A. Maruhashi, Y. Imahori, M. Kirihata, M. Nakazawa, and Y. Yura, "Effectiveness of BNCT for recurrent head and neck malignancies," *Applied Radiation and Isotopes*, vol. 61, no. 5, pp. 1069–1073, nov 2004. [Online]. Available: http://linkinghub.elsevier.com/retrieve/pii/S0969804304002672

[40] T. Aihara, J. Hiratsuka, S. Nishiike, N. Morita, M. Uno, T. Harada, Y. Sakurai, A. Maruhashi, and K. Ono, "Using BPA alone for boron neutron capture therapy of recurrent head and neck malignancies." [Online]. Available: https://inis.iaea.org/search/search.aspx?orig{_}q=RN:39030680

[41] M. Suzuki, Y. Sakurai, S. Masunaga, Y. Kinashi, K. Nagata, A. Maruhashi, and K. Ono, "Feasibility of boron neutron capture therapy (BNCT) for malignant pleural mesothelioma from a viewpoint of dose distribution analysis," *International Journal of Radiation Oncology*Biology*Physics*, vol. 66, no. 5, pp. 1584–1589, dec 2006. [Online]. Available: http://linkinghub.elsevier.com/retrieve/pii/S0360301606027751

[42] M. Suzuki, Y. Sakurai, S. Hagiwara, S. Masunaga, Y. Kinashi, K. Nagata, A. Maruhashi, M. Kudo, and K. Ono, "First Attempt of Boron Neutron Capture Therapy (BNCT) for Hepatocellular Carcinoma," *Japanese*

Journal of Clinical Oncology, vol. 37, no. 5, pp. 376–381, may 2007. [Online]. Available: http://academic.oup.com/jjco/article/37/5/376/941664/First-Attempt-of-Boron-Neutron-Capture-Therapy

[43] R. L. Moss, "Progress towards boron neutron capture therapy at the High Flux Reactor Petten." *Basic life sciences*, vol. 54, pp. 169–83, 1990. [Online]. Available: http://www.ncbi.nlm.nih.gov/pubmed/2268238

[44] S. Savolainen, I. Auterinen, M. Kallio, M. Karkkainen, A. Kosunen, C. Aschan, J. Benczik, M. Farkkila, P. Hiismaki, K. Kaita, M. Kulvik, P. Ryynanen, T. Seppala, T. Seren, V. Tanner, M. Toivonen, J. Vahatalo, and H. Yla-Mella, "The Finnish boron neutron capture therapy program - an overview on scientific projects," *International Congress Series*, vol. 1132, no. June, pp. A342–A347, 1997.

[45] J. Burian and J. Rataj, "Neutron Beam Design and Performance for BNCT in Czechoslovakia," in *Neutron Beam Design, Development, and Performance for Neutron Capture Therapy*. Boston, MA: Springer US, 1990, pp. 229–233. [Online]. Available: http://link.springer.com/10.1007/978-1-4684-5802-2{_}17

[46] J. Burian, M. Marek, J. Rataj, S. Flibor, J. Rejchrt, L. Viererbl, F. Sus, H. Honova, L. Petruzelka, K. Prokes, F. Tovarys, V. Dbaly, V. Benes, P. Kozler, J. Honzatko, I. Tomandl, and V. Mares, "Report on the first patient group of the phase I BNCT trial at the LVR-15 reactor," *International Congress Series*, vol. 1259, pp. 27–32, feb 2004. [Online]. Available: http://linkinghub.elsevier.com/retrieve/pii/S0531513103015152

[47] J. Capala, B. H. Stenstam, K. Sköld, P. Munck af Rosenschöld, V. Giusti, C. Persson, E. Wallin, A. Brun, L. Franzen, J. Carlsson, L. Salford, C. Ceberg, B. Persson, L. Pellettieri, and R. Henriksson, "Boron neutron capture therapy for glioblastoma multiforme: clinical studies in Sweden."

Journal of neuro-oncology, vol. 62, no. 1-2, pp. 135–44. [Online]. Available: http://www.ncbi.nlm.nih.gov/pubmed/12749709

[48] A. Zonta, U. Prati, L. Roveda, C. Ferrari, S. Zonta, A. Clerici, C. Zonta, T. Pinelli, F. Fossati, S. Altieri, S. Bortolussi, P. Bruschi, R. Nano, S. Barni, P. Chiari, and G. Mazzini, "Clinical lessons from the first applications of BNCT on unresectable liver metastases." *Journal of Physics: Conference Series*, vol. 41, pp. 484–495, may 2006. [Online]. Available: http://stacks.iop.org/1742-6596/41/i=1/a=054?key=crossref.12b7b65e8d6d5e95ab3ced9d236cf719

[49] S. J. González, M. R. Bonomi, G. A. Santa Cruz, H. R. Blaumann, O. A. Calzetta Larrieu, P. Menéndez, R. Jiménez Rebagliati, J. Longhino, D. B. Feld, M. A. Dagrosa, C. Argerich, S. G. Castiglia, D. A. Batistoni, S. J. Liberman, and B. M. C. Roth, "First BNCT treatment of a skin melanoma in Argentina: dosimetric analysis and clinical outcome." *Applied radiation and isotopes : including data, instrumentation and methods for use in agriculture, industry and medicine*, vol. 61, no. 5, pp. 1101–5, nov 2004. [Online]. Available: http://www.ncbi.nlm.nih.gov/pubmed/15308199

[50] L. W. Wang, S. J. Wang, P. Y. Chu, C. Y. Ho, S. H. Jiang, Y. W. H. Liu, Y. H. Liu, H. M. Liu, J. J. Peir, F. I. Chou, S. H. Yen, Y. L. Lee, C. W. Chang, C. S. Liu, Y. W. Chen, and K. Ono, "BNCT for locally recurrent head and neck cancer: preliminary clinical experience from a phase I/II trial at Tsing Hua Open-Pool Reactor." *Applied radiation and isotopes : including data, instrumentation and methods for use in agriculture, industry and medicine*, vol. 69, no. 12, pp. 1803–6, dec 2011. [Online]. Available: http://www.ncbi.nlm.nih.gov/pubmed/21478023

[51] L. Yiguo, X. Pu, W. Xiao, and K. Fuquan, "Start-up of the first in hospital neutron irradiator (IHNI-1) & presentation of the BNCT development status in China," in *New Challenges in Neutron Capture Therapy 2010: Proceedings*

of the 14th International Congress on Neutron Capture Therapy, 2013, pp. 371–374.

[52] J. C. Yanch, X.-L. Zhou, R. E. Shefer, and R. E. Klinkowstein, "Accelerator-based epithermal neutron beam design for neutron capture therapy," *Medical Physics*, vol. 19, no. 3, pp. 709–721, may 1992. [Online]. Available: http://doi.wiley.com/10.1118/1.596815

[53] D. A. Allen and T. D. Beynon, "A design study for an accelerator-based epithermal neutron beam for BNCT." *Physics in medicine and biology*, vol. 40, no. 5, pp. 807–21, may 1995. [Online]. Available: http://www.ncbi.nlm.nih.gov/pubmed/7652009

[54] N. Gupta, J. Niemkiewicz, T. E. Blue, R. Gahbauer, and T. X. Qu, "Effect of head phantom size on 10 B and 1 H[n ,γ] 2 H dose distributions for a broad field accelerator epithermal neutron source for BNCT," *Medical Physics*, vol. 20, no. 2, pp. 395–404, mar 1993. [Online]. Available: http://doi.wiley.com/10.1118/1.597131

[55] T. X. B. Qu, T. E. Blue, C. K. C. Wang, and R. A. Gahbauer, "A Neutronic Study of an Accelerator-Based Neutron Irradiation Facility for the Treatment of Superficial Melanoma by Boron Neutron Capture Therapy," *Nuclear Technology*, vol. 91, no. 3, pp. 404–412, 1990. [Online]. Available: https://www.tandfonline.com/doi/full/10.13182/NT90-A34461

[56] W. B. Howard, J. C. Yanch, S. M. Grimes, T. N. Massey, S. I. Al-Quraishi, D. K. Jacobs, and C. E. Brient, "Measurement of the 9 Be(p , n) thick target spectrum for use in accelerator-based Boron Neutron Capture Therapy," *Medical Physics*, vol. 23, no. 7, pp. 1233–1235, jul 1996. [Online]. Available: http://doi.wiley.com/10.1118/1.597684

[57] C.-K. C. Wang and B. R. Moore, "Thick beryllium target as an epithermal neutron source for neutron capture therapy," *Medical Physics*,

vol. 21, no. 10, pp. 1633–1638, oct 1994. [Online]. Available: http://doi.wiley.com/10.1118/1.597269

[58] T. Kobayashi, G. Bengua, Y. Nakagawa, K. Tanaka, and M. Hoshi, "A possibility of BNCT irradiation systems using accelerators," 2004. [Online]. Available: https://inis.iaea.org/search/search.aspx?orig{_}q=RN:36039729

[59] S. Yonai, T. Aoki, T. Nakamura, H. Yashima, M. Baba, H. Yokobori, and Y. Tahara, "Feasibility study on epithermal neutron field for cyclotron-based boron neutron capture therapy," *Medical Physics*, vol. 30, no. 8, pp. 2021–2030, jul 2003. [Online]. Available: http://doi.wiley.com/10.1118/1.1587431

[60] H. Tanaka, Y. Sakurai, M. Suzuki, S. Masunaga, Y. Kinashi, G. Kashino, Y. Liu, T. Mitsumoto, S. Yajima, H. Tsutsui, A. Maruhashi, and K. Ono, "Characteristics comparison between a cyclotron-based neutron source and KUR-HWNIF for boron neutron capture therapy," *Nuclear Instruments and Methods in Physics Research, Section B: Beam Interactions with Materials and Atoms*, vol. 267, no. 11, pp. 1970–1977, 2009. [Online]. Available: http://dx.doi.org/10.1016/j.nimb.2009.03.095

[61] S. Bentzen and M. Joiner, "The linear-quadratic approach in clinical practice," in *Basic Clinical Radiobiology*, 4th ed., M. Joiner and A. van der Kogel, Eds. London: Hodder Arnold, 2009, ch. 9, pp. 120–134.

[62] J. Beringer, J. F. Arguin, R. M. Barnett, K. Copic, O. Dahl, D. E. Groom, C. J. Lin, J. Lys, H. Murayama, C. G. Wohl, W. M. Yao, P. A. Zyla, C. Amsler, M. Antonelli, D. M. Asner, H. Baer, H. R. Band, T. Basaglia, C. W. Bauer, J. J. Beatty, V. I. Belousov, E. Bergren, G. Bernardi, W. Bertl, S. Bethke, H. Bichsel, O. Biebel, E. Blucher, S. Blusk, G. Brooijmans, O. Buchmueller, R. N. Cahn, M. Carena, A. Ceccucci, D. Chakraborty, M. C. Chen, R. S. Chivukula, G. Cowan, G. D'Ambrosio, T. Damour, D. de Florian, A. de Gouvêa, T. DeGrand, P. de Jong, G. Dissertori,

B. Dobrescu, M. Doser, M. Drees, D. A. Edwards, S. Eidelman, J. Erler, V. V. Ezhela, W. Fetscher, B. D. Fields, B. Foster, T. K. Gaisser, L. Garren, H. J. Gerber, G. Gerbier, T. Gherghetta, S. Golwala, M. Goodman, C. Grab, A. V. Gritsan, J. F. Grivaz, M. Grünewald, A. Gurtu, T. Gutsche, H. E. Haber, K. Hagiwara, C. Hagmann, C. Hanhart, S. Hashimoto, K. G. Hayes, M. Heffner, B. Heltsley, J. J. Hernández-Rey, K. Hikasa, A. Höcker, J. Holder, A. Holtkamp, J. Huston, J. D. Jackson, K. F. Johnson, T. Junk, D. Karlen, D. Kirkby, S. R. Klein, E. Klempt, R. V. Kowalewski, F. Krauss, M. Kreps, B. Krusche, Y. V. Kuyanov, Y. Kwon, O. Lahav, J. Laiho, P. Langacker, A. Liddle, Z. Ligeti, T. M. Liss, L. Littenberg, K. S. Lugovsky, S. B. Lugovsky, T. Mannel, A. V. Manohar, W. J. Marciano, A. D. Martin, A. Masoni, J. Matthews, D. Milstead, R. Miquel, K. Mönig, F. Moortgat, K. Nakamura, M. Narain, P. Nason, S. Navas, M. Neubert, P. Nevski, Y. Nir, K. A. Olive, L. Pape, J. Parsons, C. Patrignani, J. A. Peacock, S. T. Petcov, A. Piepke, A. Pomarol, G. Punzi, A. Quadt, S. Raby, G. Raffelt, B. N. Ratcliff, P. Richardson, S. Roesler, S. Rolli, A. Romaniouk, L. J. Rosenberg, J. L. Rosner, C. T. Sachrajda, Y. Sakai, G. P. Salam, S. Sarkar, F. Sauli, O. Schneider, K. Scholberg, D. Scott, W. G. Seligman, M. H. Shaevitz, S. R. Sharpe, M. Silari, T. Sjöstrand, P. Skands, J. G. Smith, G. F. Smoot, S. Spanier, H. Spieler, A. Stahl, T. Stanev, S. L. Stone, T. Sumiyoshi, M. J. Syphers, F. Takahashi, M. Tanabashi, J. Terning, M. Titov, N. P. Tkachenko, N. A. Törnqvist, D. Tovey, G. Valencia, K. van Bibber, G. Venanzoni, M. G. Vincter, P. Vogel, A. Vogt, W. Walkowiak, C. W. Walter, D. R. Ward, T. Watari, G. Weiglein, E. J. Weinberg, L. R. Wiencke, L. Wolfenstein, J. Womersley, C. L. Woody, R. L. Workman, A. Yamamoto, G. P. Zeller, O. V. Zenin, J. Zhang, R. Y. Zhu, G. Harper, V. S. Lugovsky, and P. Schaffner, "Review of Particle Physics," *Physical Review D*, vol. 86, no. 1, jul 2012. [Online]. Available: https://link.aps.org/doi/10.1103/PhysRevD.86.010001

[63] A. M. Kellerer and H. H. Rossi, *Current topics in radiation research quarterly*,

8th ed., M. Ebert and A. Howard, Eds. Amsterdam: North Holland, 1974.

[64] R. B. Hawkins, "A statistical theory of cell killing by radiation of varying linear energy transfer." *Radiation research*, vol. 140, no. 3, pp. 366–74, dec 1994. [Online]. Available: http://www.ncbi.nlm.nih.gov/pubmed/7972689

[65] ——, "A microdosimetric-kinetic model for the effect of non-Poisson distribution of lethal lesions on the variation of RBE with LET." *Radiation research*, vol. 160, no. 1, pp. 61–9, 2003. [Online]. Available: http://www.ncbi.nlm.nih.gov/pubmed/12816524

[66] Y. Kase, T. Kanai, Y. Matsumoto, Y. Furusawa, H. Okamoto, T. Asaba, M. Sakama, and H. Shinoda, "Microdosimetric measurements and estimation of human cell survival for heavy-ion beams." *Radiation research*, vol. 166, no. 4, pp. 629–38, oct 2006. [Online]. Available: http://www.ncbi.nlm.nih.gov/pubmed/17007551

[67] S. Mori, K. Shibayama, K. Tanimoto, M. Kumagai, Y. Matsuzaki, T. Furukawa, T. Inaniwa, T. Shirai, K. Noda, H. Tsuji, and T. Kamada, "First clinical experience in carbon ion scanning beam therapy: retrospective analysis of patient positional accuracy." *Journal of radiation research*, vol. 53, no. 5, pp. 760–8, sep 2012. [Online]. Available: http://www.ncbi.nlm.nih.gov/pubmed/22927632http://www.pubmedcentral.nih.gov/articlerender.fcgi?artid=PMC3430428

[68] M. Scholz and G. Kraft, "Track structure and the calculation of biological effects of heavy charged particles," *Advances in Space Research*, vol. 18, no. 1-2, pp. 5–14, jan 1996. [Online]. Available: http://linkinghub.elsevier.com/retrieve/pii/027311779500784C

[69] W. Hanson, L. Anderson, and C. C. Ling, "Physical Aspects of Quality Assurance in Radiation Therapy," no. 13, 1994. [Online]. Available: http://mail.aapm.org/pubs/reports/RPT{_}13.pdf

[70] T. E. Blue, N. Gupta, and J. E. Woollard, "A calculation of the energy dependence of the RBE of neutrons," *Physics in Medicine and Biology*, vol. 38, no. 12, pp. 1693–1712, dec 1993. [Online]. Available: http://stacks.iop.org/0031-9155/38/i=12/a=002?key=crossref.a67e6ab21486e7bfb5b77bb1c539d2b8

[71] P. D. Bradley, "The Development of a Novel Silicon Microdosimeter for High LET Radiation Therapy," Ph.D. dissertation, University of Wollongong, 2000.

[72] F. Dessauer, "Uber einige Wirkungen von Strahlen," *I. Z. Phys.*, vol. 12, pp. 38–44, 1922.

[73] J. A. Crowther, "Some considerations relative to the action of X-rays on tissue cells," in *Proceedings of the Royal Society of London. Series B, Containing papers of a biological character*, 1924, pp. 207–211.

[74] P. Jordan, "Uber die elementarprozesse der biologischen strahlenwirkung," *Radiologica*, vol. 2, no. 16, p. 166, 1938.

[75] L. Gray, "The distribution of the ions resulting from the irradiation of living cells," *J. Radiol. Suppl.*, vol. 1, p. 7, 1947.

[76] S. C. Lind, "Actions of Radiations on Living Cells. By D. E. Lea." *The Journal of Physical and Colloid Chemistry*, vol. 51, no. 6, pp. 1451–1451, jun 1947. [Online]. Available: http://pubs.acs.org/doi/abs/10.1021/j150456a021

[77] R. E. ZIRKLE, D. F. MARCHBANK, and K. D. KUCK, "Exponential and sigmoid survival curves resulting from alpha and x irradiation of Aspergillus spores." *Journal of cellular physiology. Supplement*, vol. 39, no. Suppl. 1, pp. 78–85, mar 1952. [Online]. Available: http://www.ncbi.nlm.nih.gov/pubmed/14927690

[78] ICRU, "Report 16," *Journal of the International Commission on Radiation Units and Measurements*, vol. os9, no. 1, pp. NP–NP, jun 1970. [Online]. Available: https://academic.oup.com/jicru/article/2924191/Report

[79] A. M. Kellerer and D. Chmelevsky, "Criteria for the applicability of LET," *Radiation research*, vol. 63, no. 2, pp. 226–234, 1975.

[80] J. Booz, L. Braby, J. Coyne, P. Kliauga, L. Lindborg, H.-G. Menzel, and N. Parmentier, "Report 36," *Journal of the International Commission on Radiation Units and Measurements*, vol. os19, no. 1, pp. NP–NP, dec 1983. [Online]. Available: https://doi.org/10.1093/jicru/os19.1.Report36https://academic.oup.com/jicru/article/2923741/Report

[81] H. H. Rossi and W. Rosenzweig, "A Device for the Measurement of Dose as a Function of Specific Ionization," *Radiology*, vol. 64, no. 3, pp. 404–411, mar 1955. [Online]. Available: http://dx.doi.org/10.1148/64.3.404

[82] D. Srdoč and D. Srdoc, "Experimental Technique of Measurement of Microscopic Energy Distribution in Irradiated Matter Using Rossi Counters," *Radiation Research*, vol. 43, no. 2, p. 302, aug 1970. [Online]. Available: https://www.jstor.org/stable/3573036?origin=crossref

[83] P. Kliauga, "Measurement of Single Event Energy Deposition Spectra at 5 nm to 250 nm Simulated Site Sizes," *Radiation Protection Dosimetry*, vol. 31, no. 1-4, pp. 119–123, jun 1990. [Online]. Available: https://academic.oup.com/rpd/article-lookup/doi/10.1093/oxfordjournals.rpd.a080650

[84] V. Cesari, N. Iborra, L. De Nardo, P. Querini, V. Conte, P. Colautti, G. Tornielli, and P. Chauvel, *Microdosimetric measurements of the nice therapeutic proton beam*, jan 2001, vol. 17.

[85] J. Burmeister, C. Kota, R. L. Maughan, and A. J. Waker, "Characterization of miniature tissue-equivalent proportional counters for neutron radiotherapy applications," *Physics in Medicine and Biology*, vol. 47, no. 10, pp. 1633–1645, 2002.

[86] D. Moro, P. Colautti, M. Lollo, J. Esposito, V. Conte, L. De Nardo, A. Ferretti, and C. Ceballos, "BNCT dosimetry performed with a mini twin tissue-

equivalent proportional counters (TEPC)," *Applied Radiation and Isotopes*, vol. 67, no. 7-8 SUPPL., pp. 171–174, 2009.

[87] P. J. Mcnulty, J. W. Beauavais, and D. R. Roth, "Microdosimetry radiation analysis method and device," 1993.

[88] D. R. Roth, P. J. McNulty, W. J. Beauvais, R. A. Reed, and E. G. Stassinopoulos, "Solid State Microdosimeter for Radiation Monitoring in Spacecraft and Avionics," *IEEE Transactions on Nuclear Science*, vol. 41, no. 6, pp. 2118–2124, 1994.

[89] A. Rosenfeld, G. Kaplan, M. Carolan, B. Allen, R. Maughan, M. Yudelev, C. Kota, and J. Coderre, "Simultaneous macro and micro dosimetry with MOSFETs," *IEEE Transactions on Nuclear Science*, vol. 43, no. 6, pp. 2693–2700, 1996. [Online]. Available: http://ieeexplore.ieee.org/lpdocs/epic03/wrapper.htm?arnumber=556855

[90] A. Rosenfeld and P. Bradley, "Semiconductor Microdosimetry in Mixed Radiation and Photon Fields: Present and Future," *Radiation Protection Dosimetry*, vol. 85, no. 1, pp. 385–388, sep 1999. [Online]. Available: https://academic.oup.com/rpd/article-lookup/doi/10.1093/oxfordjournals.rpd.a032877

[91] A. B. Rosenfeld, P. Bradley, I. Cornelius, G. I. Kaplan, B. J. Allen, A. B. Anatoly Rosenfeld, J. B. Flanz, M. Goitein, A. Van Meerbeeck, J. Schubert, J. Bailey, Y. Takada, A. Maruhashi, Y. Hayakawa, A. Rosenfeld, P. Bradley, G. Kaplan, B. Allen, and J. Flanz, "A new silicon detector for microdosimetry applications in proton therapy I et al, A new silicon detector for microdosimetry applications in proton therapy A New Silicon Detector for Microdosimetry Applications in Proton Therapy," *IEEE Transactions on Nuclear Science*, vol. 47, no. 4, pp. 1386–1394, 2000. [Online]. Available: http://ro.uow.edu.au/engpapers/16

[92] A. Wroe, A. Rosenfeld, M. Reinhard, V. Pisacane, J. Ziegler, M. Nelson, F. Cucinotta, M. Zaider, and J. Dicello, "Solid state microdosimetry with heavy ions for space applications," *IEEE Transactions on Nuclear Science*, vol. 54, no. 6, pp. 2264–2271, 2007.

[93] I. Cornelius, R. Siegele, A. B. Rosenfeld, and D. D. Cohen, "Ion beam induced charge characterisation of a silicon microdosimeter using a heavy ion microprobe," *Nuclear Instruments and Methods in Physics Research, Section B: Beam Interactions with Materials and Atoms*, vol. 190, no. 1-4, pp. 335–338, 2002.

[94] S. Guatelli, M. I. Reinhard, B. Mascialino, D. A. Prokopovich, A. S. Dzurak, M. Zaider, and A. B. Rosenfeld, "Tissue equivalence correction in silicon microdosimetry for protons characteristic of the LEO space environment," *IEEE Transactions on Nuclear Science*, vol. 55, no. 6, pp. 3407–3413, 2008.

[95] D. A. Prokopovich, M. I. Reinhard, G. C. Taylor, A. Hands, and A. B. Rosenfeld, "Comparison of SOI microdosimeter and tissue equivalent proportional counter measurements at the CERF facility," *IEEE Transactions on Nuclear Science*, vol. 59, no. 5 PART 3, pp. 2501–2505, 2012.

[96] A. Wroe, A. Rosenfeld, and R. Schulte, "Out-of-field dose equivalents delivered by proton therapy of prostate cancer," *Medical Physics*, vol. 34, no. 9, pp. 3449–3456, 2007.

[97] L. T. Tran, L. Chartier, D. A. Prokopovich, M. I. Reinhard, M. Petasecca, S. Guatelli, M. L. F. Lerch, V. L. Perevertaylo, M. Zaider, N. Matsufuji, M. Jackson, M. Nancarrow, and A. B. Rosenfeld, "3D-mesa 'bridge' silicon microdosimeter: Charge collection study and application to RBE studies in 12C radiation therapy," *IEEE Transactions on Nuclear Science*, vol. 62, no. 2, pp. 504–511, 2015.

[98] L. T. Tran, L. Chartier, D. Bolst, J. Davis, D. A. Prokopovich, A. Pogossov, S. Guatelli, M. I. Reinhard, M. Petasecca, M. L. Lerch, N. Matsufuji, M. Povoli, A. Summanwar, A. Kok, M. Jackson, and A. B. Rosenfeld, "In-field and out-of-file application in12C ion therapy using fully 3D silicon microdosimeters," *Radiation Measurements*, vol. 115, no. February, pp. 55–59, 2018.

[99] N. S. Lai, S. Member, W. H. Lim, A. L. Ziebell, M. I. Reinhard, A. B. Rosenfeld, S. Member, and A. S. Dzurak, "Development and Fabrication of Cylindrical Silicon-on-Insulator Microdosimeter Arrays," *IEEE Transactions on Nuclear Science*, vol. 56, no. 3, pp. 1637–1641, 2009.

[100] S. Parker, C. Kenney, and J. Segal, "3D â A proposed new architecture for solid-state radiation detectors," *Nuclear Instruments and Methods in Physics Research Section A: Accelerators, Spectrometers, Detectors and Associated Equipment*, vol. 395, no. 3, pp. 328–343, aug 1997. [Online]. Available: http://linkinghub.elsevier.com/retrieve/pii/S0168900297006943

[101] A. Kok, G. Anelli, C. DaVia, J. Hasi, P. Jarron, C. Kenney, J. Morse, S. Parker, J. Segal, S. Watts, and E. Westbrook, "3D detectorsâstate of the art," *Nuclear Instruments and Methods in Physics Research Section A: Accelerators, Spectrometers, Detectors and Associated Equipment*, vol. 560, no. 1, pp. 127–130, may 2006. [Online]. Available: http://linkinghub.elsevier.com/retrieve/pii/S0168900205023508

[102] NorFab, "SINTEF MiNaLab," 2018. [Online]. Available: https://www.norfab.no/lab-facilities/sintef-minalab/

[103] E. Monakhov, "Silicon based 3D mini- and microdosimeter," 2013. [Online]. Available: https://www.mn.uio.no/smn/english/research/projects/physics/si-3dmimic/

[104] T.-E. Hansen, A. Kok, T. A. Hansen, N. Lietaer, M. Mielnik, P. Storås, C. D. Via, J. Hasi, C. Kenney, and S. Parker, "First fabrication of full 3D-detectors

at SINTEF," *Journal of Instrumentation*, vol. 4, no. 03, pp. P03 010–P03 010, mar 2009. [Online]. Available: http://stacks.iop.org/1748-0221/4/i=03/a=P03010?key=crossref.80fb9281369c23f02e5e0b288b5c6177

[105] L. T. Tran, L. Chartier, D. A. Prokopovich, D. Bolst, M. Povoli, A. Summanwar, A. Kok, A. Pogossov, M. Petasecca, S. Guatelli, M. I. Reinhard, M. Lerch, M. Nancarrow, N. Matsufuji, M. Jackson, and A. B. Rosenfeld, "Thin Silicon Microdosimeter Utilizing 3-D MEMS Fabrication Technology: Charge Collection Study and Its Application in Mixed Radiation Fields," *IEEE Transactions on Nuclear Science*, vol. 65, no. 1, pp. 467–472, 2018.

[106] H. H. Rossi, "Specification of Radiation Quality," *Radiation Research*, vol. 10, no. 5, pp. 522–531, may 1959. [Online]. Available: http://www.rrjournal.org/doi/abs/10.2307/3570787

[107] L. W. Brackenbush, G. W. Endres, and D. E. Hadlock, "A New Type of REM Measuring Instrument," *IEEE Transactions on Nuclear Science*, vol. 33, no. 1, pp. 609–612, 1986.

[108] Y. Onizuka, S. Endo, M. Ishikawa, M. Hoshi, M. Takada, T. Kobayashi, Y. Sakurai, H. Utsumi, S. Uehara, N. Hayabuchi, N. Maeda, T. Takatuji, K. Fujika, Q. E. Applications, I. Radiation, and R. General, "MICRODOSIMETRY OF EPITHERMAL NEUTRON FIELD AT THE KYOTO UNIVERSITY REACTOR," *Radiation protection dosimetry*, vol. 99, pp. 383–385, 2002.

[109] S. Endo, Y. Onizuka, M. Ishikawa, M. Takada, Y. Sakurai, T. Kobayashi, K. Tanaka, M. Hoshi, and K. Shizuma, "Microdosimetry of neutron field for boron neutron capture therapy at Kyoto University reactor," *Radiation Protection Dosimetry*, vol. 110, no. 1-4, pp. 641–644, 2004.

[110] ICRU, "The quality factor in radiation protection. ICRU Report no. 40," *Journal of the International Commission on Radiation Units and*

Measurements, vol. os21, no. 1, pp. NP–NP, apr 1986. [Online]. Available: https://academic.oup.com/jicru/article/2923767/Report

[111] A. Tilikidis, B. Lind, P. Näfstadius, and A. Brahme, "An estimation of the relative biological effectiveness of 50 MV bremsstrahlung beams by microdosimetric techniques," *Physics in Medicine and Biology*, vol. 41, no. 1, pp. 55–69, 1996.

[112] J. Dennis, *Neutron Dosimetry for Biology and Medicine: ICRU Report 26*, 1978, vol. 33, no. 1. [Online]. Available: http://www.tandfonline.com/doi/full/10.1080/09553007714551571

[113] T. Sato, Y. Iwamoto, S. Hashimoto, T. Ogawa, T. Furuta, S.-i. Abe, T. Kai, P.-E. Tsai, N. Matsuda, H. Iwase, N. Shigyo, L. Sihver, and K. Niita, "Features of Particle and Heavy Ion Transport code System (PHITS) version 3.02," *Journal of Nuclear Science and Technology*, vol. 55, no. 6, pp. 684–690, jun 2018. [Online]. Available: https://www.tandfonline.com/doi/full/10.1080/00223131.2017.1419890

[114] Y. Iwamoto, T. Sato, S. Hashimoto, T. Ogawa, T. Furuta, S.-i. Abe, T. Kai, N. Matsuda, R. Hosoyamada, and K. Niita, "Benchmark study of the recent version of the PHITS code," *Journal of Nuclear Science and Technology*, vol. 54, no. 5, pp. 617–635, may 2017. [Online]. Available: https://www.tandfonline.com/doi/full/10.1080/00223131.2017.1297742

[115] Far West Technology Inc, "Model LET-1/2 operation manual," 2001. [Online]. Available: http://www.fwt.com/detector/support/LET12{_}manual.PDF

[116] F. Y. Hsu, H. W. Hsiao, C. J. Tung, H. M. Liu, and F. I. Chou, "Microdosimetry study of THOR BNCT beam using tissue equivalent proportional counter," *Applied Radiation and Isotopes*, vol. 67, no. 7-8 SUPPL., pp. 175–178, 2009.

[117] P. Colautti, D. Moro, S. Chiriotti, V. Conte, L. Evangelista, S. Altieri, S. Bortolussi, N. Protti, and I. Postuma, "Microdosimetric measurements

in the thermal neutron irradiation facility of LENA reactor," *Applied Radiation and Isotopes*, vol. 88, pp. 147–152, 2014. [Online]. Available: http://dx.doi.org/10.1016/j.apradiso.2014.01.005

[118] S. Endo, M. Hoshi, J. Takada, H. Tauchi, S. Matsuura, S. Takeoka, K. Kitagawa, S. Suga, and K. Komatsu, "Neutron generator (HIRRAC) and dosimetry study." *Journal of radiation research*, vol. 40 Suppl, pp. 14–20, 1999.

[119] S. Endo, K. Tanaka, K. Fujikawa, T. Horiguchi, T. Itoh, Y. Onizuka, M. Hoshi, A. Murataka, Y. Kojima, and K. Shizuma, "Microdosimetry on a mini-reactor UTR-KINKI for educational uses and biological researches," *Journal of Radiation Research*, vol. 50, no. 1, pp. 83–87, 2009.

[120] R. D. Rogus, O. K. Harling, and J. C. Yanch, *Mixed Field Dosimetry of Neutron Beams for Boron Neutron Capture Therapy at the Massachusetts Institute of Technology.* Boston, MA: Springer US, 1996, pp. 457–466. [Online]. Available: https://doi.org/10.1007/978-1-4757-9567-7{_}65

[121] J. A. Coderre, E. H. Elowitz, M. Chadha, R. Bergland, J. Capala, D. D. Joel, H. B. Liu, D. N. Slatkin, and A. D. Chanana, "Boron neutron capture therapy for glioblastoma multiforme using p-boronophenylalanine and epithermal neutrons: trial design and early clinical results." *Journal of neuro-oncology*, vol. 33, no. 1-2, pp. 141–52, 1997. [Online]. Available: http://www.ncbi.nlm.nih.gov/pubmed/9151231

[122] J. Gueulette, M. Octave-Prignot, B.-M. De Coster, A. Wambersie, and V. Grégoire, "Intestinal crypt regeneration in mice : a biological system for quality assurance in non-conventional radiation therapy," *Radiotherapy and Oncology*, vol. 73, no. 1, pp. S148–S154, dec 2004. [Online]. Available: https://linkinghub.elsevier.com/retrieve/pii/S0167814004800380

[123] S. J. González and G. A. Santa Cruz, "The Photon-Isoeffective Dose in Boron Neutron Capture Therapy," *Radiation Research*, vol. 178, no. 6, pp. 609–621, dec 2012. [Online]. Available: http://www.bioone.org/doi/10.1667/RR2944.1

[124] T. Sato, S.-i. Masunaga, H. Kumada, and N. Hamada, "DEPTH DISTRIBUTIONS OF RBE-WEIGHTED DOSE and PHOTON-ISOEFFECTIVE DOSE FOR BORON NEUTRON CAPTURE THERAPY," *Radiation Protection Dosimetry*, vol. 183, no. 1, pp. 247–250, 2018.

[125] A. M. Kellerer, "Event Simultaneity in Cavities: Theory of the Distortions of Energy Deposition in Proportional Counters," *Radiation Research*, vol. 48, no. 2, p. 216, nov 1971. [Online]. Available: https://www.jstor.org/stable/3573307?origin=crossref

[126] ——, "Considerations on the random traversal of convex bodies and solutions for general cylinders." *Radiation research*, vol. 47, no. 2, pp. 359–76, 1971. [Online]. Available: http://www.ncbi.nlm.nih.gov/pubmed/5561927

[127] P. D. Bradley, A. B. Rosenfeld, B. Allen, J. Coderre, and J. Capala, "Performance of silicon microdosimetry detectors in boron neutron capture therapy," *Radiation research*, vol. 151, pp. 235–243, 1999.

[128] L. Kankaanranta, T. Seppälä, H. Koivunoro, K. Saarilahti, T. Atula, J. Collan, E. Salli, M. Kortesniemi, J. Uusi-Simola, P. Välimäki, A. Mäkitie, M. Seppänen, H. Minn, H. Revitzer, M. Kouri, P. Kotiluoto, T. Seren, I. Auterinen, S. Savolainen, and H. Joensuu, "Boron Neutron Capture Therapy in the Treatment of Locally Recurred Head-and-Neck Cancer: Final Analysis of a Phase I/II Trial," *International Journal of Radiation Oncology*Biology*Physics*, vol. 82, no. 1, pp. e67–e75, jan 2012. [Online]. Available: http://linkinghub.elsevier.com/retrieve/pii/S0360301610034632

[129] I. Takaki, I. Yoshie, K. Naoto, Y. Naofumi, T. Hiroki, M. Shin-ichiro, S. Yoshinori, K. Itsuro, I. Soichi, S. Minoru, and Y. Yoshiaki, "Boron Carbide Particle

as a Boron Compound for Boron Neutron Capture Therapy," *J Nucl Med Radiat Ther*, vol. 5, no. -, 2014.

[130] G. Nowak, M. Störmer, H.-W. Becker, C. Horstmann, R. Kampmann, D. Höche, M. Haese-Seiller, J.-F. Moulin, M. Pomm, C. Randau, U. Lorenz, R. Hall-Wilton, M. Müller, and A. Schreyer, "Boron carbide coatings for neutron detection probed by x-rays, ions, and neutrons to determine thin film quality," *Journal of Applied Physics*, vol. 117, no. 3, p. 034901, jan 2015. [Online]. Available: http://aip.scitation.org/doi/10.1063/1.4905716

[131] H. H. Rossi and M. Zaider, *Microdosimetry and Its Applications*, 1st ed. Berlin, Heidelberg: Springer Berlin Heidelberg, 1996. [Online]. Available: http://link.springer.com/10.1007/978-3-642-85184-1

[132] A. Wambersie, P. Pihet, and H. Menzel (INVITED), "The Role of Microdosimetry in Radiotherapy," *Radiation Protection Dosimetry*, vol. 31, no. 1-4, pp. 421–432, jun 1990. [Online]. Available: https://academic.oup.com/rpd/article-lookup/doi/10.1093/oxfordjournals.rpd.a080707

[133] J. F. Ziegler, M. Ziegler, and J. Biersack, "SRIM â The stopping and range of ions in matter (2010)," *Nuclear Instruments and Methods in Physics Research Section B: Beam Interactions with Materials and Atoms*, vol. 268, no. 11-12, pp. 1818–1823, jun 2010. [Online]. Available: http://linkinghub.elsevier.com/retrieve/pii/S0168583X10001862

[134] A. L. Ziebell, W. H. Lim, M. I. Reinhard, I. Cornelius, D. A. Prokopovich, R. Siegele, A. S. Dzurak, and A. B. Rosenfeld, "A cylindrical silicon-on-insulator microdosimeter: Charge collection characteristics," *IEEE Transactions on Nuclear Science*, vol. 55, no. 6, pp. 3414–3420, 2008.

[135] T. Mukawa, T. Matsumoto, and K. Niita, "Study on Microdosimetry for Boron Neutron Capture Therapy," *Progress in NUCLEAR SCIENCE and TECHNOLOGY*, vol. 2, pp. 242–246, 2011.

[136] A. Karaoglu, P. Arce, D. Obradors, J. I. Lagares, and P. Unak, "Calculation by GAMOS/Geant4 simulation of cellular energy distributions from alpha and lithium-7 particles created by BNCT," *Applied Radiation and Isotopes*, vol. 132, pp. 206–211, feb 2018. [Online]. Available: http://linkinghub.elsevier.com/retrieve/pii/S0969804317309594

[137] C. Werner, "MCNP Users Manual - Code Version 6.2," Los Alamos National Laboratory, Tech. Rep., 2017.

Appendix

Calculation of Watt fission spectra

The following expression was used to calculate the ^{252}Cf neutron spectrum

$$f(E) = C \exp(-\frac{E}{a}) \sinh(\sqrt{bE}) \tag{6.1}$$

where a and b are constants and C is a normalisation constant used in MCNP [137].

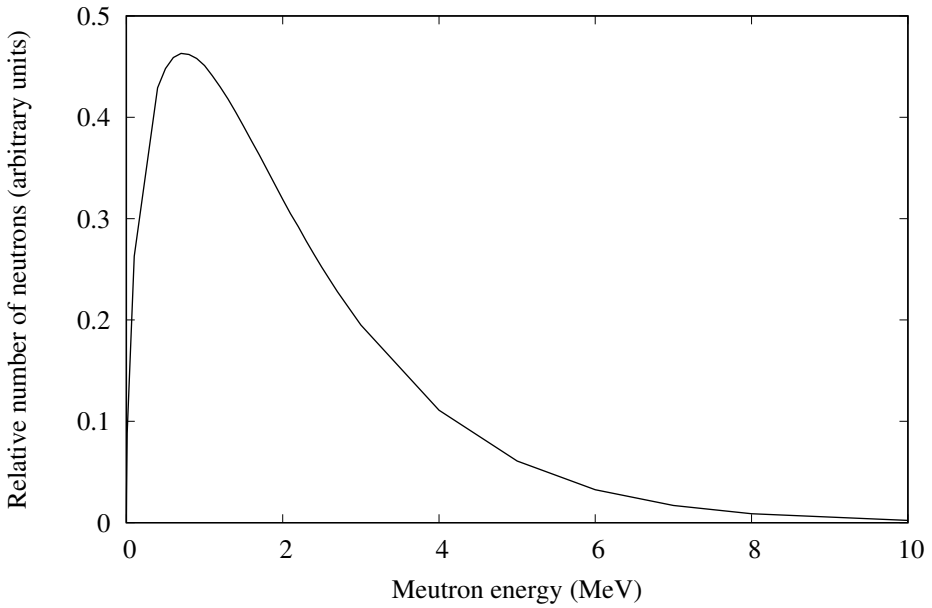

Figure 6.1: ^{252}Cf spectrum calculated from the Watt fission spectra

Gas pressure calculation

TEPC

According to ICRU report 36 [80], if the atomic composition of tissue and gas are identical, and if the mass stopping powers are independent of the density, it follows that:

$$\rho_g = \frac{\rho_t}{k_{gt}} \tag{6.2}$$

where subscripts $\rho_g$and ρ_t correspond to density of the gas and tissue, respectively and $k_{gt}$is the ratio of the diameter of the two medium. Assuming a unit density tissue the above expression becomes:

$$\rho_g = \frac{1}{k_{gt}} \tag{6.3}$$

Therefore, the the mean energy loss of charged particles is equal in both spheres if the ratio of the density of the gas to the density of the tissue is chosen to be equal to the ratio k_{gt}.

Table 6.1: Parameters used to calculate the density inside the cavity.

Tissue diameter (cm)	1×10^{-4}
TEPC cavity diameter (cm)	1.27
k_{gt}(unitless)	1.24×10^{4}
ρ_g(g/cm^3)	7.87×10^{-5}

Table 6.2: Atomic composition inside the TEPC cavity.

	Hydrogen	Carbon	Nitrogen	Oxygen
Atomic mass (u)	1.00794	12.011	14.00674	15.9994
CH4 (64.4%)	4×0.644	1×0.644	0	0
CO2 (32.5%)	0	1×0.325	0	2×0.325
N2 (3.1%)	0	0	2×0.031	0
Corrected atomic mass (u)	2.596	11.639	0.868	10.399

Total atomic mass of gas = 2.596 u + 11.639 u + 0.868 u + 10.399 u

$$
\begin{aligned}
&= && 2.596 \text{ u} \\
&= && 25.502 \text{ u} \\
&= && 25.502 \text{ u}/N_A \\
&= && 4.235 \times 10^{-23} \text{ g}
\end{aligned}
$$

$$
\begin{aligned}
\text{Number density of gas} &= \frac{7.87 \times 10^{-5} \text{ g} \cdot \text{cm}^{-3}}{4.235 \times 10^{-23} \text{ g}} \\
&= 1.858 \times 10^{18} \text{ cm}^{-3} \\
&= 1.858 \times 10^{24} \text{ m}^{-3}
\end{aligned}
$$

For an inhomogeneous system, the pressure inside a cavity can be calculated using the following equation:

$$P = k_B n T \tag{6.4}$$

where $k_B$is the Boltzmann constant, n is the number density and T is the temperature.

$$
\begin{aligned}
\text{Pressure} &= 1.38 \times 10^{-23} \text{ J/K} \times 1.858 \times 10^{24} \text{ m}^{-3} \times 293.15 \text{ K} \\
&= 7516.5 \text{ J/m}^{-3} \\
&= 75.17 \text{ hPa}
\end{aligned}
$$

Graphite walled proportional counter

Table 6.3: Atomic composition inside the graphite walled proportional counter cavity.

	Hydrogen	Carbon	Nitrogen	Oxygen
Atomic mass (u)	1.00794	12.011	14.00674	15.9994
CO_2 (100%)	0	1×12.011	0	2×15.9994
Corrected atomic mass (u)	0	12.011	0	31.9988

$$
\begin{aligned}
\text{Total atomic mass of gas} &= 12.011\ \text{u} + 31.9988\ \text{u} \\
&= 44.0098\ \text{u} \\
&= 44.0098\ \text{u}/N_A \\
&= 7.308 \times 10^{-23}\ \text{g}
\end{aligned}
$$

$$
\begin{aligned}
\text{Number density of gas} &= \frac{7.87 \times 10^{-5}\ \text{g}\cdot\text{cm}^{-3}}{7.308 \times 10^{-23}\ \text{g}} \\
&= 1.077 \times 10^{18}\ \text{cm}^{-3} \\
&= 1.077 \times 10^{24}\ \text{m}^{-3}
\end{aligned}
$$

$$
\begin{aligned}
\text{Pressure} &= 1.38 \times 10^{-23}\ \text{J/K} \times 1.077 \times 10^{24}\ \text{m}^{-3} \times 293.15\ \text{K} \\
&= 4356.97\ \text{J/m}^{-3} \\
&= 43.57\ \text{hPa}
\end{aligned}
$$